EVALUATION AND PERFORMANCE PREDICTION OF COOLING TOWER RAIN ZONES

by

Darren John Pierce

Thesis presented in partial fulfilment of the requirements for the degree M.Sc. Engineering at the University of Stellenbosch.

Supervisor: H.C.R. Reuter

Co-supervisor: Prof. D.G. Kröger

Department of Mechanical Engineering
University of Stellenbosch
Stellenbosch, South Africa

March 2007

DECLARATION

I, the undersigned, hereby declare that the work contained in this thesis is my own original work and that I have not previously in its entirety or in part submitted it at any university for a degree.

Signature:……

Date:……

Abstract

Cooling tower rain zone performance characteristics such as the loss coefficient and the Merkel number are evaluated and simulated. To this end the influence of drop diameter and drop deformation on the velocity, path length and cooling of single water drops are investigated. Experimental drop size and pressure drop data over a counterflow rain zone are presented and the effect of drop deformation on the pressure drop is investigated using the experimental data and CFD. Using the experimental drop size data and CFD, the performance uncertainty produced by using the Rosin-Rammler drop distribution function as opposed to the discrete drop distribution data is investigated. CFD models are developed to investigate the feasibility of modelling rain zones by assuming a constant drop diameter and to establish which diameter definition is the most representative of a particular polydisperse drop distribution. These models were used to validate the correlations for the rain zone performance characteristics proposed in literature.

Opsomming

Die Merkel getal en verlieskoeffisient van ‘n koeltoring se reënsone is gemodelleer. Daar is gekyk na die invloed van druppeldiameter en druppelvervorming op die snelheid, padlengte en uiteindelik die afkoeling van ‘n enkele druppel. Druppelgrootte en drukval data van ‘n dwarsvloei reënsone is eksperimenteel bepaal. Die effek van druppelvervorming op die drukval oor ‘n dwarsvloei reënsone is bepaal deur gebruik te maak van eksperimentele data en CFD. Die verrigtingsonsekerheid wat ontstaan weens die gebruik van ‘n Rosin-Rammler druppelverdeling, in plaas van ‘n diskrete druppelverdeling, is ondersoek deur gebruik te maak van eksperimenteel gemete druppelverdelings en CFD. CFD-modelle is opgestel om die modellering van ‘n reënsone met behulp van ‘n enkele verteenwoordigende druppeldiameter te ondersoek. Daar is ook bepaal hoe so ‘n druppeldiameter gedefinieer moet word, ten einde verteenwoordigend te wees vir spesifieke toestande waar druppels poli-verdeeld is. Laastens is die CFD-modelle gebruik om ‘n korrelasies wat in die literatuur voorkom vir verrigtinskarateristieke te bevestig.

Dedicated to God and my loved ones.

Acknowledgements

"Other things may change us, but we start and end with family." Anthony Brandt. To my wonderful family, that always supported me and gave the necessary encouragement at times of hardship. Family is the thing that gets us from one good time to the next, always holding your hand through the storms. *"The family is the country of the heart."* Giuseppe Mazzini. Then I give thanks to the paradise that is my country.

"If we value the pursuit of knowledge, we must be free to follow wherever that search may lead us. The free mind is not a barking dog, to be tethered on a ten-foot chain." Adlai E. Stevenson Jr.(1900 - 1965). To my supervisors, Prof. D.G. Kröger and Mr. H.C.R. Reuter, thanks for giving me the freedom at times to explore this sea of knowledge, yet always providing me with an ever fixed mark by which I could navigate.

"To be conscious that you are ignorant is a great step to knowledge." Benjamin Disraeli (1804 - 1881). I acknowledge the fact that the more I study, the more I realise how little I know. But a lesson that I take from my supervisors is that this must never stop us to always venture to gain knowledge.

"True happiness is of a retired nature, and an enemy to pomp and noise; it arises, in the first place, from the enjoyment of one's self, and in the next from the friendship and conversation of a few select companions." Joseph Addison (1672 - 1719). Thank you to all the friends that I have and all the friends that I have made through this time of my life. Thanks to all of you for always being willing to listen. Thank you to Ferdi Zietsman, Dawie Viljoen and Neil van der Merwe for all the discussions that lead to an ideal world and a theoretically perfect wet-cooling tower. A special thanks to Dr Danie de Kock for all his help and expertise, I regard him as a co-supervisor in this thesis. To all the rest that helped me in many ways, thank you.

"For God so loved the world that he gave his one and only Son, that whoever believes in Him shall not perish but have eternal life." To You O Lord I give the most thanks, for it is your doing that gave me all this mentioned above. The greatest joy that this thesis gave me, was that it intensified my walk with the Lord. A code by which I live my life is the *parable of the talents* as told by Jesus. Thank you Lord.

Table of Contents

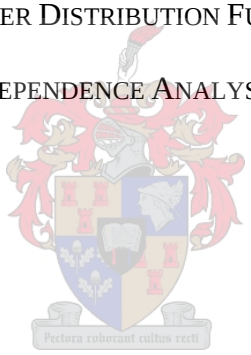

List of Figures

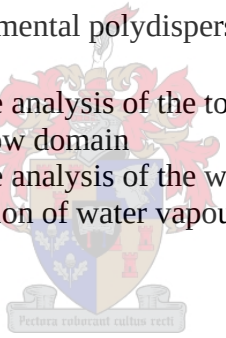

List of Tables

Nomenclature

List of symbols

a	Acceleration, m/s^2
a_1	Constant defined by Equation (3.14), N/m^2K^3
a_2	Constant defined by Equation (3.14), $N/m^2/K^2$
a_3	Constant defined by Equation (3.14), $N/m^2/K$
a_4	Constant defined by Equation (E.11), N/m^2K^2
a_5	Constant defined by Equation (E.11), N/m^2K
a_μ	Constant defined by Equation (7.9)
a_ρ	Constant defined by Equation (7.9)
a_L	Constant defined by Equation (7.9)
a_v	Constant defined by Equation (7.9)
A	Area, m^2; constant defined by Equation (3.16), N/m^2K
b_1, b_2…	Dimensionless constants defined by Equations (2.10), (2.17) and (2.18)
c_p	Specific heat at constant pressure, J/kgK
c_v	Specific heat at constant volume, J/kgK
C	Concentration, kg/m^3; correction factor
C_0	Constant defined by Equation (6.4), kg/m^4
C_1	Constant defined by Equation (6.4)
C_D	Drag coefficient
d	Diameter, m
d_{10}	Average diameter, defined in Table 4.1, m
d_{30}	Mean volume diameter, defined in Table 4.1, m
d_{32}	Sauter mean diameter, defined in Table 4.1, m
d_{41}	Pierce diameter, defined in Table 4.1, m
d_{43}	De Brouckere diameter, defined in Table 4.1, m
d_e	Effective spherical diameter, m
d_m	Maximum stable drop diameter, m
d_{RR}	Mean diameter for Rosin-Rammler, m
d_x	Major axis of prolate ellipsoidal drop, m
d_z	Minor axis of prolate ellipsoidal drop, m
D	Diffusion coefficient, m^2/s
E	Deformation
E_1, E_2…	Constants defined by Equations (2.17) and (2.18), 1/s
F	Force, N
g	Gravitational acceleration, m/s^2
g_{YS}	Correction factor defined by Equation (3.8)
G	Mass velocity, kg/sm^2
h	Heat transfer coefficient, W/m^2K; enthalpy, J/kg
h_D	Mass transfer coefficient, m/s
H	Height, m
I_1, I_2	Constants defined by Equation (3.14), N/m^2K

J	Constant defined by Equation (E.13), N/m^2K
k	Thermal conductivity, W/mK
K	Pressure loss coefficient; constants defined by Equation (2.9)
L	Length, m
m	Mass flow rate, kg/s
M	Mass, kg
n	Spread parameter for Rosin-Rammler
N	Number of diameter intervals
N_d	Number of drops
p	Pressure, N/m^2
Q	Flow rate, m^3/s or ℓ/s; heat transfer rate, W
r	Radius, m; inlet rounding, m
R	Gas constant, J/kgK
s	Path length, m
t	Time, s
T	Temperature, K
v	Velocity, m/s
V	Volt, V; volume, m^3
x	Horizontal coordinate, mm
X	Mass fraction
y	Calibration value, mm/pixel
Y_d	Retained mass fraction
z	Fall distance, m

Greek symbols

α	Constant defined by Equations (2.17) and (2.18), 1/s
α_1, α_2, α_3	Constants defined by Equation (3.14), N/m^2K
α_4, α_5	Constants defined by Equation (E.9), N/m^2K
β	Constant defined by Equations (2.17) and (2.18), 1/s; constant defined by Equation (3.14), N/m^2K
δ	Incremental
Δ	Differential
Φ	Relative humidity; shape factor
η	Dimensionless diameter
θ	Dimensionless temperature; angle, º
κ	Velocity-of-approach factor
μ	Dynamic viscosity, kg/sm
ρ	Density, kg/m^3
σ	Surface tension, N/m
ξ	Constant defined by Equation (3.14)
ψ	Constant defined by Equations (2.17) and (2.18), 1/s
ω	Humidity ratio, kg/kg dry air

Subscripts

a	Air; ambient
ad	Air relative to drop
avg	Average
bt	Bypass trough
B	Buoyancy
c	Counterflow; close
ct	Cooling tower
d	Drop
D	Drag
evap	Evaporated
f	Fraction; far; fluid
fi	Fill inlet
g	Gas
i	Interval; inlet; incremental
lm	Log mean
m	Mixture
mono	Monodisperse drop distribution
n	Nozzle
poly	Polydisperse drop distribution
rz	Rain Zone
s	Sphere; static; saturation
t	Total
ts	Test section
T	Terminal
v	Vapour
w	Water
wb	Wetbulb
wo	Water outlet
YS	Yao-Schrock

Dimensionless groups

Eo	Eotvos number,	$\frac{g(\rho_d - \rho_a)d^2}{\sigma}$
Le	Lewis number,	$\frac{Sc}{Pr}$
Nu	Nusselt number,	$\frac{hd}{k}$
Pr	Prandtl number,	$\frac{c_p \mu}{k}$
Re	Reynolds number,	$\frac{\rho v d}{\mu}$

Sc	Schmidt number,	$\frac{\mu}{\rho D}$
Sh	Sherwood number,	$\frac{h_D d}{D}$

Abbreviations and acronyms

AIChE	American Institute of Chemical Engineers
ASME	American Society of Mechanical Engineers
CFD	Computational fluid dynamics
DPM	Discrete phase model
GUI	Graphic-user-interface
IAHR	International Association of Hydraulic Research
IMechE	Institution of Mechanical Engineers
ODE	Ordinary differential equation
RANS	Reynolds Averaged Navier-Stokes
RHS	Right hand side
SIMPLE	Semi-implicit method for pressure linked equations
STP	Standard temperature and pressure, 20ºC and 101325Pa
UDF	User-defined-function
VDI	Verein Deutscher Ingenieure (Society of German Engineers)

CHAPTER

1

Introduction

In conventional fossil fuelled power plants less than half of the thermal energy supplied is converted to electric power, most of the rest is waste energy and needs to be rejected to the surroundings by means of a cooling system.

Many of the earlier power plants made use of once-through cooling, where water is taken from a natural source e.g. sea, rivers, lakes etc. and then heated and returned back to the source. Ecological awareness and regulations instated in the *1970s* have prohibited the use of such cooling systems in many areas. Thus alternatives such as wet-cooling towers had to be found to solve the cooling problem.

A wet-cooling tower facilitates the cooling of warm process water by bringing it into direct contact with colder dry air. The main cooling mechanisms are sensible heat transfer and evaporation due to mass transfer, which are strongly dependent on the interfacial area and the contact time. Ways to increase the heat and mass transfer is to make use of fill (splash, trickle or film type). These can be installed in either counterflow or crossflow configurations which can be distinguished by the direction of the air flow relative to the water flow.

For the case of a natural draught cooling tower, the air flow is achieved by means of buoyancy due to the difference in density between the cold air outside and the warm moist air inside the cooling tower, whereas in a mechanical draught cooling tower the air flow is provided by a fan.

1.1 Background

Rish [1961RI1] was one of the first to include the rain zone in his analysis of counterflow cooling towers. Prior studies ignored the rain zone, considering it to be unimportant or too complex to analyse. However, in large counterflow wet-cooling towers as much as *10-20%* of the total heat is rejected in the rain zone, thus knowledge of the characteristics of the rain zone is important for reliable prediction of the total performance. This substantiates that the rain zone can not be ignored in any detailed analysis of a wet-cooling tower.

Limited published literature is available on the mathematical modelling of the heat and mass transfer from free-falling sprays consisting of large drops. The simpler models for describing drop cooling invariably assume that the polydisperse drop distribution can be expressed by a single representative drop diameter known as a monodisperse drop distribution. Hollands [1974HO1]

modelled the operation of a spray cooling tower mathematically, and concluded that a monodisperse drop distribution is desirable and that the drop diameter should be as small as *1-2mm*. Warrington and Musselman [1983WA1] reached the same conclusion in comparing the performance of a monodisperse drop distribution to a polydisperse drop distribution. Alkidas [1981AL1] and Aggarwal [1988AG1] found that the Sauter mean diameter can be used to calculate the heating of a polydisperse drop distribution. Hollands and Goel [1976HO1] showed analytically that it is not generally possible to use a monodisperse drop distribution to model the cooling or heating of a polydisperse drop distribution. They found that a monodisperse drop distribution can be used in the following cases: (i) when the particles move through the heat/mass exchanger so rapidly that they do not change appreciably in temperature or (ii) when the drops are very small and represent a small mass in comparison to the air stream. Dreyer [1994DR1] reviewed relevant literature and concurs with this hypothesis.

Lowe and Christie [1961LO1] derive the mass transfer and the pressure drop for counterflow conditions, assuming that no drop collisions or agglomeration occur. Their data is applicable to small drops only and the drops fall at their terminal velocity. In most towers, large drops may never reach their terminal velocity.

Hollands [1974HO1] included the effect of drop deformation on the drag and the heat and mass transfer experienced by the drops in his mathematical model. De Villiers and Kröger [1998DE1] include drop deformation in their determination of the rain zone loss coefficient and Merkel number. Fisenko et al. [2004FI1] exclude drop deformation in the development of their mathematical model of a mechanical draught cooling tower performance. They do not determine the pressure drop over the rain zone with their model and confine themselves to modelling the change in the drop's velocity, its diameter and temperature, and also a change in the temperature and density of the air-vapour mixture in a cooling tower. De Villiers and Kröger [1998DE1] use a monodisperse drop distribution in their model, whereas Fisenko et al. [2004FI1] are able to model polydisperse drop distributions.

With the aid of modern computers the differential Navier-Stokes, continuity and energy equations for a two-phase flow can be solved numerically. Benton and Rehberg [1986BE1] conducted a numerical investigation of the rain zone of a counterflow and a pure crossflow configuration. Williamson et al. [2006WI1] used FLUENT to simulate a two-dimensional axisymmetric two-phase simulation of the heat and mass transfer inside a natural draught wet-cooling tower. They used a monodisperse drop distribution with a drop diameter of *2.5mm*.

1.2 Motivation

The motivations for this thesis can be divided into three distinctive sections: financial, environmental and academic.

From an economical and engineering vantage point it is imperative that all systems should meet design performance. It should be known that small significant improvements to a cooling system of a power plant could result in a multi-million dollar saving in resources. Improving the rain zone performance can reduce the life cycle costs of natural draught wet-cooling towers.

Improving the rain zone performance of natural draught wet-cooling towers can also be beneficial to the environment. Such improvements include reducing water consumption and plant emissions.

The academic motivation for this thesis is to gain a sound understanding of the physics of the rain zone. This understanding will help accomplish the prior motivations.

These motivations are incentives to continually improve these systems worldwide by conducting research and development.

1.3 Objectives

This thesis concentrates solely on the processes found in the rain zone of a wet-cooling tower. Counterflow and cross-counterflow rain zone configurations are investigated, with emphasis on the latter found in natural draught wet-cooling towers.

Validation of the proposals, ideas and hypotheses put forward by prior researchers, as highlighted in Section 1.2, together with the motivations given in the previous section give rise to the objectives of this thesis:

1. Investigate the influence of drop diameter and drop deformation on the velocity, path length and cooling of single water drops vertically free-falling through stagnant or upward flowing air.
2. Assist with the design, draughting, manufacture, installation, calibration and testing of a new rain zone test facility.
3. Determine the inlet drop size distribution and the pressure drop of a counterflow rain zone experimentally for different air and water mass flow rates.
4. Develop CFD models to predict the pressure drop and the heat and mass transfer of a counterflow and cross-counterflow rain zone.
5. Investigate the performance uncertainty produced by using the Rosin-Rammler drop distribution function as opposed to discrete drop distribution data when modelling the performance of the rain zone.
6. Investigate the feasibility of modelling rain zones by assuming a constant drop diameter and establish which diameter definition is the most representative of a particular polydisperse drop distribution.
7. Using the CFD models developed in this thesis, validate the correlations for the rain zone performance characteristics proposed by De Villiers and Kröger [1998DE1].

1.4 Approach and Layout of Thesis

This section presents the basic layout of this thesis and provides a short synopsis for each chapter.

CHAPTER 1. INTRODUCTION
Chapter 1 gives a brief description of cooling towers. It presents the motivation, objectives and the layout of the thesis.

CHAPTER 2. DROP VELOCITY AND PATH LENGTH
This chapter is used to gain an understanding of the physics of the motion of drops free-falling through air and then also to provide data to validate CFD models. The effect of drop deformation on the velocity and path length of a drop is investigated.

CHAPTER 3. DROP HEAT AND MASS TRANSFER
This chapter is used to gain an understanding of the physics of the cooling of drops free-falling through air and then also to provide data to validate CFD models.

CHAPTER 4. EXPERIMENTAL DATA ACQUISITION
Experimental work of a one-dimensional counterflow case is performed in order to obtain pressure drop and drop size distribution data necessary to validate CFD models. The relevant data for the pressure drop and drop distribution is presented at the end of this chapter.

CHAPTER 5. EFFECT OF DROP DEFORMATION ON RAIN ZONE PERFORMANCE
The effect of drop deformation on rain zone performance is investigated.

CHAPTER 6. CFD MODEL OF THE RAIN ZONE
CFD models are created that can be used to model polydisperse and monodisperse drop distributions, with regards to the loss coefficient and Merkel number. The results of the simulations for the polydisperse drop distributions are given.

CHAPTER 7. MODELLING RAIN ZONE LOSS COEFFICIENT
This chapter will investigate the modelling of a polydisperse drop distribution by means of a monodisperse drop distribution with regards to the loss coefficient, and in doing so define a new representative diameter. CFD is then used to validate the mathematical correlations for the rain zone loss coefficient given by De Villiers and Kröger [1998DE1].

CHAPTER 8. MODELLING RAIN ZONE HEAT AND MASS TRANSFER
This chapter will investigate the modelling of a polydisperse drop distribution by means of a monodisperse drop distribution with regards to the Merkel number. The mathematical correlations for the rain zone Merkel number presented by De Villiers and Kröger [1998DE1] will be validated with CFD.

CHAPTER 9. CONCLUSIONS AND RECOMMENDATIONS
This chapter is used to present the conclusions and recommendations that stem from the work done in this thesis.

CHAPTER

2

Drop Velocity and Path Length

This chapter is used to gain an understanding of the physics of the motion of drops vertically free-falling through air and then also to provide data to validate CFD models. To this end, the chapter sets out to present the derivation of the governing equation of motion of a vertically free-falling drop in an incompressible Newtonian fluid. Different solution techniques, namely analytical, numerical and CFD (FLUENT 6.2.16) are employed to solve the ordinary differential equations and the results are compared. Finally the effect of drop deformation on the velocity and path length of a drop is investigated.

2.1 Mathematical Model

Consider a drop vertically free-falling under the action of gravity through stagnant air or a counterflow air stream.

Referring to Figure 2.1, the equation of motion of a drop can be found, by applying Newton's second law, defined by

$$\sum F = M_d g - F_B - F_D = M_d a_d \tag{2.1}$$

where M_d denotes the mass of the drop, a_d the acceleration and F_D and F_B are the drag and buoyancy forces defined by Equations (2.2) and (2.3) respectively.

$$F_D = \frac{1}{2}\rho_a v_{ad}^2 A_d C_D \tag{2.2}$$

$$F_B = M_a g \tag{2.3}$$

Where v_{ad} is the velocity of the air relative to the drop, A_d its cross-sectional area, C_D the drag coefficient and M_a is the mass of the displaced air. The relative velocity of the air to the drop is given by,

$$v_{ad} = |v_a - v_d| \tag{2.4}$$

where v_a and v_d are the air and the drop velocities respectively.

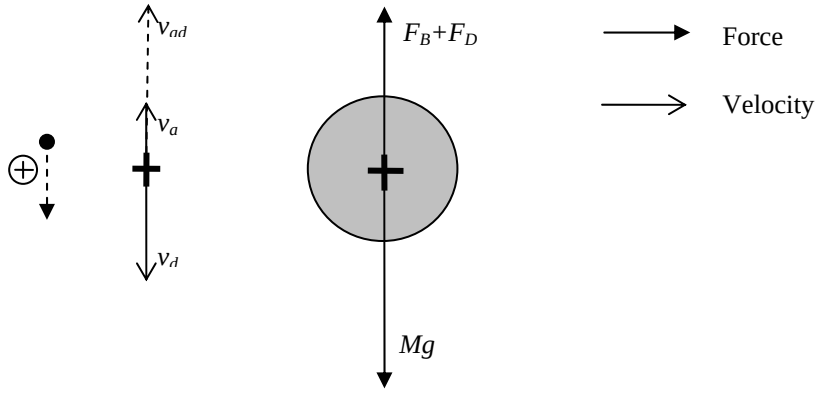

Figure 2.1: Free-body-diagram of a drop in a counterflow air stream.

Substitution of Equations (2.2) and (2.3) into Equation (2.1) and rewriting all dependent variables in terms of their independent variables yields,

$$\frac{dv_d}{dt} = \frac{(\rho_d - \rho_a)}{\rho_d} g - \frac{3\rho_a}{4\rho_d d_d} C_D v_{ad}^2 \tag{2.5}$$

In this chapter it is assumed that the temperature and diameter of the drop remain constant. The variation of these variables is addressed in Chapter 3.

2.1.1 Drag Coefficient

Turton and Levenspiel [1986TU1] propose a correlation to represent the drag coefficient for spheres. A reformulation of the single equation correlation is given by,

$$C_D = \frac{24}{Re} + \frac{4.152}{Re^{0.343}} + \frac{0.413}{1+16300\,Re^{-1.09}} \quad \text{for } Re \le 200\,000 \tag{2.6}$$

Referring to Equation (2.6) and Figure 2.2, the first term on the right-hand-side denotes Stokes' law, the second term represents the transition of the drag curve to the near constant portion for high Reynolds numbers, represented by the last term.

Using the same data, Clift et al. [1978CL1] present a set of 10 polynomial regressions applicable to different Reynolds number ranges to represent the drag coefficient for spheres, given in Table 2.1.

Table 2.1: Clift et al. [1978CL1] drag coefficient correlations, $w = log_{10}Re$.

Reynolds number range	Drag coefficient correlation
$\mathrm{Re} < 0.01$	$C_D = \frac{24}{\mathrm{Re}} + \frac{3}{16}$
$0.01 < \mathrm{Re} \le 20$	$C_D = \frac{24}{\mathrm{Re}}\left[1 + 0.1315\,\mathrm{Re}^{(0.82-0.05w)}\right]$
$20 \le \mathrm{Re} \le 260$	$C_D = \frac{24}{\mathrm{Re}}\left[1 + 0.1935\,\mathrm{Re}^{0.6305}\right]$
$260 \le \mathrm{Re} \le 1500$	$\log_{10} C_D = 1.6435 - 1.1242w + 0.1558w^2$
$1.5\times10^3 \le \mathrm{Re} \le 1.2\times10^4$	$\log_{10} C_D = -2.4571 + 2.5558w - 0.9295w^2 + 0.1049w^3$
$1.2\times10^4 < \mathrm{Re} < 4.4\times10^4$	$\log_{10} C_D = -1.9181 + 0.637w - 0.0636w^2$
$4.4\times10^4 < \mathrm{Re} \le 3.38\times10^5$	$\log_{10} C_D = -4.339 + 1.5809w - 0.1546w^2$
$3.38\times10^5 < \mathrm{Re} \le 4\times10^5$	$C_D = 29.78 - 5.3w$
$4\times10^5 < \mathrm{Re} \le 1\times10^6$	$C_D = 0.1w - 0.49$
$1\times10^6 < \mathrm{Re}$	$C_D = 0.19 - \frac{8\times10^4}{\mathrm{Re}}$

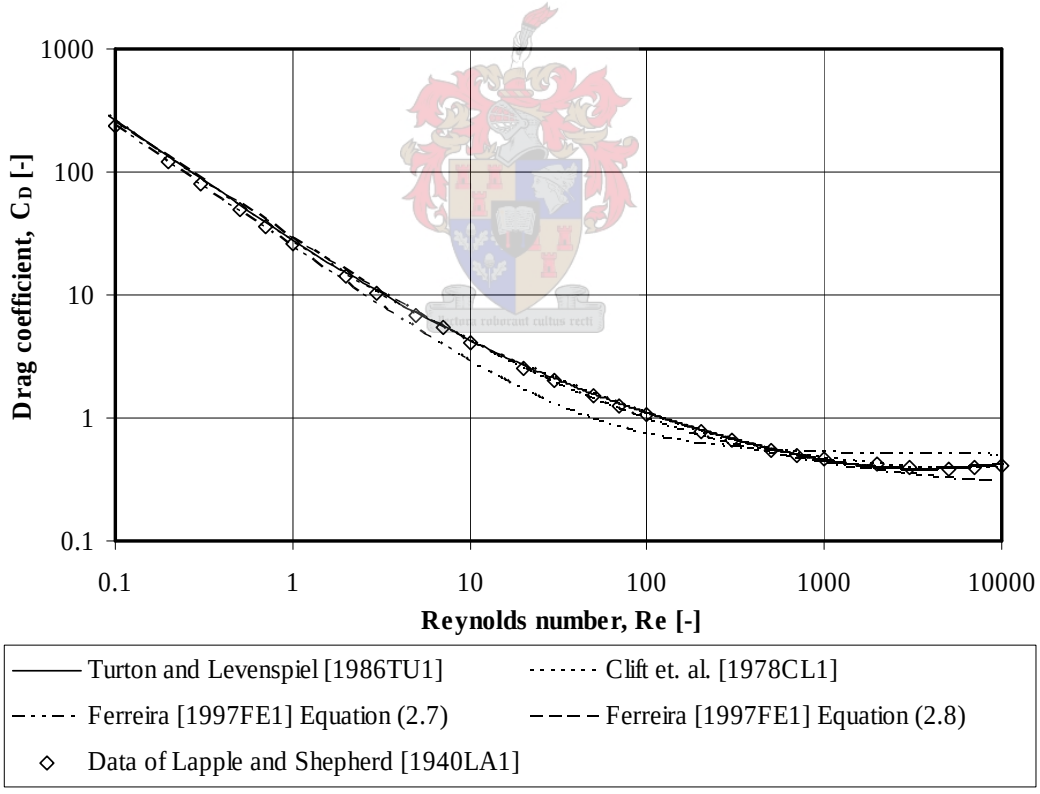

Figure 2.2: Drag coefficient of a sphere as a function of Reynolds number.

Ferreira [1997FE1] proposes two correlations, Equations (2.7) and (2.8), for the drag coefficient in order to solve Equation (2.5) for a sphere analytically.

$$C_D = \frac{24}{Re} + 0.5 \tag{2.7}$$

$$C_D = \left(\frac{4.9}{Re^{1/2}} + 0.5 \right)^2 \tag{2.8}$$

FLUENT Documentation [2003FL1] incorporate the following correlation for the drag coefficient of smooth spheres given by Morsi and Alexander [1972MO1],

$$C_D = K_1 + \frac{K_2}{Re} + \frac{K_3}{Re^2} \tag{2.9}$$

where K_1, K_2 and K_3 are constants that are applicable to certain Reynolds number ranges, given in Table 2.2.

Table 2.2: Constants of Equation (2.9) and their applicable Reynolds number ranges.

Reynolds number range	K_1	K_2	K_3
Re < 0.1	0	24	0
0.1 < Re < 1	3.69	22.73	0.0903
1 < Re < 10	1.222	29.1667	-3.8889
10 < Re < 100	0.6167	46.5	-116.67
100 < Re < 1000	0.3644	98.33	-2778
1000 < Re < 5000	0.357	148.62	-4.75×10^4
5000 < Re < 10000	0.46	-490.546	57.87×10^4
10000 < Re < 50000	0.5191	-1662.5	5.4167×10^6

FLUENT Documentation [2003FL1] also incorporates another correlation, proposed by Haider and Levenspiel [1989HA1], which includes a shape factor,

$$C_D = \frac{24}{Re}\left(1 + b_1 Re^{b_2}\right) + \frac{b_3 Re}{b_4 + Re} \tag{2.10}$$

where

$$ln(b_1) = 2.3288 - 6.4581\phi + 2.4486\phi^2$$

$$b_2 = 0.0964 + 0.5565\phi$$

$$ln(b_3) = 4.905 - 13.8944\phi + 18.4222\phi^2 - 10.2599\phi^3$$

$$ln(b_4) = 1.4681 + 12.2584\phi - 20.7322\phi^2 + 15.8855\phi^3$$

The shape factor, Φ, is defined as the ratio of the surface area of a sphere, having the same volume as the drop, to the actual surface area of the drop. Equation (2.10) is similar in form to Equation (2.6).

Gunn and Kinzer [1949GU1], Beard and Pruppacher [1969BE1] and Ryan [1976RY1] measured the terminal velocities of water drops in air. They all show a marked difference from the terminal velocity predicted by using drag correlations for spheres. Gunn and Kinzer [1949GU1] measured the velocity of water drops at $20^{\circ}C$ falling in stagnant air at STP. Refer to Figure 2.3.

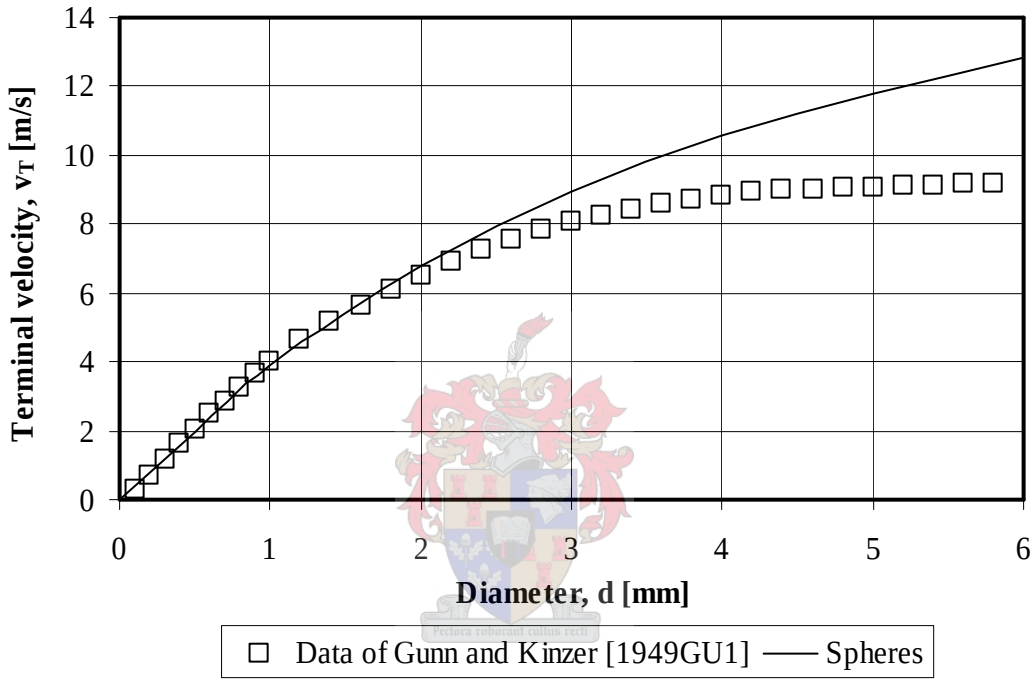

Figure 2.3: Terminal velocity as a function of drop diameter, for experimental water drops and spheres.

The drag experienced by liquid drops is mainly influenced by internal circulation, drop oscillation and drop deformation.

Internal circulation reduces the skin friction that a liquid drop experiences thus reducing the drag. LeClair et al. [1972LE1] found that the effect that internal circulation has on the drag of a water drop to be less than *1%*.

Beard [1977BE1] and Pruppacher and Klett [1978PR1] concluded that the oscillation frequency of water drops is too high for drop oscillation to have a noticeable effect on drop drag in the absence of air turbulence.

It can therefore be concluded that the main reason for the difference in drag between spheres and drops must therefore be due to drop deformation.

2.1.2 Drop Deformation

Drop deformation is defined as the aspect ratio of a prolate ellipsoidal drop, written as,

$$E = \frac{d_z}{d_x} \tag{2.11}$$

where d_z and d_x are defined as shown in Figure 2.4. Beard and Chuang [1987BE1] formulated a numerical model that predicts the deformation at drop terminal velocity in stagnant air. The deformation caused by drag can be obtained by numerically solving the appropriate Laplace equation. An empirical equation proposed by Dreyer [1994DR1] fits their data, expressed by,

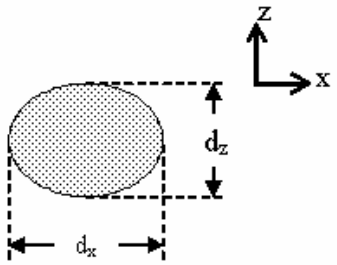

Figure 2.4: Representation of a deformed drop.

$$E_T = \frac{1}{1+0.148Eo^{0.85}} \tag{2.12}$$

where the Eotvos number, *Eo*, is defined by,

$$Eo = \frac{gd_d^2\left(\rho_d - \rho_a\right)}{\sigma_d} \tag{2.13}$$

Dreyer [1994DR1] proposed a correlation for drop deformation during drop acceleration as a function of velocity, terminal velocity (v_T) and terminal deformation, given by,

$$E = 1 - \left(\frac{v_d}{v_T}\right)^2 \left(1 - E_T\right) \tag{2.14}$$

He also proposed a correlation, which expresses the ratio of drop and sphere drag coefficients as a function of drop deformation, given by

$$\frac{C_D}{C_{D,sphere}} = 1 - 0.17185\left(1-E\right) + 6.692\left(1-E\right)^2 - 6.605\left(1-E\right)^3 \tag{2.15}$$

where $C_{D,sphere}$ is calculated using Equation (2.6).

The drop drag coefficient in the correlation above is based on the actual frontal area of the deformed drop and the Reynolds number is based on the

equivalent spherical drop diameter, where the equivalent spherical drop diameter is the diameter of a sphere that has the same volume as the actual drop.

Equation (2.10) includes drop deformation, however the value for the shape factor stays constant throughout the drop's lifetime and this implies that the equation does not take into account changes in drop deformation which occur during drop acceleration. Incorporation of Equation (2.15) in FLUENT 6.2.16 would be computationally expensive. The author therefore proposes a correlation that is a function of the Reynolds number and the terminal deformation of the drop. The derivation of Equation (2.16) is given in Appendix B.

$$C_D = \frac{23.986}{Re} + \frac{4.186}{Re^{0.343}} + \left(1.28\times10^{-6} E_T^{2.017} - 1.75\times10^{-6} E_T + 7.07\times10^{-7}\right) Re^{1.831} \tag{2.16}$$

2.2 Solution Techniques

The different solution techniques that are employed to solve Equation (2.5), together with their assumptions, for the determination of the velocity and path length of a drop falling through stagnant air or a counterflow air stream are presented in this section.

2.2.1 Analytical

For the analytical solution it is assumed that the drop remains spherical for its entire path length, it falls in stagnant air and the drop has no effect on the air. This means that the spherical drag correlation, Equation (2.6), is employed. The subscript *s* is now used to denote the spherical drop case.

Analytical solutions for the velocity and path length as a function of time are found and given below,

$$v_s = \frac{\mu_a}{2\rho_a d_s E_1}\left(\psi \tan\left(\frac{\psi\left(t-t_0\right)}{2} + \tan^{-1}\left(\frac{2\rho_a d_s E_1 v_{s,0} + \mu_a E_2}{\mu_a \psi}\right)\right) - E_2\right) \tag{2.17}$$

$$s_s = -\frac{1}{2}\mu_a \frac{-\ln\left(\sec^2\left(\frac{1}{2}\psi\left(t-t_0\right) + \tan^{-1}\left(\frac{2\rho_a d_s E_1 v_{s,0} + E_2\mu_a}{\mu_a\psi}\right)\right)\right) + E_2 t}{\rho_a d_s E_1} + \frac{1}{2}\mu_a \frac{-\ln\left(\sec^2\left(\tan^{-1}\left(\frac{2\rho_a d_s E_1 v_{s,0} + E_2\mu_a}{\mu_a\psi}\right)\right)\right) + E_2 t_0}{\rho_a d_s E_1} \tag{2.18}$$

where

$$\alpha = \frac{\rho_a d_s}{\mu_a}\left(1-\frac{\rho_a}{\rho_s}\right)g$$

$$\beta = -\frac{3\mu_a}{4{d_s}^2\rho_s}$$

$$E_1 = b_1\beta$$

$$E_2 = b_2\beta$$

$$E_3 = \alpha + b_3\beta$$

$$\psi = \left(4E_3E_1 - E_2^2\right)^{1/2}$$

and t_0 and $v_{s,0}$ are the initial time and velocity respectively. The values for the constants and their applicable Reynolds number ranges are given in Table 2.3.

Table 2.3: Values of constants of parabolic equation for C_DRe^2 as a function of Reynolds number.

Reynolds number range	b_1	b_2	b_3
$0 \leq Re \leq 275$	0.409	75.837	-674.48
$275 \leq Re \leq 900$	0.378	97.931	-4714.1
$900 \leq Re \leq 1750$	0.359	142.33	-30791
$1750 \leq Re \leq 2750$	0.354	140.25	-12434
$2750 \leq Re \leq 4000$	0.377	10.257	172402
$4000 \leq Re \leq 10000$	0.474	-961.02	2604768

The analytical solution presents an expression for the time required to reach terminal velocity,

$$t_{transient} = \frac{2\rho_s d_s}{3b_1\rho_a} \tag{2.19}$$

The reader is referred to Appendix C for a full derivation of Equations (2.17) and (2.18).

2.2.2 Numerical

For the purposes of this thesis, a numerical program was written that can solve the equations of motion, Equation (2.5), for a vertically free-falling drop in an incompressible Newtonian fluid, using the 4th order Runge-Kutta numerical integration technique. The effect of drop deformation on the drag can be incorporated using Equation (2.15) or Equation (2.16). The effect of the drop on the continuous phase is not considered, thus the continuous phase remains undisturbed.

2.2.3 Computational Fluid Dynamics

FLUENT 6.2.16 models the drops by means of a discrete phase model (DPM), utilising a Lagrangian approach in which the momentum equation is written in a co-ordinate system that moves with each individual drop. The continuous phase equations are still expressed in their Eulerian continuum form, but are suitably modified to account for the presence of the drops, by means of interphase source terms.

The user is presented with the option to include interphase interaction. In the event that the interaction is included, then the conservation of momentum states that a change in momentum of the drop will result in a change in momentum of the continuous phase. This interaction is accounted for by appropriate interphase source terms in the continuous phase momentum equations.

FLUENT 6.2.16 can solve Equation (2.5) using a number of numerical integration techniques: implicit Euler integration; semi-implicit trapezoidal integration; analytical integration and a 5^{th} order Runge-Kutta technique.

The effect of the drops on the turbulence equations of the continuous phase can be modelled with FLUENT 6.2.16 using two-way turbulence coupling.

2.3 Analysis of Results

The next section compares and discusses the results obtained by employing the different solution techniques. For the solution techniques to be comparable the simulation conditions are identical. For this reason this section is sub-divided into two sections. The first section, *spherical drops*, will compare all the prior discussed solution techniques for the case of a spherical drop falling in stagnant air. The second section, *deformable drops*, will be used to compare the solution techniques of CFD and the numerical model for the case of a deformable drop falling in a counterflow air stream.

2.3.1 Spherical drops

The analytical results are used as reference values, to which the numerical and CFD results are compared.

The analytical drop velocity and path length data are presented in Figures 2.5 and 2.6 respectively. Equation (2.19) is also plotted in Figure 2.5.

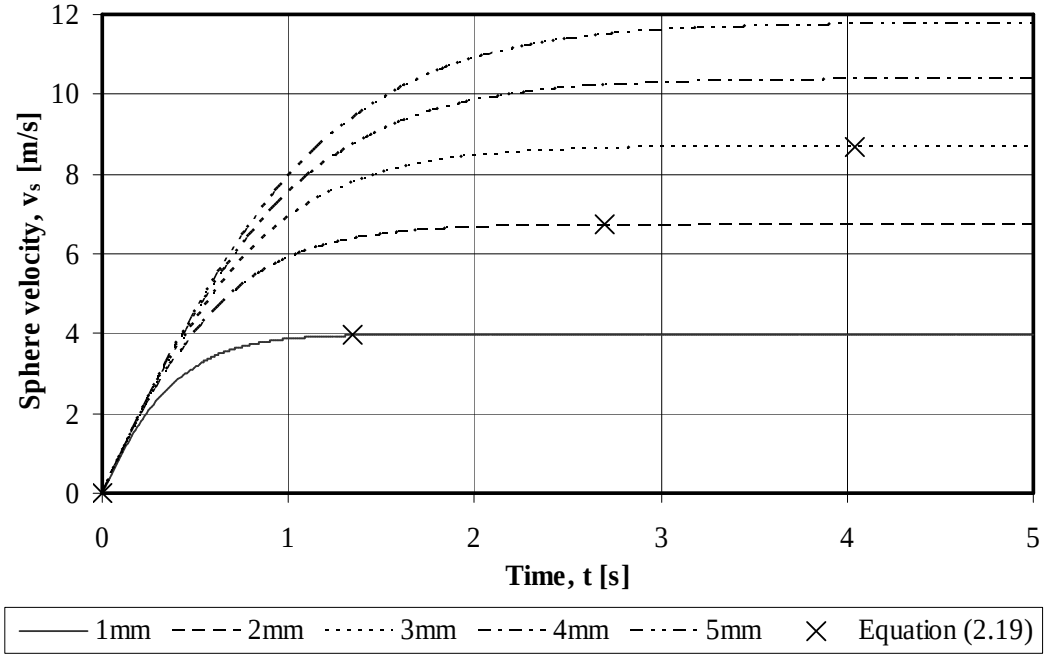

Figure 2.5: Velocity of a sphere as a function of time, Equation (2.17).

Figure 2.5 correctly shows that all the spheres have the same initial gradient, gravitational acceleration. The figure also shows that the larger spheres attain a larger velocity value, thus they would fall through a rain zone faster.

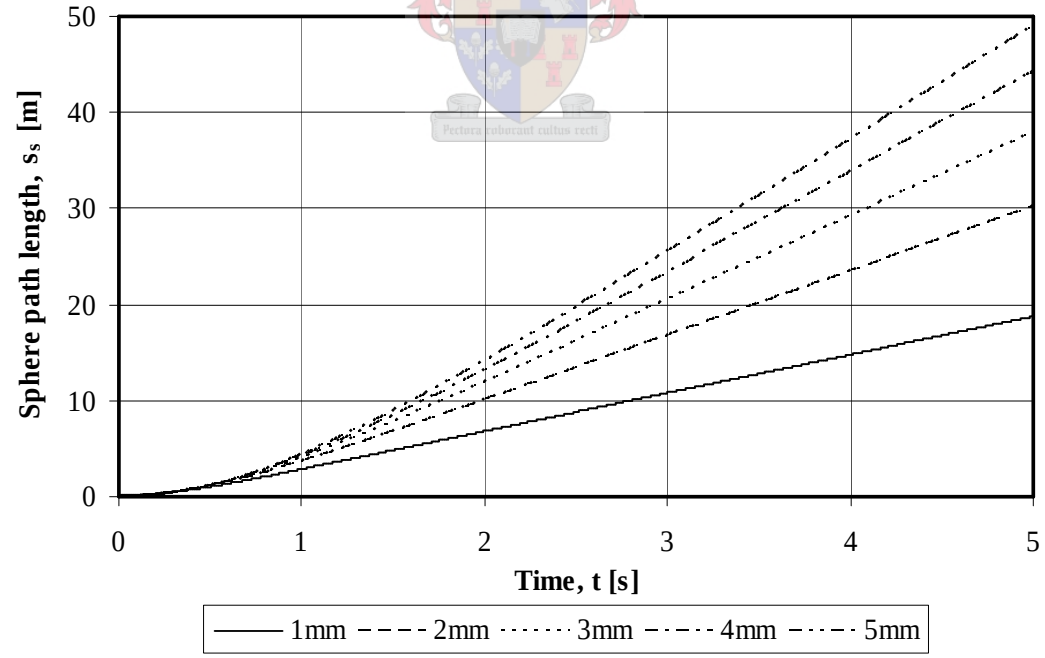

Figure 2.6: Path length of a sphere as a function of time, Equation (2.18).

Figure 2.6 shows that the larger drops take less time to attain any corresponding path length value, thus for the rain zone example this would mean less contact time between the drop and the air. The gradients of the curves in Figure 2.6 become constant at the onset of terminal velocity.

Figures 2.7 and 2.8 are used to present the results of the comparison between the solution procedures, with respect to velocity and path length.

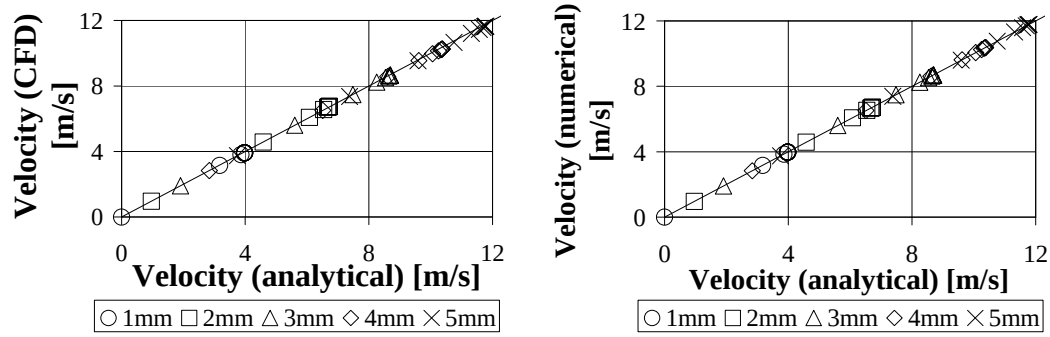

(a) (b)

Figure 2.7: Numerical and CFD spherical drop velocity data plotted against corresponding analytical data for comparison of the results.

Figure 2.7 shows good correspondence between the results from the different solution techniques. For a *5mm* sphere there is *1%* deviation between the analytical and the CFD results and between the analytical and the numerical results a *0.04%* deviation exists. The deviations can be attributed to the different drag coefficient correlations implemented. The analytical and the numerical solution techniques implement Equation (2.6), whereas the CFD solution technique implements Equation (2.9).

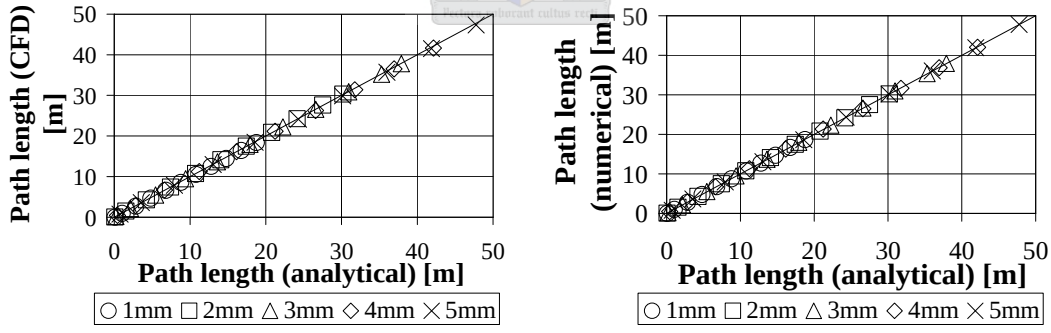

(a) (b)

Figure 2.8: Numerical and CFD spherical drop path length data plotted against corresponding analytical data for comparison of results.

For the path length, the values for the deviations remain relatively unchanged.

This section demonstrates that analytical, CFD and numerical solution techniques can be used to predict the velocity and path length of a vertically free-

falling spherical drop. It is seen that CFD deviates marginally from the analytical model due to the different drag correlation incorporated.

2.3.2 Deformable drops

Figure 2.9 illustrates the deviation in the terminal velocity between the experimental data of Gunn and Kinzer [1949GU1] and results obtained using various drag coefficient correlations.

The same order of accuracy is obtained for drop diameters in the range $0 \leq d_d \leq 2mm$. Beyond this range the terminal velocities of spheres and drops begin to deviate significantly from each other.

Kröger [1998KR1] states that generally splash type fills produce a spectrum of relatively small drops in the rain zone (*3mm – 4mm*) while film and trickle fills produce larger drops (*5mm – 6mm*). Figure 2.9 illustrates that neither of these two ranges are accurately predicted by spheres regarding terminal velocity.

Therefore it can be stated: in order to accurately predict the terminal velocity of water drops and ultimately rain zone performance, it is imperative to employ equations that incorporate the effect of drop deformation on drag.

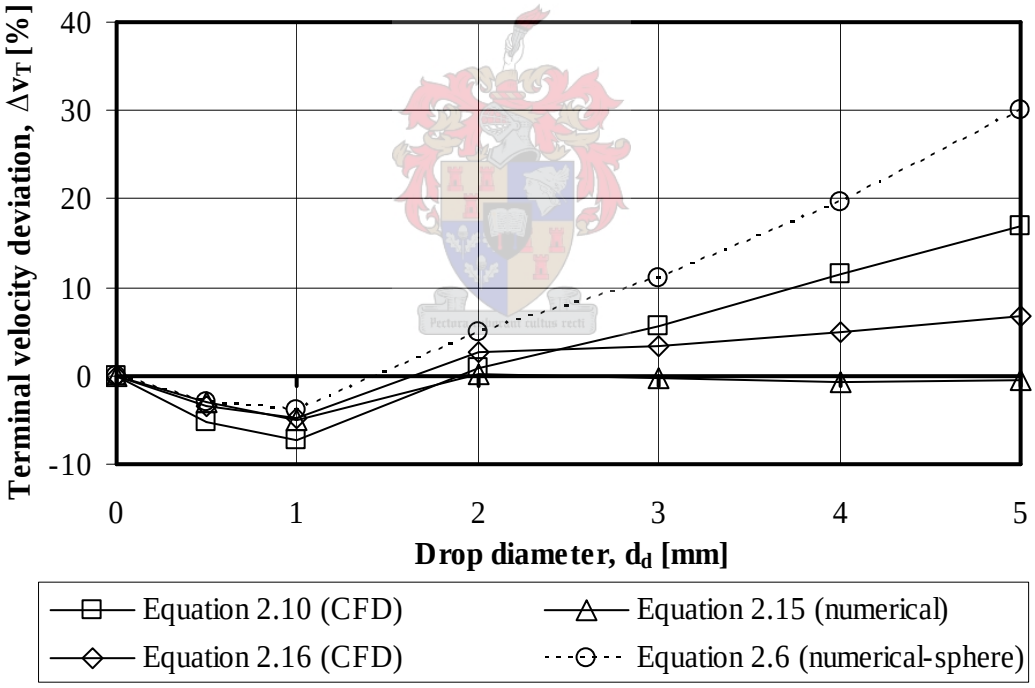

Figure 2.9: The deviation between experimental terminal velocity data [1949GU1] and numerical and CFD data obtained by employing different drag coefficient correlations.

Figure 2.10 illustrates that an increase in counterflow air velocity reduces the absolute terminal velocity of a drop which results in a shorter path length for a

given period of time. The absolute terminal velocity of a drop falling in a counterflow air stream can be written as,

$$v_{T,c} = v_{T,c0} - v_a \tag{2.20}$$

where $v_{T,c}$ and $v_{T,c0}$ are the absolute terminal velocities with and without a counterflow air velocity respectively.

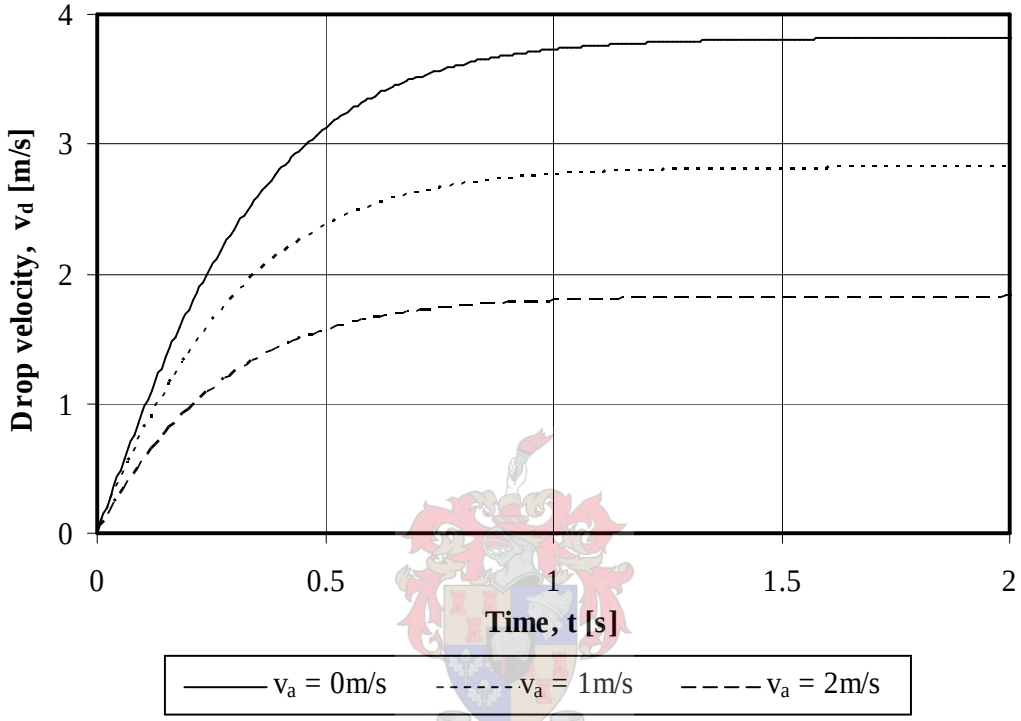

Figure 2.10: Velocity of a *1mm* drop as a function of time for various counterflow air velocities.

Summary

Literature shows that internal circulation, drop oscillation and drop deformation have an effect on the drag experienced by a drop, but that deformation is the most significant.

An analytical solution is proposed to determine the velocity and path length of vertically free-falling spherical drops in stagnant air. The results are compared with corresponding results obtained numerically and by means of CFD and the deviations are within *0.04%* and *1%* respectively.

Experimental data showed that the terminal velocity of larger liquid drops and liquid spheres differed somewhat due to drop deformation. FLUENT 6.2.16 provides the option to use a correlation for drag coefficient which accommodates fixed drop deformation, yet it was found to deliver unsatisfactory results for

certain drop sizes. Consequently a new correlation was developed with which better results were obtained.

It was shown that increasing counterflow air velocity reduces the absolute terminal velocity, this results in shorter path lengths for a specified time.

It was shown that the drop diameters that are associated with a rain zone are all affected by drop deformation and thus it can not be ignored when determining the velocity and path length of drops in the rain zone. Also for the typical heights associated with rain zones these drop diameters hardly ever reach their terminal velocities, thus spending most of their lifetime in their transient velocity stage. Very little literature exists on the transient velocity stage of deformable drops, thus no direct comparison can be drawn. However, with the fixed initial gradient in the velocity *vs.* time graph and a correct prediction of the terminal velocity an accurate prediction of the transient velocity stage of a drop's lifetime can be found.

CHAPTER

3

Drop Heat and Mass Transfer

This chapter is used to gain an understanding of the physics of the cooling of drops vertically free-falling through air and then also to provide data to validate CFD models. To this end, the chapter sets out to present the derivation of the governing equations for the rate of temperature change of a vertically free-falling drop in an incompressible Newtonian fluid. Different solution techniques to solve these ordinary differential equations, namely analytical, numerical and CFD (FLUENT 6.2.16), are employed and the results for the change in drop temperature and diameter are then compared for various conditions.

3.1 Mathematical Model

There are mainly three different models for the transport processes inside a drop. The *complete mixing model* assumes complete mixing and therefore constant temperature along the radius of the drop. Resistance to heat and mass transfer therefore only exists in the continuous phase. The *non-mixing model* assumes a temperature gradient along the radius, giving rise to transient heat transfer inside the drop due to conduction. The *mixing model* considers both the effects of oscillation and internal circulation on the mixing in the drop. The *non-mixing* and *mixing models* require that the internal temperature gradient of a drop, *inter alia*, be modelled, resulting in extra computational time per drop. FLUENT 6.2.16 employs the *complete mixing model*, which is adopted for this thesis.

Heat and mass transfer are the two main driving mechanisms for energy transfer between a water drop and air, which ultimately relates to a change in the temperature and the diameter of the drop. The driving potential for mass transfer is the concentration difference of water vapour at the drop surface and in the air, defined by,

$$\frac{dM_d}{dt} = -h_D A_d \left(C_d - C_a \right) \tag{3.1}$$

where, A_d is the surface area of the drop, C_d and C_a are the concentrations of water vapour at the surface of the drop and in the air respectively and h_D is the mass transfer coefficient, that is determined from the Sherwood number, *Sh*, given by

$$h_D = \frac{Sh\, D}{d_d} \tag{3.2}$$

where D is the diffusion coefficient.

Concerning the heat transfer, it was assumed that the radiation heat transfer is negligible, thus the heat transfer is due to convection only. The driving potential for the convection heat transfer is the temperature difference that exists between the drop surface and the air. Assuming uniform drop temperature, the convection heat transfer is represented by Newton's law of cooling defined by,

$$Q_c = hA_d \left(T_a - T_d\right) \tag{3.3}$$

where, h is the convection heat transfer coefficient that is determined from the Nusselt number, Nu, given by

$$h = \frac{k_a Nu}{d_d} \tag{3.4}$$

where k_a is the thermal conductivity of the air.

From the first law of thermodynamics for an unsteady flow process, applied to a control volume around a drop, and substitution of Equations (3.1) and (3.3) results in the energy equation for a drop free-falling in an incompressible Newtonian fluid, expressed by,

$$\frac{d}{dt}\left(M_d c_v T_d\right) = M_d c_v \frac{dT_d}{dt} + c_v T_d \frac{dM_d}{dt} = hA_d \left(T_a - T_d\right) - h_D A_d \left(C_d - C_a\right) h_g$$

hence

$$\frac{dT_d}{dt} = \frac{hA_d}{M_d c_v}\left(T_a - T_d\right) - \frac{h_D A_d}{M_d c_v}\left(C_d - C_a\right) h_{fg} \tag{3.5}$$

Solution of Equation (3.5) results in a relation for drop temperature as a function of time, drop diameter and thermophysical properties. For the change in the diameter of the drop as a function of time Equation (3.1) must be solved.

3.1.1 Heat and Mass Transfer Coefficients

Heat and mass transfer of liquid drops has been studied extensively by numerous researchers; Frossling [1938FR1], Snyder [1951SN1], Ranz and Marshall [1952RA1], Hsu et al. [1954HS1], Yao and Schrock [1976YA1], Miura et al. [1977MI1] and Srikrishna et al. [1982SR1].

Ranz and Marshall [1952RA1] conducted their studies using small drops suspended on thin wires/fibres, subject to a constant velocity air stream. They proposed the following correlations for the heat and mass transfer,

$$Nu = 2 + 0.6\, Re^{1/2}\, Pr^{1/3} \tag{3.6}$$
$$Sh = 2 + 0.6\, Re^{1/2}\, Sc^{1/3} \tag{3.7}$$

for $2 \le Re \le 800$.

Miura et al. [1977MI1] show that these correlations accurately predict the heat and mass transfer for Reynolds numbers of up to *2000*. The correlations are in good agreement with data for solid spheres, thus the effects of drop oscillation and internal circulation were minimal in the Ranz and Marshall [1952RA1] studies. FLUENT 6.2.16 employs these correlations, [1952RA1].

Yao and Schrock [1976YA1] measured the temperature of large water drops, $3 \le d_d \le 6mm$, accelerating from rest in still air, by conducting a series of experiments. The experimental data is plotted in Figure 3.1 together with results obtained by solving Equation (3.5) using different correlations for *Nu* and *Sh* found in literature.

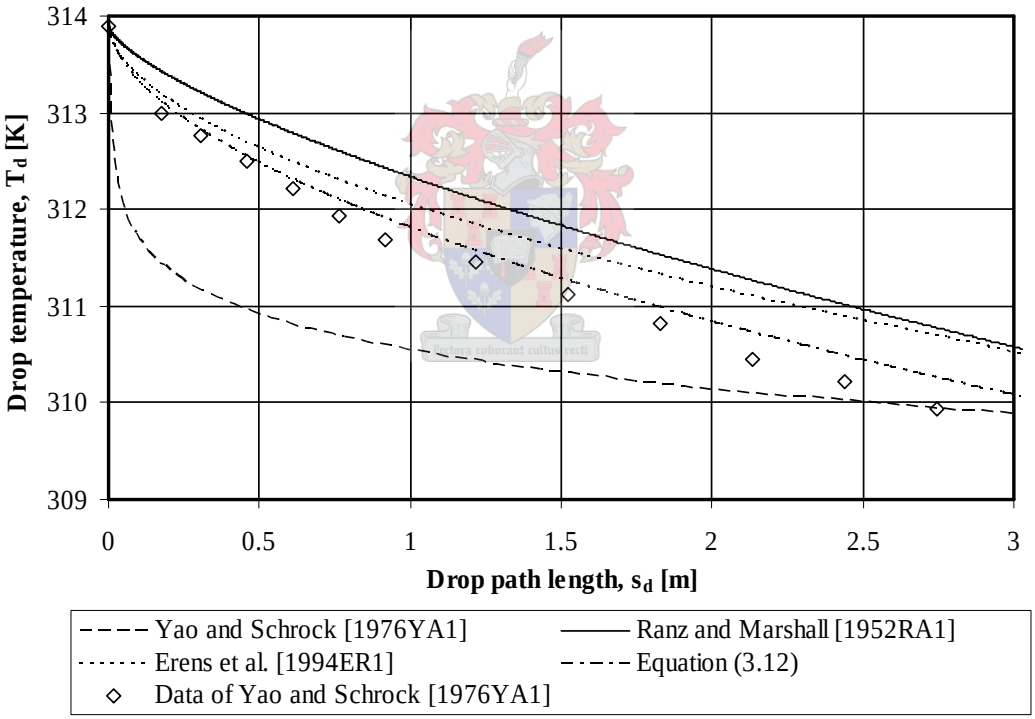

Figure 3.1: Drop temperature as a function of path length for different heat and mass transfer correlations.

Figure 3.1 illustrates that the correlations of Ranz and Marshall [1952RA1] under-predicts the cooling of accelerating water drops. Thus acceleration influences the heat and mass transfer of a drop. Snyder [1951SN1] measured the cooling rate of

single water drops accelerating freely in air. At higher Reynolds numbers his data differs by up to *15%* from the heat transfer data for solid spheres.

Yao and Schrock [1976YA1] proposed the following correlation, for their experimental data, based on the correlations given by Ranz and Marshall [1952RA1],

$$Nu = 2 + g_{YS}\left(0.6\, Re^{1/2}\, Pr^{1/3}\right) \tag{3.8}$$

where,

$$g_{YS} = 25\left(\frac{z}{d_d}\right)^{-0.7} \tag{3.9}$$

for $Re < 2500$ and $10 < (z/d_d) < 600$.

Erens et al. [1994ER1] using the data of Yao and Schrock [1976YA1] proposed a more accurate correlation, given by,

$$g_{YS} = 0.22 + 3.15\left(\frac{(dv/dt)\, d_d}{v^2 d_m}\right)^{0.2} \quad \text{for} \quad \frac{(dv/dt)\, d_d}{v^2} > 5\times 10^{-4} \tag{3.10}$$

The maximum stable drop diameter, d_m, which is the maximum diameter of a drop before it breaks up, is given by,

$$d_m = \sqrt{\frac{16\sigma_d}{g\left(\rho_d - \rho_a\right)}} \tag{3.11}$$

Using the experimental data of Yao and Schrock [1976YA1] the author proposes the following correlation,

$$g_{YS} = 0.68\left(\frac{C_D\, Re^2}{\left(C_D\, Re^2\right)_T}\right)^{-0.28} + \frac{0.95}{\left(1 + 1.4\left(\frac{C_D\, Re^2}{\left(C_D\, Re^2\right)_T}\right)^{-2}\right)} \tag{3.12}$$

where $(C_D Re^2)_T$ is at the terminal velocity condition. The full derivation of Equation (3.12) is given in Appendix D.

The predicted values for the temperature of a falling accelerating water drop using Equations (3.10) and (3.12) are illustrated in Figure 3.1, where it is seen that the latter correlated the experimental data of Yao and Schrock [1976YA1] better.

3.2 Solution Techniques

The different solution techniques that are employed to solve Equation (3.5), together with their assumptions, for the determination of the temperature and diameter of a drop free-falling through upward flowing or stagnant air are presented in this section.

3.2.1 Analytical

For the analytical solution it is assumed that the drop remains spherical for its entire path length and it falls in stagnant air. Furthermore the falling drop has no effect on the thermophysical properties of the continuous phase, thus these properties remain constant and equal to their initial conditions. For the analytical model the thermophysical properties of the drop remain constant and equal to their initial conditions.

Equations (3.1) and (3.5) are coupled and need to be solved simultaneously. In order to reduce the set of equations to a single ordinary differential equation, Equation (3.5) must be divided by Equation (3.1) to give,

$$\frac{dT_s}{dd_s} = -\frac{3}{c_v}\frac{h}{h_D}\frac{T_a - T_s}{C_s - C_a}\frac{1}{d_s} + \frac{3h_{fg}}{c_v}\frac{1}{d_s} \tag{3.13}$$

where the subscript *s* is now used to denote the spherical drop.

The final solution equation is given by,

$$RHS = \frac{1}{\xi}(\theta - 1) - \frac{\beta}{2\xi^2\alpha_1} ln\left(\frac{\xi\alpha_1\theta^2 + I_1\theta + \xi\alpha_3}{\xi\alpha_1 + I_1 + \xi\alpha_3}\right) \\ ... + \frac{\beta I_1}{\xi^2\alpha_1 I_2}\left(tan^{-1}\left(\frac{2\xi\alpha_1\theta + I_1}{I_2}\right) - tan^{-1}\left(\frac{2\xi\alpha_1 + I_1}{I_2}\right)\right) \tag{3.14}$$

$$\eta = e^{RHS} \tag{3.15}$$

where,

$$\eta = \frac{d_s}{d_{s,0}}$$

$$\theta = \frac{T_s - T_a}{T_{s,0} - T_a}$$

are the dimensionless variables for the diameter and temperature respectively, the constants in Equation (3.14) are defined below,

$$\alpha_1 = a_1\left(T_{s,0} - T_a\right)^2$$

$$\alpha_2 = \left(T_{s,0} - T_a\right)\left(2a_1 T_a + a_2\right)$$

$$\alpha_3 = a_1 T_a^2 + a_2 T_a + a_3 + A$$

$$\beta = \frac{3k_a R_v}{c_v D} Le^{-\frac{1}{3}}$$

$$\xi = \frac{3h_{fg}}{c_v\left(T_{s,0} - T_a\right)}$$

$$I_1 = \beta + \alpha_2 \xi$$

$$I_2 = \left(4\xi^2 \alpha_3 \alpha_1 - I_1^2\right)^{1/2}$$

The reader is referred to Appendix E for a full derivation of Equation (3.14).

A shortcoming of this model is its failure to relate the dependent variables temperature and diameter to an independent variable such as time or path length.

The model does show, mathematically, that the diameter of a drop changes by less than *2%* before it reaches its steady state temperature, wetbulb.

3.2.2 Numerical

For the purposes of this thesis, a numerical program was written that can solve the energy transfer equation for a free-falling drop in an incompressible Newtonian fluid, using a 4th order Runge-Kutta integration technique. The model can incorporate drop deformation, acceleration effects and change in drop diameter and neglects the effects of the drop on the continuous phase.

The thermophysical properties of the continuous phase also remain constant. Unlike the analytical solution, the thermophysical properties of the drop are able to be updated for each time step, making it more realistic.

3.2.3 Computational Fluid Dynamics

FLUENT 6.2.16 models the drops by means of a discrete phase model (DPM), utilising a Lagrangian approach in which the energy and mass transfer equations are written in a co-ordinate system that moves with each individual drop. The continuous phase equations are still expressed in their Eulerian continuum form, but are suitably modified to account for the presence of the drops, by means of interphase source terms.

The user is presented with the option to include interphase interaction. In the event that the interaction is included, then as the trajectory of a particle is computed, the code determines the heat and mass transfer between the drop phase and the continuous phase. This interaction is accounted for by appropriate interphase source terms in the continuous phase energy and species transport equations.

By default, the solution of the particle energy and mass equations are solved in a segregated manner. The user is presented with the option to enable

Coupled Heat-Mass Solution. If selected then the code will solve this pair of equations using a stiff coupled ODE solver with error tolerance control.

FLUENT 6.2.16 only utilises the Ranz and Marshall [1952RA1] correlations for determining the Nusselt and Sherwood numbers. In order to incorporate other correlations the user must compile a user-defined-function. In the code the thermophysical properties such as density, specific heat and latent heat of vaporization of the drop and the diffusion coefficient of water vapour in air remain constant and equal to their initial values defined by the user.

FLUENT 6.2.16 provides the option to solve Equations (3.1) and (3.5) by means of a number of different numerical integration techniques: implicit Euler integration; semi-implicit trapezoidal integration; analytical integration and a 5^{th} order Runge-Kutta technique.

3.3 Analysis of Results

The next section compares and discusses the results obtained by employing the different solution techniques. For the solution techniques to be comparable the simulation conditions need to be identical. For all the simulations presented here, the water drop will initially be at a higher temperature than the air.

Due to the limitations of FLUENT 6.2.16 and the analytical solution technique, the drops are assumed to be spherical, free-falling in a stagnant air with the heat and mass transfer calculated using the correlations of Ranz and Marshall [1952RA1].

The results of the three solution techniques are compared by making use of the dimensionless variables, η and θ, from the analytical solution. The simulation conditions are: drybulb air temperature of *296.6K*, initial drop temperature of *313.9K*, relative humidity of *0.6* and ambient pressure of *101325N/m*^{2}.

Numerical (1) in Figure 3.2 is for the case where the thermophysical properties of the drop are updated for each time step in the numerical solution technique, *Numerical (2)* is for the case where the thermophysical properties are held constant. *Numerical (1)* is a better representation of the reality.

For the positive θ case both the heat and mass transfer processes are in the same direction, whereas for the negative θ case the heat transfer process reverses and now tries to heat the drop, this results in an increase in the curvature of the graph. When $\theta = 0$ the drop temperature is equal to the air drybulb temperature. The figure also shows that the drop's diameter reduces by less than *2%* before the drop temperature converges to the wetbulb temperature of the air. For most conventional cooling towers the fall height and drop distribution is such that the majority of the drops never reach the wetbulb temperature, therefore the change in diameter can be considered negligible for cooling tower analysis. The change in diameter can be used to determine the mass of water evaporated.

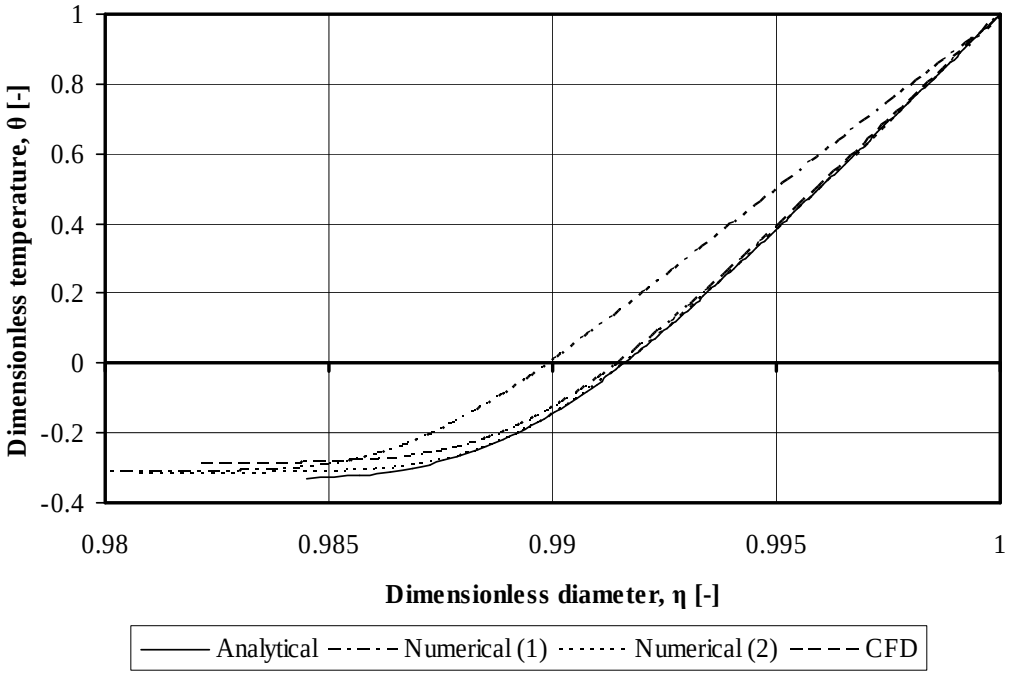

Figure 3.2: Comparison of dimensionless temperature as a function of dimensionless diameter for the three different solution techniques.

From Figure 3.2 it appears that neither the analytical nor the CFD solution represent the reality, *Numerical (1)*, accurately. Figure 3.3 compares the CFD solution, the case of constant thermophysical properties, with the *Numerical (1)* solution.

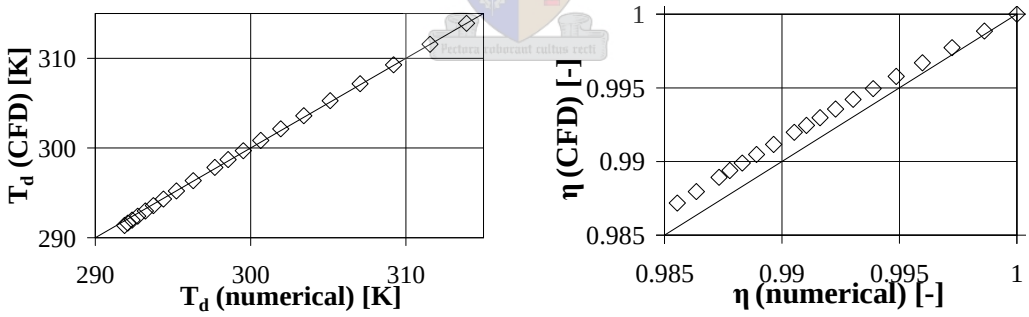

(a) (b)

Figure 3.3: Comparison between numerical and CFD results for (a) Temperature and (b) dimensionless diameter.

Figure 3.3 demonstrates that the maximum deviation between the CFD and numerical solutions is *0.15%* for both temperature and diameter. In conclusion, for the simulations presented here, CFD and any solution procedure that assumes constant thermophysical properties of the drop and utilises the

complete mixing model can be used to accurately predict the change in temperature and diameter of a water drop free-falling in stagnant air.

According to Kröger [1998KR1] the rain zone generally consists of *3-6mm* drops. Plotting the temperature as a function of time for drop diameters of *1, 2, 3, 4* and *5mm* falling in air with a counterflow velocity of *2m/s*, reveals that all of the drops will eventually converge to the wetbulb temperature of the air.

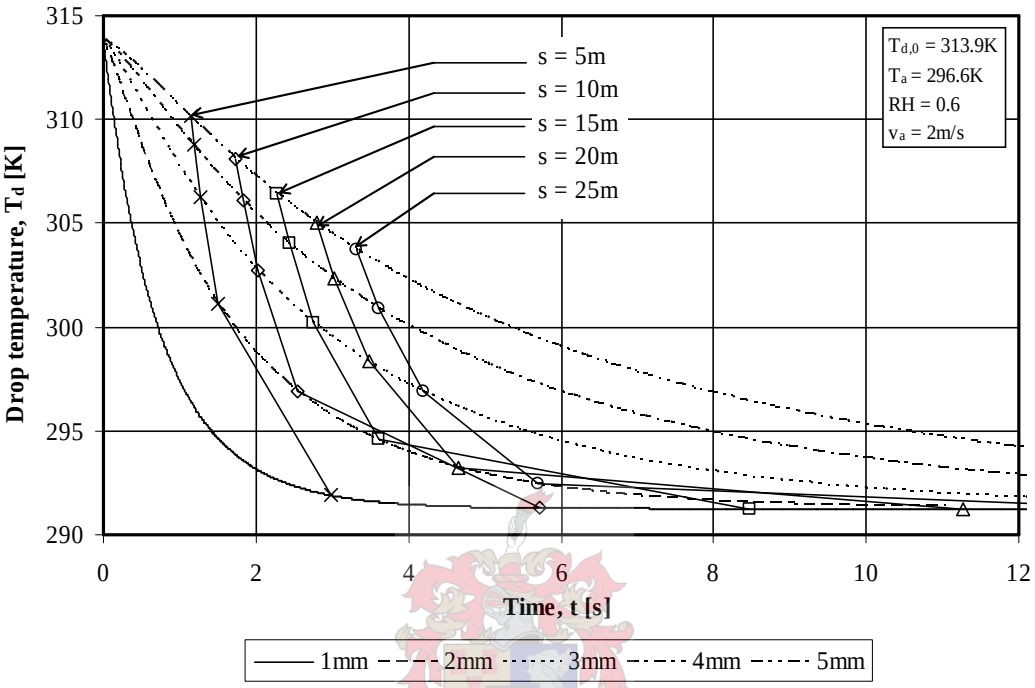

Figure 3.4: Temperature as a function of time for spherical water drops falling in counterflow air.

Similar to the drop velocity, there exists a transient and steady state stage, the steady state stage for each drop being the state where the drop attains the wetbulb air temperature.

Figure 3.4 illustrates lines of constant path length (*s*) and that smaller drops cool down quicker than larger drops. For the case of *s = 10m*, which is the typical height of a rain zone in a natural draft wet-cooling tower, the *1mm* drop has come to within *0.2%* of the steady state temperature. Kröger [1998KR1] states that generally the smallest average drop diameter in the rain zone is *3mm*. For this diameter with *s = 10m*, the change in drop temperature is only *50%* of the maximum change in drop temperature. Had the drop been *1mm* or *2mm* then the change in drop temperature would be *99.8%* or *75%* of the maximum respectively. Thus it would be desirable to have smaller drops in the rain zone.

For a rain zone height larger than *10m*, it would be undesirable to have *1mm* drop diameters, as the drop would no longer cool but only lose mass due to evaporation. Figure 3.4 shows that the majority of drops in a general rain zone of a cooling tower hardly ever reach their thermal steady state condition.

For a *1mm* drop, under the same simulation conditions as Figure 3.4, free-falling in different counterflow air velocities, the change in the drop temperature as a function of drop path length is given by Figure 3.5 below.

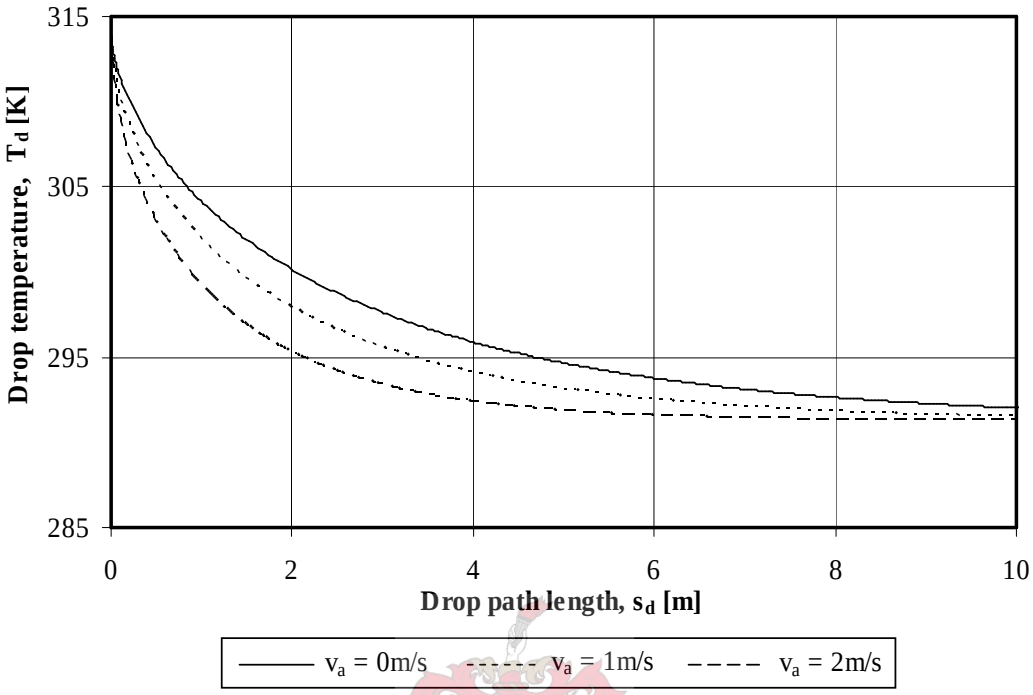

Figure 3.5: Drop temperature as a function of drop path length for various counterflow air velocities.

The figure illustrates that a counterflow air velocity increases the rate of change in the drop temperature, and that an increase in the counterflow air velocity results in an increase in the rate of change in the drop temperature. Reasons for this are the increased residence time and higher initial Reynolds numbers that relate to higher Nusselt and Sherwood numbers.

It should be noted that the effect of drop deformation on the change in temperature of a drop is addressed in Chapter 5.

Summary

A new correlation for the heat and mass transfer is proposed that predicts the temperature change of free-falling accelerating water drops with greater accuracy than others found in literature. The correlation of Ranz and Marshall [1952RA1] is however used for this thesis due to its inclusion in FLUENT 6.2.16.

The temperature and diameter change of free-falling spheres was found to be accurately predicted by FLUENT 6.2.16, analytical and numerical solution techniques.

The thermal transient time of a drop is of great importance to rain zone analysis. This conclusion is supported by the fact that the smallest average drop

diameter generally found in a cooling tower rain zone barely reaches thermal steady state.

It was found that smaller drops require less time than larger drops, for the same amount of cooling, resulting in a shorter path length. This leads to the ratiocination that the smaller the drops the shorter the rain zone required.

In conclusion it was found that a counterflow air velocity increases the rate of change in the drop temperature, and that an increase in the counterflow air velocity results in an increase in the rate of change in the drop temperature, the reasons being increased residence time and Nusselt and Sherwood numbers.

CHAPTER

4

Experimental Data Acquisition

Experimental work of a one-dimensional counterflow case is performed in order to obtain pressure drop and drop size distribution data necessary to validate CFD models. This chapter is used to discuss the experimental test facility and the setup thereof. The experimental procedure used to determine the pressure drop over the domain of drops as well as the acquisition of drop distribution data is presented here. The relevant data for the pressure drop and drop distribution is then analysed and presented at the end of this chapter.

4.1 Experimental Setup

The experimental setup that is used to determine the pressure drop over the domain as well as the drop size distribution in the domain will be discussed in this section.

As part of this thesis a test facility was designed and implemented at the Mechanical Engineering Department of the University of Stellenbosch. The calibration of the test facility is dealt with in Viljoen [2006VI1]. The test facility is capable of maximum air and water velocities in the order of $5.8kg/m^2s$. Figure 4.1 shows all the components of the experimental setup and their relation to one another.

The test facility was designed with the idea of making it adaptable, thus entailing that the same parts can be used to construct either a crossflow, counterflow or cross-counterflow test domain.

Referring to the figure, the path that the air travels is now given. The test facility in the counterflow arrangement is an induced draft tunnel. The axial fan creates a low pressure on the diffuser side of the fan, the atmospheric air being at a higher pressure on the outside of the test facility is then drawn in due to the pressure difference. The air passes through the rounded inlet that creates a uniform velocity profile in the test section and then proceeds to move through the domain of drops. The air then moves through the fill and the water distribution sections before reaching the drift eliminator section where the majority of the entrained drops are removed. After leaving this section the air enters the plenum chamber, from where it travels through a flow nozzle. The pressure difference over the flow nozzle is measured and this is used to determine the mass flow of the air. The diffuser aids in pressure recovery and also helps to improve fan performance. The air then finally is discharged by the fan to the surroundings. The

static pressure difference of the air over the test section is measured between pressure tapping points *1* and *2*.

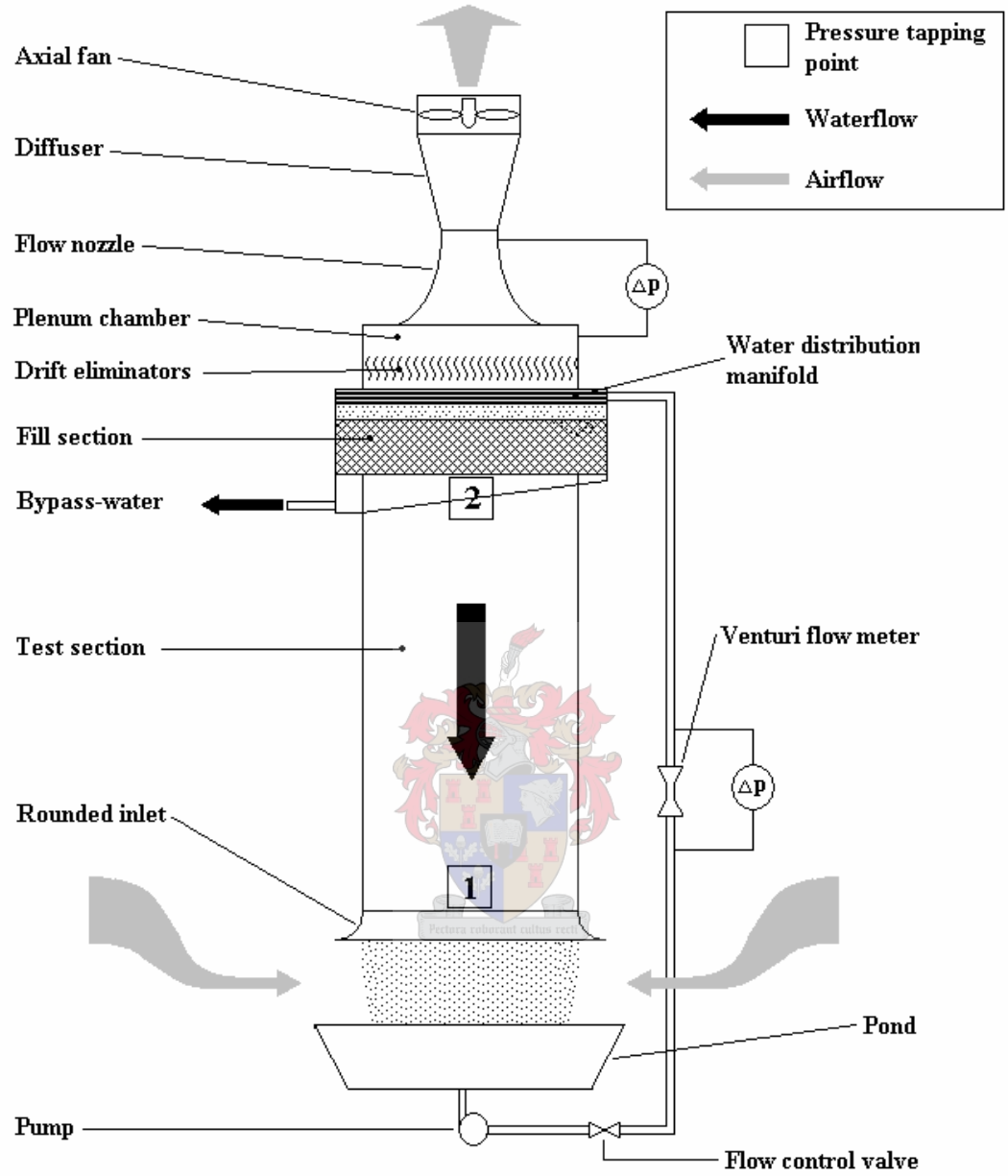

Figure 4.1: Experimental test setup in counterflow configuration.

The water is pumped from the pond through a control valve that is located on the high pressure side of the pump to control the volume flow of the water. The water passes through a venturi meter where the pressure difference over the venturi meter is recorded and used to determine the total volume flow of water that enters the tunnel. The water is introduced to the tunnel *via* a water distribution manifold found in the water distribution section. It then enters the fill section of the tunnel and passes through it. From here the central portion of the

flow leaving the fill passes through the test section where it interacts with the air before returning to the pond. The peripheral portion is however collected in bypass troughs from which it drains to a collecting tank for flow measurement before returning back to the pond.

4.2 Measurement Techniques and Instrumentation

Temperature measurements are made using type *T* thermocouple wire and the atmospheric pressure is measured with a mercury column manometer.

The pressure difference over the venturi flow meter is measured with a *Foxboro 843DP-H2I* pressure transducer coupled to a data logging program, *LabView 7.1*, *via* a *Hewlett Packard A34790* data logger. The calibration curve for the venturi flow meter is given by,

$$Q_w = 1.73\times10^{-7}\,\Delta p_w^5 - 2.915\times10^{-5}\,\Delta p_w^4 + 1.819\times10^{-3}\,\Delta p_w^3 - 5.363\times10^{-2}\,\Delta p_w^2 + 0.9511\Delta p_w + 0.4887 \tag{4.1}$$

where Q_w is the water flow rate in ℓ/s and Δp_w is the pressure drop over the venturi meter in kN/m^2. The pressure drop is determined using the calibration curve of the pressure transducer, given by,

$$p_w = 15.996V_w - 16.006 \tag{4.2}$$

where V_w is the voltage reading given by the pressure transducer in volts.

The pressure drop over the flow nozzle as well as over the test section was measured with *Betz* water micromanometers. Frequency control of the fan is done by a *YASKAWA General Purpose Inverter* (*Varispeed E-7 Model CIMR-E7C*), so as to control the mass flow of air through the test facility. The velocity of the air in the test section is determined by,

$$v_{ts} = C_n\left(\frac{2\Delta p_n}{\rho_a \kappa}\right)^{0.5}\frac{A_n}{A_{ts}} \tag{4.3}$$

where Δp_n is the pressure drop over the nozzle, C_n is a calibration correction coefficient of the nozzle with a value of *0.96*, κ is the *velocity-of-approach factor* with a value of 0.988 and A_n and A_{ts} are the areas of the nozzle and test sections respectively.

The drop size distribution in the test section is measured with an apparatus designed and implemented by Terblanche [2005TE1], a schematic of the installation of this apparatus in the test facility at station *2* is given below.

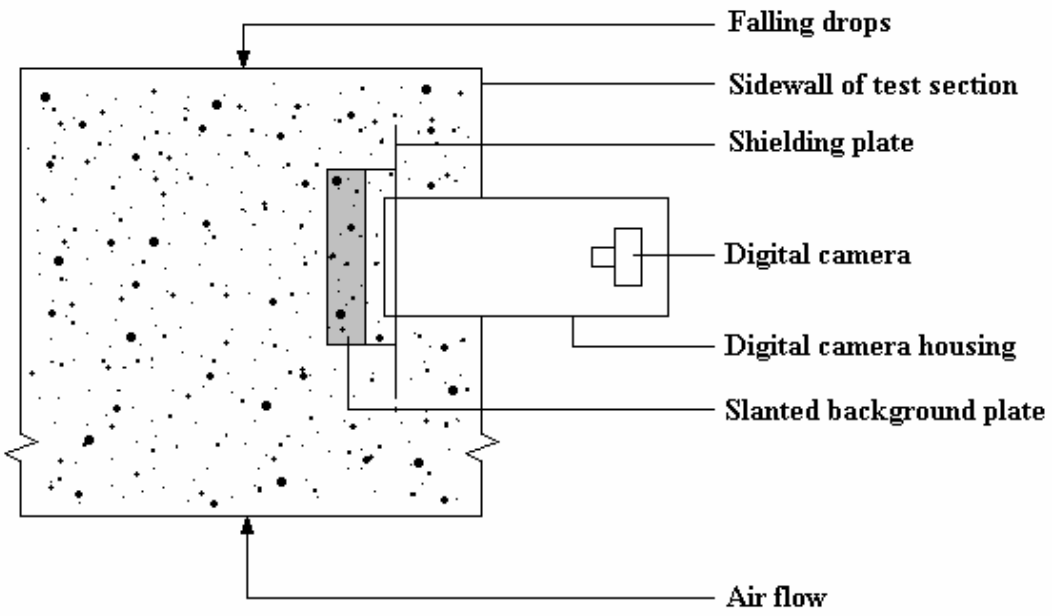

Figure 4.2: Drop size distribution measurement apparatus.

The raw experimental data is in the form of digital images. The digital images are first imported into a standard image editing program in order to draw definite lines around each drop so that they can easily be distinguished. Once this is complete the edited digital images are imported into *Droplet Analyzer v.1* developed by Terblanche [2005TE1].

Droplet Analyzer v.1 determines the coordinates of each drop as well as the number of pixels that each drop consists of. This data is then manipulated to determine the drop distribution, the manipulation procedure is given below. The close, far and average calibration values are determined using the following set of equations respectively,

$$\begin{aligned} y_c &= 0.25 \ \ mm/pixel \\ y_f &= -0.000075x + 0.313 \ \ mm/pixel \\ y_{avg} &= \frac{y_c + y_f}{2} \ \ mm/pixel \end{aligned} \tag{4.4}$$

where x is the horizontal coordinate of the drop in the photograph. The background plate, as shown in Figure 4.2, is not perpendicular to the digital camera but at an angle, so as to reduce glare coming from the digital camera flash. This angle results in the fact that pixels will have different dimensions at different positions in the digital image, thus the need for the two calibration values in Equation (4.4).

4.3 Experimental Procedure

The test procedure for both the acquisition of the pressure drop and drop distribution data is documented here in the format of the steps that were taken to conduct one complete test.

4.3.1 Pressure Drop

1 Record the atmospheric pressure using the mercury column manometer.
2 Reset the *Betz* micromanometers for both the test section and the nozzle to the zero position.
3 Run the test facility by turning the pump on, it is not necessary at this point to turn the fan on, until the water temperature reaches the wetbulb temperature of the air in the test section that is measured at both station *1* and *2*. Once this condition is reached the fan can be turned on.
4 Input the atmospheric pressure, measured in step *1*, into the graphic-user-interface (GUI) of the *LabView* program specifically written for the test facility, see Snyman [2005SN1]. The program uses this value together with the temperature measured in the nozzle to determine the air density using the ideal gas law.
5 Set the water to the desired total volume flow by adjusting the control valve, the total volume flow is indicated in the GUI.
6 Adjust the frequency of the fan until the desired velocity in the test section is achieved, this is determined by using the pressure drop over the flow nozzle.
7 Once the *Betz* micromanometer for the test section has stabilized the pressure drop reading can be recorded.
8 For one fixed water flow rate, three different air velocities are tested.
9 Repeat steps *6* through *9* for six different water flow rates.

4.3.2 Drop Size Distribution

1 Follow steps *1* through *7* as in section 4.3.1.
2 It is important to note that the water total flow rate and the air velocity in the test section be set to the same values as in section 4.3.1.
3 Once the water flow rate and the air velocity have stabilized the digital images of the drop distribution can be taken. It was found that five digital images at a single test condition were sufficient.
4 For one fixed water flow rate take digital images at the same three air velocities as in section 4.3.1.
5 Repeat steps 4 and 5 for the six different water flow rates.

4.4 Experimental Data Analysis

The following section is used to illustrate the analysis procedure and the equations used to convert the raw experimental data into the relevant data that will be used in this thesis. The rain zone loss coefficient for comparison purposes and the drop distributions will serve as input data for the CFD simulations.

4.4.1 Rain Zone Loss Coefficient

The loss coefficient for the rain zone in the test section can be determined using the total pressure drop, Δp_{ts}, over the test section and the velocity, v_{ts}, in the test section as shown in the equation below.

$$K_{rz} = \frac{\Delta p_{ts}}{1/2 \rho_a v_{ts}^2} \tag{4.5}$$

4.4.2 Drop Size Distribution

The diameter of each drop can be determined using the *number of pixels* for the drop, the diameter is given as a spherical equivalent diameter,

$$d_e = \left(\frac{4 y_{avg}^2 \left(number\ of\ pixels \right)}{\pi} \right)^{0.5} \tag{4.6}$$

where d_e is in *mm*. This is done for each drop in the digital image. Once the diameters are known the drops can be grouped into intervals defined by diameter. The mass for each diameter interval can be determined by multiplying the number of drops in the interval by the representative mass for the interval. The representative mass is determined using the midpoint diameter of the interval. The total mass can then be determined by summing all the interval masses, by using:

$$\begin{aligned} M_i &= \frac{\pi \rho_d}{6} \sum_{j=1}^{N_{d,i}} d_{e,j}^3 \\ M_t &= \sum_{i=1}^{N} M_i \end{aligned} \tag{4.7}$$

where $N_{d,i}$ and N are the number of drops in an diameter interval and the number of diameter intervals respectively. The mass fraction for each interval is then determined by dividing each interval mass by the total mass.

$$M_{f,i} = \frac{M_i}{M_t} \tag{4.8}$$

The experimental retained mass fraction, $Y_{d,i}$, of drops with a diameter greater than d_i is determined as follows,

$$Y_{d,i} = 1 - \sum_{1}^{i} M_{f,i} \tag{4.9}$$

The Rosin-Rammler equation is used to fit a curve through the experimental data points. The Rosin-Rammler equation is given by,

$$Y_d = exp\left(-\left(\frac{d}{d_{RR}}\right)^n\right) \tag{4.10}$$

where Y_d is the retained mass fraction of drops with a diameter greater than d, d is the drop diameter, d_{RR} is the mean drop diameter and n is a measure of the spread of drops. The value of d_{RR} is obtained by noting that this is the value of d at which $Y_d = e^{-1} \approx 0.368$. The value of n is determined using the experimental values for Y_d and the corresponding d as well as d_{RR},

$$n = \frac{\sum_{i=1}^{N} \frac{ln\left(-ln\left(Y_{d,i}\right)\right)}{ln\left(d_i/d_{RR}\right)}}{N} \tag{4.11}$$

Representative diameters of a polydisperse drop distribution can be determined from ASTM E799-92 which defines these representative diameters as follows:

$$d_{pq}^{(p-q)} = \frac{\sum_i d_i^p}{\sum_i d_i^q} \tag{4.12}$$

These diameters are single values that express the various mean sizes in the domain of polydisperse drops. Table 4.1 below presents a summary of the common representative diameters.

Table 4.1: Summary of representative diameters for polydisperse drop distributions.

p	q	Name
1	0	Average diameter
3	0	Mean volume diameter
3	2	Sauter mean diameter
4	1	Pierce diameter
4	3	De Brouckere diameter

4.5 Experimental Results

The experimental results for the rain zone loss coefficient and the drop distribution are given in the relevant sections below. The reader is referred to Appendix F for the rest of the experimental data. Appendix G is used to perform a sample calculation for the test condition of G_a = *2.43 kg/m^{2}s* and G_w = *2.57 kg/m^{2}s*.

4.5.1 Rain Zone Loss Coefficient

Figure 4.3 is a chart of the experimental rain zone loss coefficient as a function of the water mass velocity, G_w, for different air mass velocities, G_a.

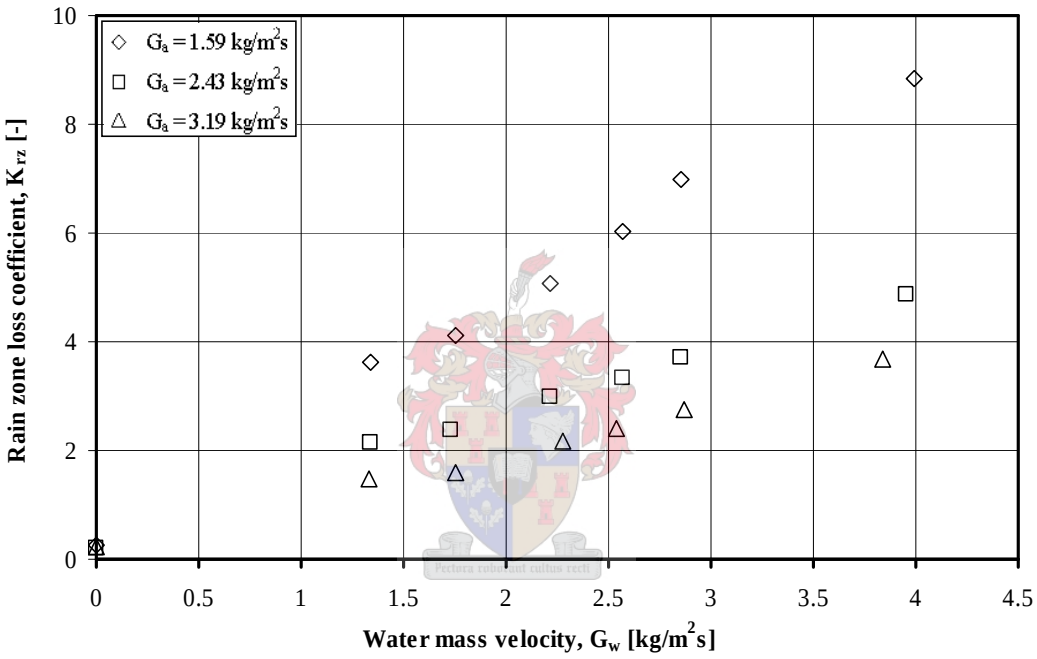

Figure 4.3: Experimental rain zone loss coefficient.

4.5.2 Drop Size Distribution

An example of the experimental drop size distribution is given below. This polydisperse drop distribution is used in simulations in subsequent chapters.

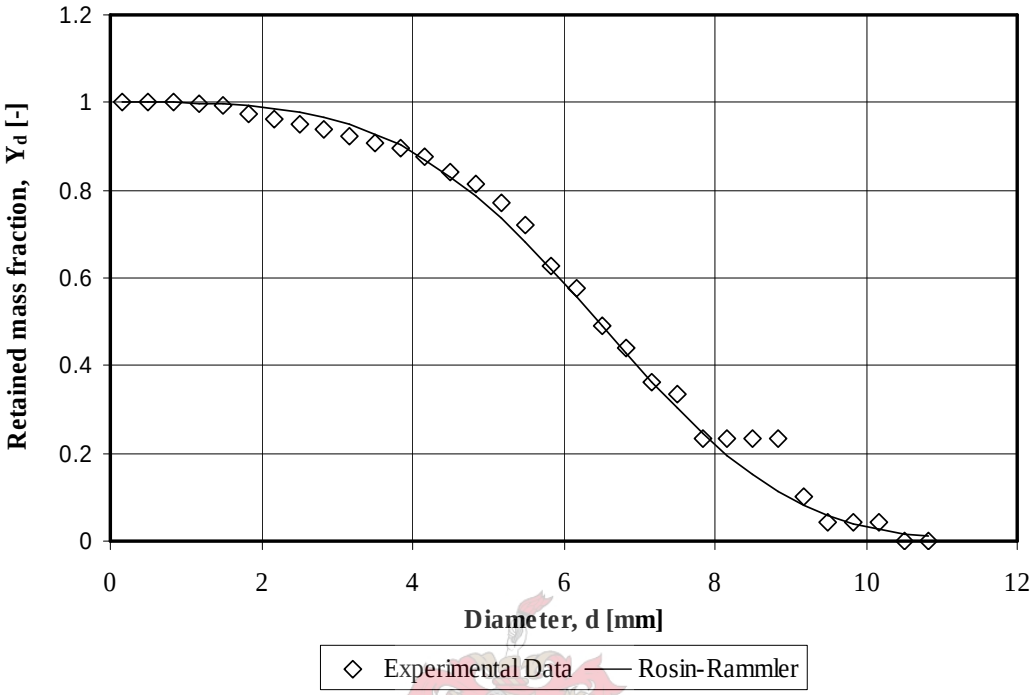

Figure 4.4: Retained mass fraction for experimental data and Rosin-Rammler distribution function.

Appendix H gives a full analysis of the Rosin-Rammler distribution function. The analysis results in the exclusion of the Rosin-Rammler distribution function as a method of inputting drop distribution data into FLUENT 6.2.16.

The values of the representative diameters, from Equation (4.12), are given in Table 4.2.

Table 4.2: Representative diameters.

Name	*p*	*q*	Diameter [mm]
Mean Diameter	1	0	3.219
Mean volume diameter	3	0	4.354
Sauter mean diameter	3	2	5.734
Pierce diameter	4	1	5.553
De Brouckere diameter	4	3	6.678

A plot of three of the representative diameters for all the test conditions is given below, the three representative diameters are: Sauter mean diameter, Mean volume diameter and the Average diameter.

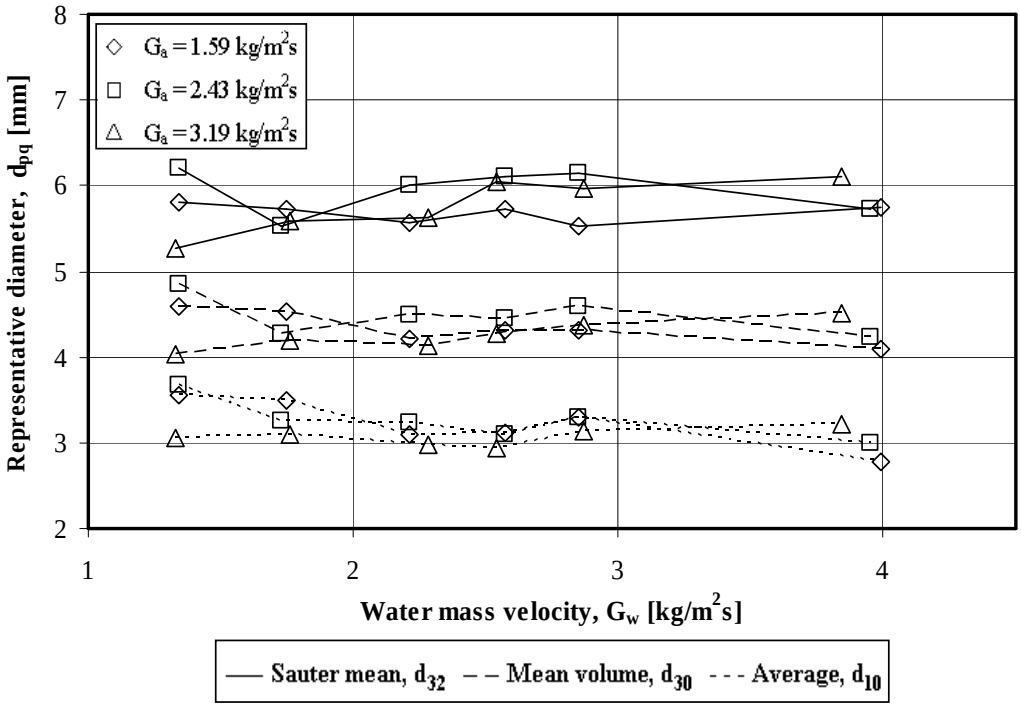

Figure 4.5: Consistency of the representative diameters for different test conditions.

The curves show that the representative diameters remain relatively constant. The *Sauter mean* diameter does seem to show the greatest variation for a specific water mass velocity condition with the *Average* diameter showing the least.

Summary

This chapter dealt with the experimental setup as well as the procedure and analysis followed to determine the rain zone loss coefficient as well as the drop distribution data. The experimental results were then given and discussed. Interestingly it was found that the representative diameters stayed relatively constant for the range of test conditions.

CHAPTER

5

Effect of Drop Deformation on Rain Zone Performance

Chapter 2 shows that drop deformation has an effect of decreasing the absolute terminal velocity. De Villiers & Kröger [1998DE1] include the drop deformation in their determination of the rain zone loss coefficient and seem to show good comparison with experimental results. Fisenko et al. [2004FI1] exclude drop deformation in the development of their mathematical model of mechanical draft cooling tower performance. They do not determine the pressure drop over the rain zone with their model and confine themselves to modelling the change in the drops' velocity, diameter and temperature, and also a change in the temperature and density of the air-vapour mixture in a cooling tower. Their model however, correlates well with experimental data. Thus two separate researchers have shown that for the one case drop deformation plays a role and then for the other case it does not. This chapter is used to validate both researchers' work.

This chapter is used to gain an understanding of the effect of drop deformation on rain zone performance. To this end, the effect of drop deformation on the pressure drop over a rain zone is validated using CFD and experimental data determined in Chapter 4. The effect on the change in temperature of the water passing through the rain zone is also validated using CFD.

5.1 Rain Zone Pressure Drop

Consider a single drop falling through air moving at an absolute speed of v_a.

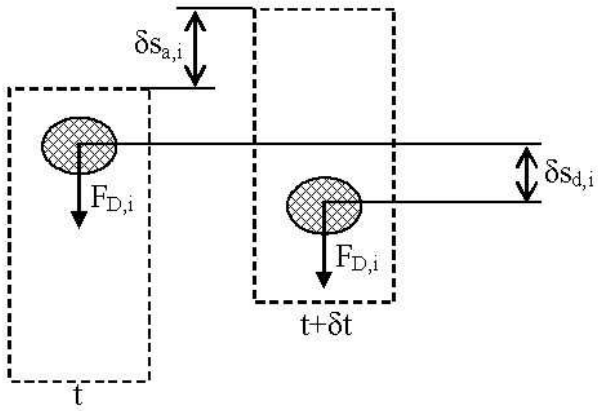

Figure 5.1: Incremental control system for determination of pressure drop.

The scientific definition of work is given as: work is the measure of a quantity that is capable of accomplishing macroscopic motion of a system due to the action of a force over a distance. Now for a variable force the expression for work becomes,

$$work = \int_{s_0}^{s_f} F(s)\cos(\theta)ds \tag{5.1}$$

where F is the force that is dependent on the displacement s and θ is the angle between the force and the direction of motion. For the case in Figure 5.1, the motion of the drop and the parcel of air are in parallel and opposite directions, thus negative work is done on the parcel of air, resulting in a pressure drop.

If a parcel of air surrounding a drop, as shown in Figure 5.1, moves at a velocity of v_a, then the parcel will be displaced a distance of $\delta s_{a,i}$ during a time increment of δt. The work done by the drag force component is therefore:

$$work = -F_{D,i}\delta s_{a,i} \tag{5.2}$$

Applying the same methodology to each drop-parcel in the domain, an expression for the pressure drop over the domain can be determined,

$$\Delta pQ_a = \frac{\sum_{i=1}^{N_d} -F_{D,i}\delta s_{a,i}}{\delta t} \tag{5.3}$$

where N_d is the number of drops in the domain. Further simplification of the expression yields,

$$\Delta p = \frac{\sum_{i=1}^{N_d} -F_{D,i}v_{a,i}}{v_a A} \tag{5.4}$$

where A is the cross sectional area of the domain, v_a in the denominator is the average air velocity and $v_{a,i}$ is the velocity of the parcel derived from,

$$v_{a,i} = \frac{\delta s_{a,i}}{\delta t} \tag{5.5}$$

For the case where the drops are assumed not to effect the continuous phase, as was done in the *numerical solution technique*, the velocity of the parcel is equal to the average air velocity which leads to a further simplification,

$$\Delta p = \frac{\sum_{i=1}^{N_d} -F_{D,i}}{A} \tag{5.6}$$

Referring to Equation (5.6), the summation of the drop drag determines the pressure drop over a domain. It is important to mention that spherical and deformable drops, of equal mass, will attain the same terminal drag force. Equation (5.6) shows that pressure drop changes only if the sum of the drag forces changes. The two influential factors are the number of drops and the drag force values of the drops in the domain. Deformable drops larger than approximately *3mm*, have lower absolute terminal velocities than their equivalent spherical drops. This means that their residence time in a particular domain will be longer than that of the spherical drops, resulting in a greater number of drops in the domain and subsequently a higher pressure drop. Deformable drops attain their terminal condition sooner than spherical drops, resulting in higher drag force values for a specific domain and subsequently a higher pressure drop.

5.1.1 Analysis

The pressure drop tests conducted in the test facility described in Chapter 4 were simulated using FLUENT 6.2.16 to investigate the effect of drop deformation on pressure drop. The measured drop size distribution data, air and water flow rates and temperatures are used as input values. The simulations were done for polydisperse and some of the different monodisperse drop distributions to compare results. The CFD rain zone loss coefficients based on a Sauter mean, mean volume and average diameter and the corresponding experimental data are plotted against the CFD loss coefficients for the polydisperse drop distributions in Figure 5.2.

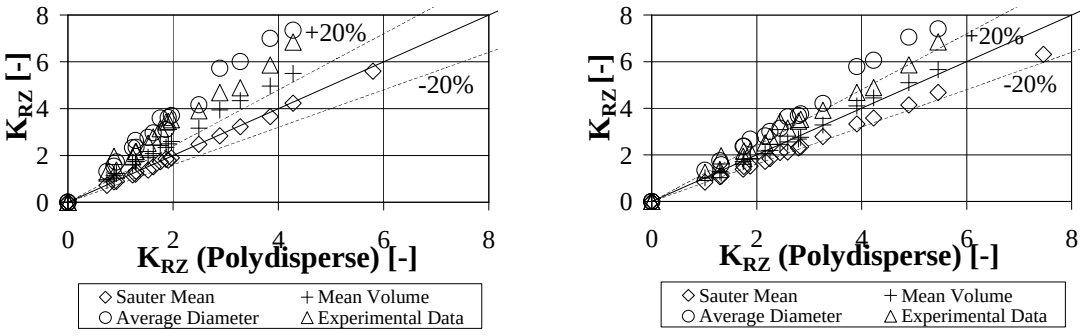

(a) Spherical drops (b) Deformable drops

Figure 5.2: Experimental and monodisperse CFD results for the rain zone loss coefficient plotted against polydisperse CFD results.

The numerical program developed for the drop velocity, path length and heat and mass transfer calculations, is also used to determine the pressure drop over the domains using Equation (5.6). The analysis is restricted to monodisperse

drop distributions. In the figures below the numerical program's results are compared to the results of FLUENT 6.2.16.

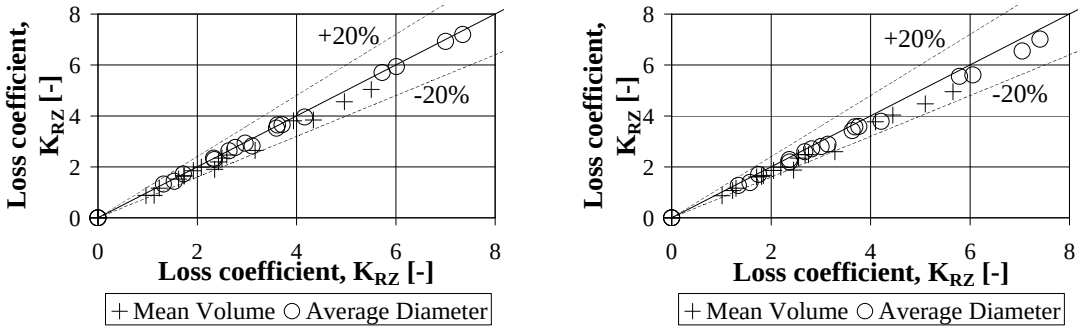

(a) Spherical drops (b) Deformable drops

Figure 5.3: Monodisperse numerical results for the rain zone loss coefficient plotted against monodisperse CFD results.

In summary, the presumption that drop deformation affects the rain zone pressure drop by increasing it is correct. The experimental results share greater correlation with the deformable drop cases and thus the drop deformation is included throughout this thesis for all simulations of the rain zone. The analysis also shows that De Villiers & Kröger [1998DE1] were correct in including drop deformation in the determination of their model for the calculation of the rain zone loss coefficient.

5.2 Water Outlet Temperature

As stated in the introduction of this chapter Fisenko et al. [2004FI1] ignore drop deformation in the determination of their mathematical model of a mechanical draft cooling tower. The effect of drop deformation on drop drag and the subsequent effect on the change in water outlet temperature of a typical cooling tower is analysed in this section. The analyses are performed using the Ranz and Marshall [1952RA1] correlations.

5.2.1 Analysis

The analysis is performed by first analysing *2, 3, 4* and *5mm* diameter drops and examining their change in temperature with respect to path length, for both the spherical and deformable drop case. The test conditions are: initial drop temperature of *295.65K*, ambient air temperature of *288.6K* with a relative humidity of *10%*, the ambient air pressure is *84100N/m*^{2} and the counterflow air velocity is *1.975m/s*. These conditions are found in Kröger [1998KR1] for a typical natural draft circular wet-cooling tower with a rain zone fall height of *10m.*

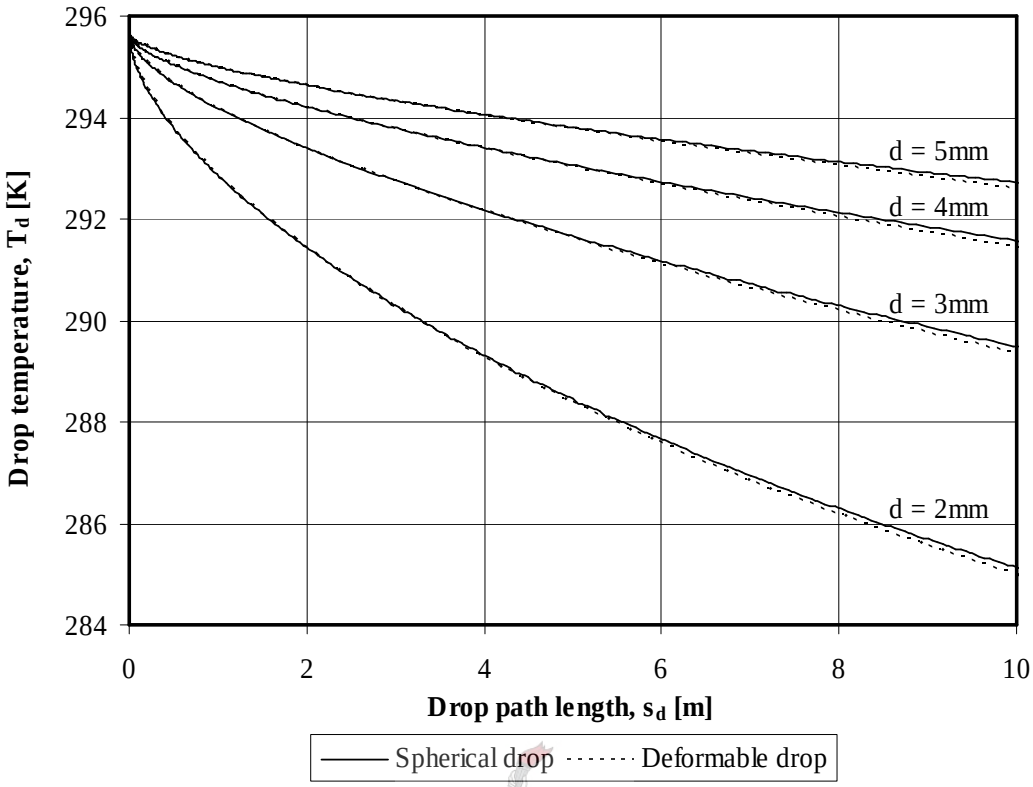

Figure 5.4: Comparison between spherical and deformable drops with respect to drop temperature.

Figure 5.4 shows that there is not much difference between the respective drops concerning the temperature as a function of fall height. At the end of the path length the deformable drop has a lower temperature, which is due to the fact that the drop is in contact with the air for longer in the specified fall domain. The two curves show the same cooling for the first part of the path length, they begin to separate at roughly *0.9m*. The reason being that before this point they both have the same velocity and thus the same Nusselt and Sherwood numbers and subsequently the same cooling rate.

For the single drop analysis there was no interaction with the continuous phase. For the analysis that follows, interaction is included. FLUENT 6.2.16 is used to analyse a counterflow domain with a height of *4m*. The same test conditions are used as in the single drop analysis. A polydisperse drop distribution was used with a total mass flow of *3.39kg/s*. The outlet water temperature is determined using a mass flow averaged scheme at the water outlet boundary, as given by Equation (5.7),

$$T_{wo} = \frac{\sum_{i=1}^{N_d} m_{d,i} T_{d,i}}{\sum_{i=1}^{N_d} m_{d,i}} \tag{5.7}$$

where N_d is the total number of drops at the outlet boundary. The results for the mass flow averaged water outlet temperature are given in Table 5.1 below.

Table 5.1: Comparison of outlet water temperature for spherical and deformable drops.

Spherical drops	Deformable drops
294.27K	294.26K

This analysis too shows that the deformable drops exhibit a lower temperature. However, the difference between the models is of such a small value, *0.7%* of the total cooling, that it can be stated that drop deformation has a negligible effect on the cooling of the drops and subsequently the water outlet temperature. Therefore Fisenko et al. [2004FI1] are able to ignore drop deformation in their mathematical model without incurring a significant error in the determination of the outlet water temperature.

Summary

It is seen that drop deformation does affect the determination of the rain zone loss coefficient as well as the outlet water temperature of a rain zone. For the case of the rain zone loss coefficient the effect is of a measurable order however the effect on the water outlet temperature is negligible. Including drop deformation in a mathematical model may present some difficulties, however if a single mathematical model is to be created that both describes the rain zone loss coefficient as well as the water outlet temperature then drop deformation must be included so as to model accurately.

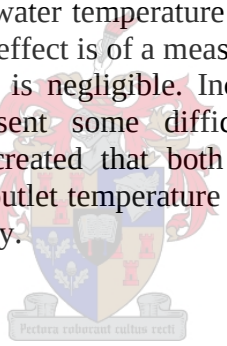

CHAPTER

6

CFD Model of the Rain Zone

In subsequent chapters, investigation is lodged into the feasibility of modelling the loss coefficient and Merkel number of polydisperse drop distributions by assuming a suitable monodisperse drop distribution using a representative diameter. All these investigations are done using the commercial CFD code, FLUENT 6.2.16. The objective of this chapter is to develop a CFD model. For the counterflow rain zone a three-dimensional mesh is generated and for the natural draught circular wet-cooling tower rain zone a two-dimensional axisymmetric mesh is generated. The results of the simulations for the polydisperse drop distributions are presented.

6.1 Background

Both the Merkel [1925ME1] and Poppe [1972PO1] methods are one-dimensional analytical cooling tower models. Merkel makes a number of simplifying assumptions to the heat balance equation, reducing the driving potential for heat and mass transfer to an enthalpy difference. Poppe includes the effect of evaporation of water and proposes a more comprehensive set of equations. Both models have proven to be acceptable, but neither can capture nor predict the non-uniformities that exist in a cooling tower. CFD models, due to their finite volume approach, have the capability to predict non-uniformities that exist in a cooling tower if modelled correctly.

FLUENT 6.2.16 is able to model polydisperse and monodisperse drop distributions and can also employ various turbulence models, thus a realistic flow field can be generated. The code models the drops by means of a discrete phase model (DPM), utilizing a Lagrangian approach in which the conservation of momentum equation is written in a co-ordinate system that moves with each individually modelled drop. The continuous phase equations are expressed in their Eulerian continuum form, but are suitably modified to take account of the presence of the drop phase.

6.2 CFD Solver Models

Considering the importance of natural draught circular wet-cooling towers in the power generation field, it was decided to simulate such a geometry. Furthermore,

due to the nature of the experimental work done, a counterflow domain is simulated.

To analyse the heat, mass and momentum transfer in the rain zone of a wet-cooling tower, certain simplifying assumption need to be made. For the continuous phase:

- The mean flow field is steady thus all time derivatives are zero.
- The flow is incompressible.
- The flow is Newtonian and turbulent.
- The flow field at the tower inlet is essentially two-dimensional, thus implying axisymmetric flow for a circular tower. For the counterflow geometry the flow is essentially one-dimensional.

FLUENT 6.2.16 has thus been used to solve the steady Reynolds Averaged Navier-Stokes (RANS) equations closed employing the standard k-ε turbulence model. The semi-implicit method for pressure linked equations (SIMPLE) was employed with second order upwind discretization employed for the spatial derivatives. A segregated implicit solver was used.

For the DPM the following assumptions are made:

- No drop agglomeration, collision, coalescence or break-up occurs.
- The drops do not influence the continuous phase turbulence conservation equations.

Drop deformation is included in the CFD model by incorporating a UDF that employs the correlation, Equation (2.16), derived in Appendix B.

Solution of the discrete phase implies integration in time of the force balance on the drop to yield the drop trajectory. As a drop moves through the continuous phase it experiences drag due to the viscous nature of the continuous phase. The conservation of momentum states that this force, acting to change the momentum of the drop, also changes the momentum of the continuous phase. As the drop is moved along its trajectory, heat and mass transfer between the drop and the continuous phase are also computed *via* the heat and mass transfer laws. The aforementioned interactions of momentum, heat and mass transfer are accounted for by appropriate interphase source terms in the continuous phase momentum, energy and species equations respectively.

The rain zone of a cooling tower contains a large number of drops. In order to individually model each drop it is necessary to treat the drop in an unsteady fashion. Although this is possible it does increase the demand on the computation time. Steady modelling presents the same results for the pressure drop, change in drop and air temperature and change in the vapour content of the air, in a fraction of the time required for unsteady modelling. This together with the number of simulations needed for the purpose of this thesis make steady modelling of the drops the viable option.

For steady modelling, only a sample of the total population is analysed, each sample is tracked from injection to termination (escape or complete evaporation) and an appropriate portion of the total mass flow rate of water is then assigned to each of the trajectories. If drop agglomeration, collision, coalescence or break-up need to be modelled then the drops would have to be treated in an unsteady fashion.

As stated earlier for the purposes of these simulations, the standard *k-ε* turbulence model is employed. The model combines turbulent Reynolds number forms of the *k* and *ε* equations for the free stream with algebraic "*law of the wall*" representation of the flow within the boundary layer. It should be emphasized that existing turbulence models are inexact representations of the physical phenomena involved. The nature of the flow to which the turbulence model is being applied is a leading factor in the degree of accuracy that is attainable. Recirculating flow at the cooling tower inlet gives rise to numerical inaccuracies, it is for this reason that comparison need be drawn with experimental correlations in order to gain confidence in the results presented. It is recommended that accuracy assessment be performed on the available and viable turbulence models.

6.3 CFD Setup and Input Data

This section will give a brief synopsis of the geometries, boundary conditions, input data and considerations used to construct the numerical wet-cooling tower simulations of this thesis, using the mesh generation code GAMBIT 2.2.30 and the CFD code FLUENT 6.2.16.

6.3.1 Tower Geometry and Boundary Conditions

The counterflow domain together with the boundary conditions is given in Figure 6.1. The dimensions of the domain are *1.5×1.5×4m* for the width, depth and height respectively.

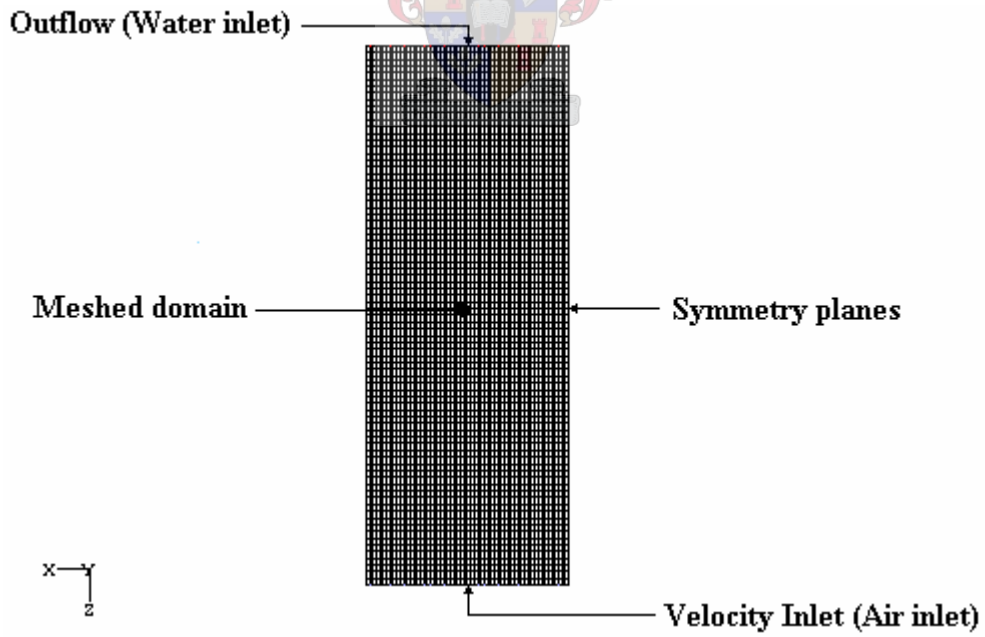

Figure 6.1: Counterflow domain and boundary conditions.

Grid independence was investigated on the counterflow domain. The results that were monitored are the pressure drop across the domain, the outlet water temperature and the mass fraction of water vapour at the air outlet boundary. The reader is referred to Appendix I for a full description of the analysis. From the analysis it was found that a cell height of *50mm* gave sufficient convergence. Thus for all the simulations presented here, including those for the circular tower domain, this cell height was used for all cells found in the rain zone. For the three-dimensional counterflow domain this resulted in *288 000* hexahedral cells in the domain.

Figure 6.2 depicts the natural draught circular wet-cooling tower domain together with the boundary conditions. The geometry of the tower is taken from Kröger [1998KR1]. The computational domain is discretized with approximately *75 000* two-dimensional structured cells. The computational domain extends approximately *60m* beyond the cooling tower inlet allowing for the determination of the inlet velocity profile. The tower has a base diameter of *104.5m* and a height of *147m*. The tower has an inlet rounding $r_i/d_i \approx 0.01$, where r_i is the inlet rounding radius and d_i is the inlet diameter of the tower.

The combination of fixed *mass inlet*, *symmetry plane* and *outflow* boundaries ensure that the velocity distribution in the particular rain zone resembles reality. Unlike the mathematical model given by De Villiers and Kröger [1998DE1], the flow field is not specified at the tower inlet, but instead the flow is allowed to develop naturally and according to the constraints of the tower domain and the laws of fluid flow. The fixed *mass inlet* is used so as to ensure that the mass flow rate of air in all the simulations is the same, so as to create similitude.

It should be noted that the effect of boundary layers within large cooling towers is small, so that any inaccuracies can be assumed negligible.

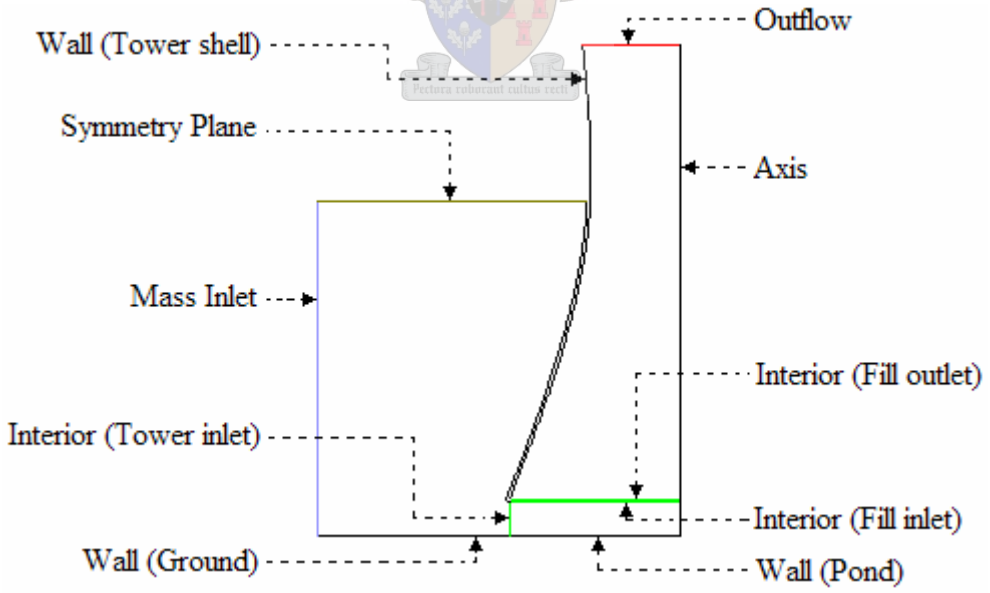

Figure 6.2: Natural draught circular wet-cooling tower domain and boundary conditions

6.3.2 CFD Input Data

For each domain, two different polydisperse drop distributions are simulated together with their representative monodisperse diameters. The two different polydisperse drop distributions chosen are:

A. A distribution with a large median diameter, this distribution was determined experimentally in Chapter 4, for film type (orthotropic) fill.
B. A distribution with a small median diameter, this distribution can be found in Kröger [1998KR1], for a trickle pack.

The distributions lie close to the extremities of the drop distribution interval found in wet-cooling towers to date as given by Kröger [1998KR1]. The necessary information for both distributions is given below in Tables 6.1 and 6.2.

Table 6.1: Polydisperse drop distribution data for distributions *A* and *B*.

Distribution *A*		Distribution *B*	
Diameter interval [mm]	Number of drops [-]	Diameter interval [mm]	Number of drops [-]
0.667 – 1	1	0 – 0.5	43
1 – 1.333	16	0.5 – 1	205
1.333 – 1.667	40	1 – 1.5	165
1.667 – 2	84	1.5 – 2	78
2 – 2.333	43	2 – 2.5	23
2.333 – 2.667	22	2.5 – 3	10
2.667 – 3	15	3 – 3.5	5
3 – 3.333	14	3.5 – 4	4
3.333 – 3.667	10	4 – 4.5	3
3.667 – 4	7	4.5 – 5	4
4 – 4.333	7	5 – 5.5	3
4.333 – 4.667	11	5.5 – 6	2
4.667 – 5	8	6 – 6.5	2
5 – 5.333	9	7 – 7.5	1
5.333 – 5.667	8	8 – 8.5	1
5.667 – 6	14	–	–
6 – 6.333	6	–	–
6.333 – 6.667	9	–	–
6.667 - 7	5	–	–
7 – 7.333	6	–	–
7.333 – 7.667	2	–	–
7.667 – 8	6	–	–
9 – 9.333	5	–	–
9.333 – 9.667	2	–	–
10.333 – 10.667	1	–	–

The representative diameters for the distributions are given below in Table 6.2.

Table 6.2: Values of the representative diameters of polydisperse drop distributions *A* and *B*.

Description	Symbol d_{pq}	Distribution *A* [mm]	Distribution *B* [mm]
Average diameter	d_{10}	3.219	1.284
Mean volume diameter	d_{30}	4.354	2.029
Pierce diameter	d_{41}	5.553	3.131
Sauter mean diameter	d_{32}	5.734	3.256

For each distribution there are three different simulation conditions, the input data of which are given in the tables below. Table 6.3 presents all the input data that remains constant and is common to all three simulation conditions. Table 6.4 presents the variable input data which differs for the three simulation conditions.

Table 6.3: Common input data for natural draught circular wet-cooling tower and counterflow CFD simulations.

Property	Value
Dynamic viscosity of air, μ_a [kg/ms]	1.794×10^{-5}
Thermal conductivity of air, k_a [W/mK]	0.0253
Diffusion coefficient, D [m^2/s]	2.34×10^{-5}
Density of water drops, ρ_w [kg/m^3]	997.87
Specific heat of water drops, c_v [J/kgK]	4178.33
Latent heat of water drops, h_{fg} [J/kg]	2.5016×10^{6}
Ambient air pressure, p_a [N/m^2]	84100
Air drybulb temperature, T_a [K]	288.6
Turbulence intensity, [%]	2
Turbulence length scale, [m]	0.1

Table 6.4: Simulation specific input data for natural draught circular wet-cooling tower and counterflow CFD simulations.

	Inlet ambient relative humidity, Φ [-]	Inlet water drop temperature, T_d [K]
Simulation 1	0.6	295.65
Simulation 2	0.6	300.00
Simulation 3	0.1	295.65

For the counterflow flow domain, a constant inlet velocity of *1.975m/s* is used at the *velocity inlet* boundary. The mass flow of the water in this flow domain is also constant for all the simulations and equal to *3.39kg/s*. For the natural draught circular wet-cooling tower flow domain the water and air mass flow rates are held constant throughout, at *12450kg/s* and *16556kg/s* respectively. The saturation

pressure of water vapour is a function of the drop temperature and can be represented by means of a fourth order polynomial, given by,

$$p_{vs}(T_d) = 529.769\times10^{-6}T_d^4 - 561.1063\times10^{-3}T_d^3 + 224.2787T_d^2 - 40045.99T_d + 2695480 \quad (6.1)$$

6.3.3 Fill simulation

Terblanche and Kröger [1994TE1] show that the inlet loss is a function of the pressure drop over the fill, thus the fill needs to be modelled accurately. For these simulations only orthotropic resistance type fill was used. FLUENT 6.2.16 can model such a film type fill by means of a porous zone. The resistance of the porous zone (fill) is determined using a power law of the form:

$$\Delta p = C_0 v^{C_1} \quad (6.2)$$

The coefficients, C_0 and C_1, can be found directly from the definition of the fill loss coefficient,

$$\Delta p = \frac{1}{2}\rho v^2 K_{fi} \quad (6.3)$$

where K_{fi} is the loss coefficient of the fill, so that C_0 and C_1 become

$$C_0 = \frac{1}{2}\rho K_{fi} / L_{fi,CFD}$$
$$C_1 = 2 \quad (6.4)$$

where $L_{fi,CFD}$ is the length of the porous zone (fill) in the CFD model. For the natural draught circular wet-cooling tower simulations a C_0 value of *11.06* is used.

6.3.4 Drop Modelling

Due to the time-derivative Lagrangian tracking scheme, initial conditions for the drops are needed. FLUENT 6.2.16 is able to import a file that contains all the necessary inputs. This technique is thus easily adaptable for poly- and monodisperse drop distributions. The necessary inputs are the initial conditions for the position, velocity, temperature, diameter and mass flow rate to be released from the specific point. A program was written that generates this file for the various simulations.

A constant pitch of *25mm* for the position of the initial points was used, as this was the pitch of the orthotropic fill used in the experimental work. The drops were given only a vertical velocity of *0.1m/s* in the direction of gravity, this helps eliminate infinities at flow initialisation. The temperature and diameter of the

drops depend on the simulation. For the mass flow rate of the water, it was decided that a constant water mass velocity along the radius of the circular wet-cooling tower domain, and also over the water inlet of the counterflow domain was desirable, thus the water mass flow rate was distributed accordingly.

The pond is defined as a *wall* boundary in the circular wet-cooling tower domain, Figure 6.2, when drops reach the pond they are removed from the flow domain, by setting the discrete phase fate to *escape* in the *wall* boundary conditions. The same applies to drops in the counterflow flow domain when they reach the *velocity inlet* boundary (air inlet), Figure 6.1.

6.4 Results

The results of the simulations for the polydisperse drop distributions *A* and *B* are given in table format below. The results are presented in the form of loss coefficients and Merkel numbers.

Table 6.5: Results for the natural draught circular wet-cooling tower flow domain.

	Distribution *A*			Distribution *B*		
	Simulation 1	Simulation 2	Simulation 3	Simulation 1	Simulation 2	Simulation 3
K_{ct} [-]	10.952	11.271	10.930	12.440	13.484	12.402
Me [-]	0.190	0.184	0.195	0.404	0.388	0.420

Table 6.6: Results for the counterflow flow domain.

	Distribution *A*			Distribution *B*		
	Simulation 1	Simulation 2	Simulation 3	Simulation 1	Simulation 2	Simulation 3
K_{ct} [-]	2.092	2.239	2.125	3.553	3.561	3.580
Me [-]	0.110	0.107	0.112	0.282	0.270	0.293

The results above will serve as reference values for comparative purposes in subsequent chapters.

Summary

This chapter presents the procedure followed to setup a CFD model that can perform polydisperse and monodisperse drop distribution calculations as well as help determine the loss coefficient and Merkel number, for both a counterflow and a natural draught circular wet-cooling tower flow domain. The CFD model is setup such that the flow field in the rain zone is a realistic representation. The boundary conditions and input data are given and discussed where necessary. The results from the simulations are presented for the two polydisperse drop distributions subject to the three simulation conditions.

CHAPTER

7

Modelling of the Rain Zone Loss Coefficient

This chapter will investigate the modelling of a polydisperse drop distribution with a monodisperse drop distribution with regards to the loss coefficient, and in doing so define a new representative diameter. The investigation is done using a commercial CFD package, FLUENT 6.2.16, to find the pressure drop over a counterflow domain as well as the inlet section of a circular wet-cooling tower domain. The results will be validated with relevant experimental correlations and then used to validate the mathematical correlations for the rain zone loss coefficient given by De Villiers and Kröger [1998DE1].

7.1 Background

The equations for loss coefficient determined by De Villiers and Kröger [1998DE1] are obtained from a two-dimensional model that was one-dimensionalised. They applied a method that uses experimental data for the absolute value of the inlet loss coefficient in the absence of a rain zone. Then by using CFD, the relative influence of the rain zone on the inlet loss coefficient is found, this is then applied to the experimental inlet loss coefficient to find an approximation of the inlet loss coefficient in the presence of a rain zone. This is illustrated in the equation set below,

$$K_{ct(wet)} = C_{rz} K_{ct(dry)}$$

where

$$C_{rz} = \frac{K_{ct(wet,CFD)}}{K_{ct(dry,CFD)}}$$

They derive their one-dimensional rain zone loss coefficient by correlating data determined by numerical integration of an analytically determined equation that incorporates a two-dimensional potential flow field and the equations of motion of a single drop. This method is employed for various tower geometries. The correlations make provision for a monodisperse drop distribution and can not be used in conjunction with a polydisperse drop distribution. De Villiers and Kröger [1998DE1] did not measure the polydisperse drop distribution in a wet-cooling

tower. They determined which single diameter correlated their experimental data best. The aforementioned two-dimensional potential flow field is unrealistic in the sense that it does not allow for flow recirculation at the inlet, assumes the axial velocity at the fill height to be uniform, assumes a uniform inlet velocity distribution and does not include the acceleration of the flow at the inlet.

FLUENT 6.2.16 is able to determine the loss coefficient for various multi-dimensional geometries by determining the pressure drop over a specified domain. The code presents an absolute value for the pressure drop over a domain; that is it is the cumulative result of the pressure drop due to the rain zone, tower geometry, turbulence etc. It is not possible to isolate the various pressure drops as well as the influences that each has on the rest or the absolute value.

An objective of this chapter is to model the rain zone loss coefficient using a commercial CFD package.

Hollands and Goel [1976HO1] state that it is not possible to model a polydisperse drop distribution with a monodisperse drop distribution accurately, they proved it analytically. This is verified by comparing the results obtained for the rain zone loss coefficient using a polydisperse drop distribution to those for different monodisperse drop distributions.

One-dimensional theoretical models are simple to understand and easy to implement, whereas numerical methods tend to be relatively expensive concerning time and money and require CFD expertise. Thus the final objective of this chapter is to validate the one-dimensional rain zone loss coefficients given by De Villiers and Kröger [1998DE1].

7.2 Analysis Procedure

FLUENT 6.2.16 reports an area-weighted-average total pressure for a pre-defined plane. The total energy loss experienced by the flow between the ambient conditions and the bottom of the fill can now be calculated. This value, calculated using Equation (7.1), represents the total loss due to the inlet, rain zone, recirculation etc.

A point of interest, is the velocity distribution across the top of the fill for the circular wet-cooling tower case as presented in Figure 7.1. The velocity is fairly uniform across the top of the fill but drops suddenly near the inlet of the tower, $r = 52.25m$. This is where flow recirculation occurs. The presence of a rain zone has noticeable effects on the velocity distribution, the first being that it seems to increase the effective flow area and secondly the velocity distribution appears to be slightly more uniform.

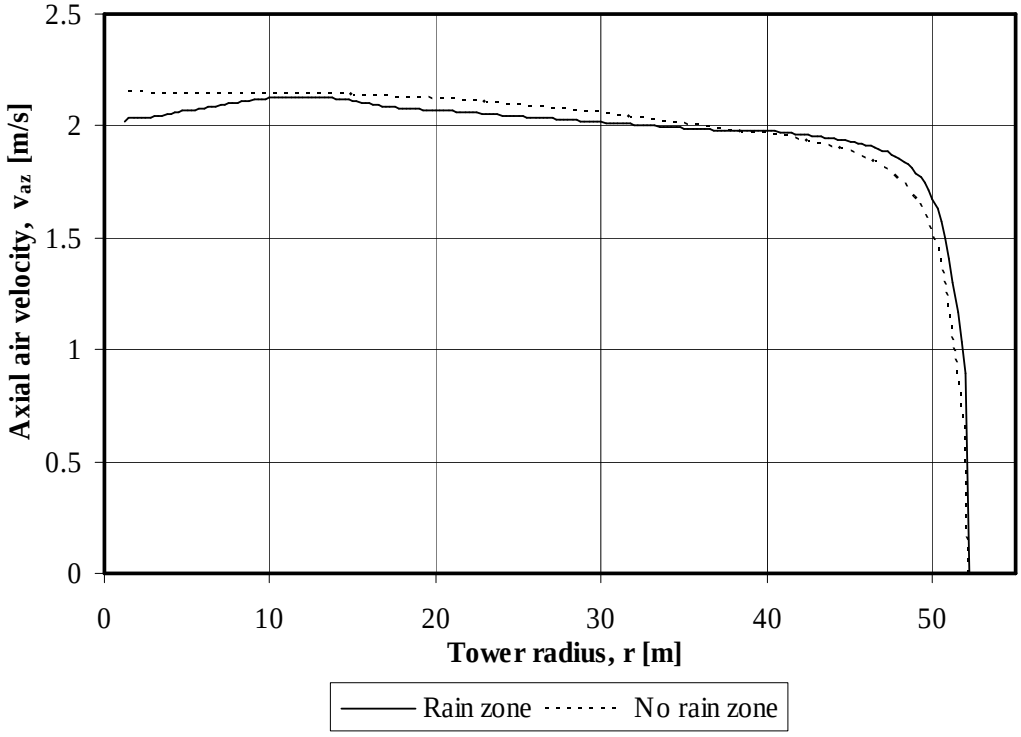

Figure 7.1: Velocity distribution across the top of the fill as a function of the radius.

The total loss coefficient, defined in terms of the mass flow averaged fill inlet velocity, is given by,

$$K_{t(wet)} = \frac{p_a - \left(p_{s,fi} + \alpha_{fi} \frac{1}{2} \rho v_{fi}^2 + \rho g H_{fi} \right)}{\frac{1}{2} \rho v_{fi}^2} \tag{7.1}$$

where the subscript *fi* denotes the conditions at the inlet to the fill, p_a is the atmospheric pressure at ground level, H_{fi} is the height of the fill above the ground level and α_{fi} is the velocity distribution correction factor that is taken as unity. The inlet loss coefficient for a cooling tower can now be found from,

$$K_{ct(wet)} = K_{t(wet)} - K_{rz} \tag{7.2}$$

The rain zone loss coefficient, K_{rz}, is given later in this section.

Terblanche and Kröger [1994TE1] propose the following correlation for the inlet loss coefficient of circular cooling towers with rounded inlets ($r_i/d_i \approx 0.01$) where the heat exchanger is installed horizontally, such that it covers the entire cross-section of the cooling tower at the upper ring beam level, given by,

$$K_{ct(dry)} = 1.5\,exp\left(0.2\frac{d_i}{H_i}\right)K_{fi}^{\left[-0.4645+0.02303\left(\frac{d_i}{H_i}\right)-0.00095\left(\frac{d_i}{H_i}\right)^2\right]} \tag{7.3}$$

for $10 \le d_i/H_i \le 15$ and $5 \le K_{fi} \le 25$.
The work done by Terblanche and Kröger [1994TE1] was done on dry-cooling towers, however the material used for the heat exchangers in the experiments is geometrically similar to orthotropic film type fill, thus the equation is valid for the dry case of wet-cooling towers installed with orthotropic type fill.

The CFD model for a circular wet-cooling tower, presented in Chapter 6, is used to determine the inlet loss coefficient, $K_{ct(dry)}$, for different d_i/H_i values, without the presence of a rain zone. These values are then compared with the experimental correlation, Equations (7.3), in this way validating the CFD code.

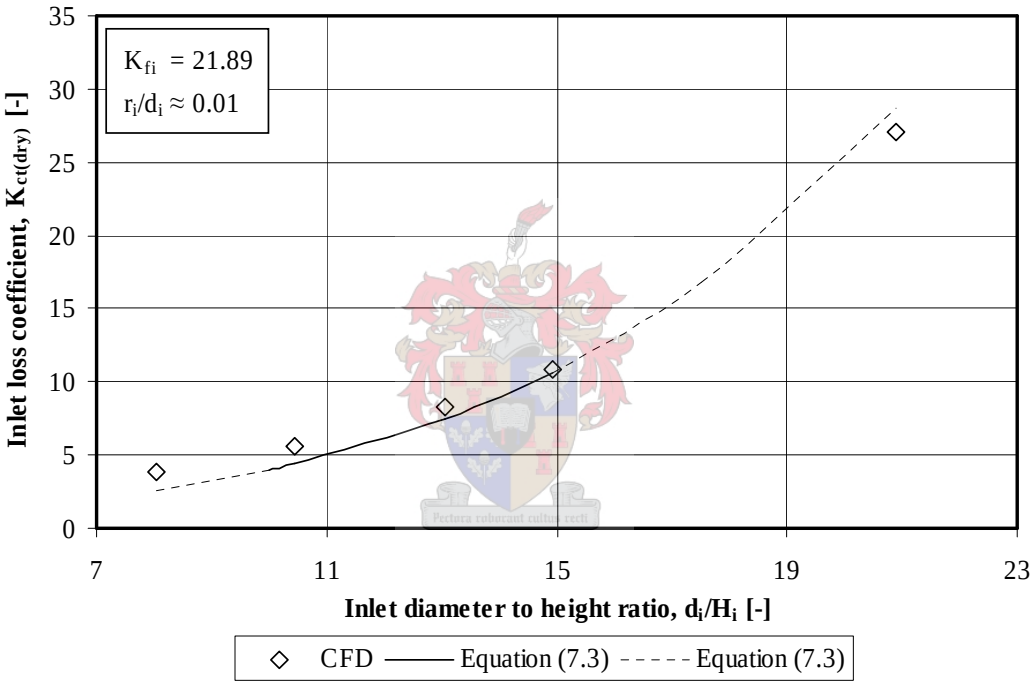

Figure 7.2: Inlet loss coefficient for circular cooling towers with orthotropic fill but no rain zone as a function of d_i/H_i.

The general validity of the analysis for this chapter is dependent on the degree of similarity between the experimental correlation and the CFD results. An interesting point to note about Equation (7.3) is that it corresponds well with the numerical results even outside of its validity range. For the purposes of this thesis Equation (7.3) will be used when determining the dry inlet loss coefficient for a circular cooling tower. In general, the agreement between the two approaches is sufficient to give confidence in further results obtained using CFD.

De Villiers and Kröger [1998DE1] state that the presence of the rain zone reduces the dry inlet loss coefficient. Figure 7.1 shows that the rain zone has an

effect on the velocity distribution, however it can not be said what effect it has on the inlet loss coefficient. A quantitative analysis of this effect is not provided in this thesis. De Villiers and Kröger [1998DE1] give the wet inlet loss coefficient as,

$$K_{ct(\,wet\,)} = C_{rz} K_{ct(dry)} \tag{7.4}$$

where C_{rz} is a rain zone correction factor, given by,

$$\begin{aligned} C_{rz} = & \left[\begin{array}{l} 0.2394 + 80.1\left(0.0954/\left(d_i/H_i\right) + d_d\right) exp\left(0.395 G_w/G_a\right) \\ -0.3195\left(G_w/G_a\right) - 966\left(d_d/\left(d_i/H_i\right)\right) exp\left(0.686 G_w/G_a\right) \end{array} \right] \\ & \times \left(1 - 0.06825 G_w\right) K_{fi}^{0.09667}\, exp\left(8.7434\left(1/d_i - 0.01\right)\right) \end{aligned} \tag{7.5}$$

The total loss coefficient due to the rain zone and inlet losses can be found by substituting Equation (7.4) into Equation (7.2) to give,

$$K_{t(wet)} = C_{rz} K_{ct(dry)} + K_{rz} \tag{7.6}$$

where K_{rz} for a circular cooling tower is given by De Villiers and Kröger [1998DE1] as,

$$\begin{aligned} K_{rz} = & 3 a_v v_w \left(\frac{H_i}{d_d}\right) [0.2246 - 0.31467 a_\rho \rho_a + 5263.04 a_\mu \mu_a \\ & + 0.775526 [1.4824163 \exp\left(71.52 a_L d_d\right) - 0.91] \\ & \times \left[0.39064 \exp\left(2.1824 \times 10^{-2} a_L \frac{d_i}{2} \right) - 0.17 \right] \left[2.0892 \left(a_v v_i\right)^{-1.3944} + 0.14 \right] \\ & \times \exp[\left(0.8449 \ln\left(a_L \frac{d_i}{2} \right) - 2.312 \right) \left(0.3724 \ln\left(a_v v_i\right) + 0.7263\right) \\ & \times \ln\left[206.757 \left(a_L H_i\right)^{-2.8344} + 0.43 \right]]] \end{aligned} \tag{7.7}$$

and for a counterflow domain, is given as,

$$\begin{aligned} K_{rz} = & a_v v_w [10645988 a_\mu \mu_a - 130.7774 a_\rho \rho_a - 32.6634 \\ & + 888.6645 [2.45287 \left(a_v v_i\right)^{-1.93315} + 0.34] \\ & \times \left[4.03861 \exp\left(-574.542 a_L d_d\right) + 0.493 \right] \\ & \times \exp[\left(65.26215 a_L d_d + 0.74827\right) \\ & \times \ln\left[6.09836 \exp\left(0.0767 a_L H_i\right) - 6.1 \right]]] \end{aligned} \tag{7.8}$$

where

$$a_\mu = 3.061\times10^{-6}\left[\frac{\rho_w^4 g^9}{\sigma_w}\right]^{0.25}$$
$$a_\rho = \frac{998}{\rho_w}$$
$$a_v = 73.298\left[\frac{g^5\sigma_w^3}{\rho_w^3}\right]^{0.25} \qquad (7.9)$$
$$a_L = 6.122\left[\frac{g\sigma_w}{\rho_w}\right]^{0.25}$$

for $2 \le d_d \le 8mm$.
Using Equations (7.1) and (7.6) the results of CFD and the one-dimensional model of De Villiers and Kröger [1998DE1] are compared.

For the counterflow case the analysis is far more direct. Due to the essentially one-dimensional nature of the flow, there will be no losses due to curvature and recirculation, thus the total loss over the domain is essentially a function of the drag forces of the drops acting on the air, as discussed in Chapter 5.

For the same simulation condition, the total loss coefficient for polydisperse and monodisperse drop distributions is determined, using the representative diameters for the monodisperse drop distributions. If the value given by the polydisperse drop distribution is taken as the reference value, then the difference between this result and the result obtained for the monodisperse drop distributions can be determined from,

$$\Delta K = K_{mono} - K_{poly} \qquad (7.10)$$

If $\Delta K = 0$, the corresponding diameter of the monodisperse drop distribution is considered to be the equivalent monodisperse diameter for approximating the total loss coefficient of a polydisperse drop distribution. The values given by the one-dimensional model of De Villiers and Kröger [1998DE1], using the representative diameters, are compared in the same way.

7.3 Results

Vector and contour plots of the flow field in the circular wet-cooling tower are presented in Figures 7.3 and 7.4.

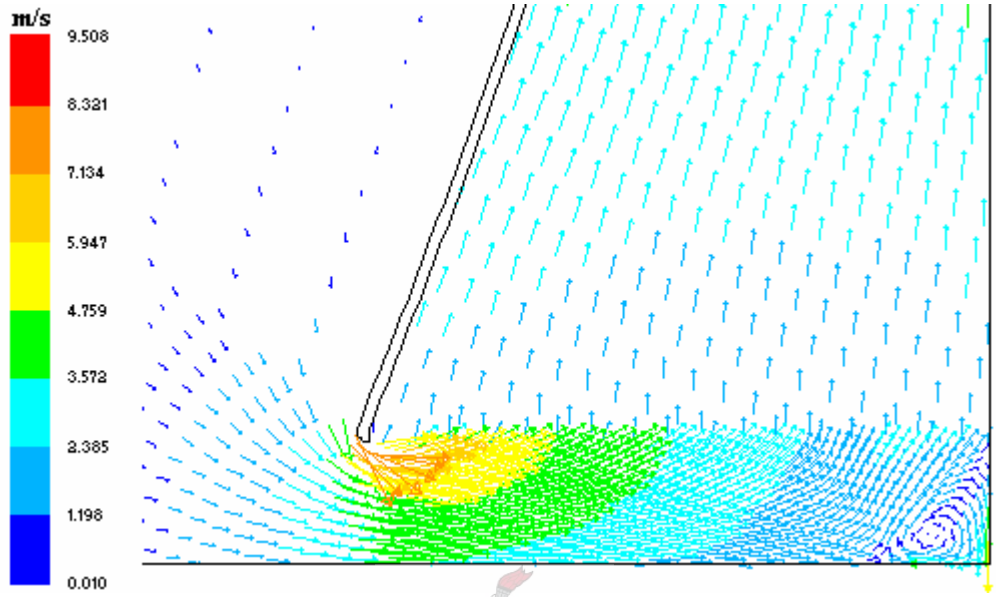

Figure 7.3: Vector plot of the inlet flow of a circular wet-cooling tower.

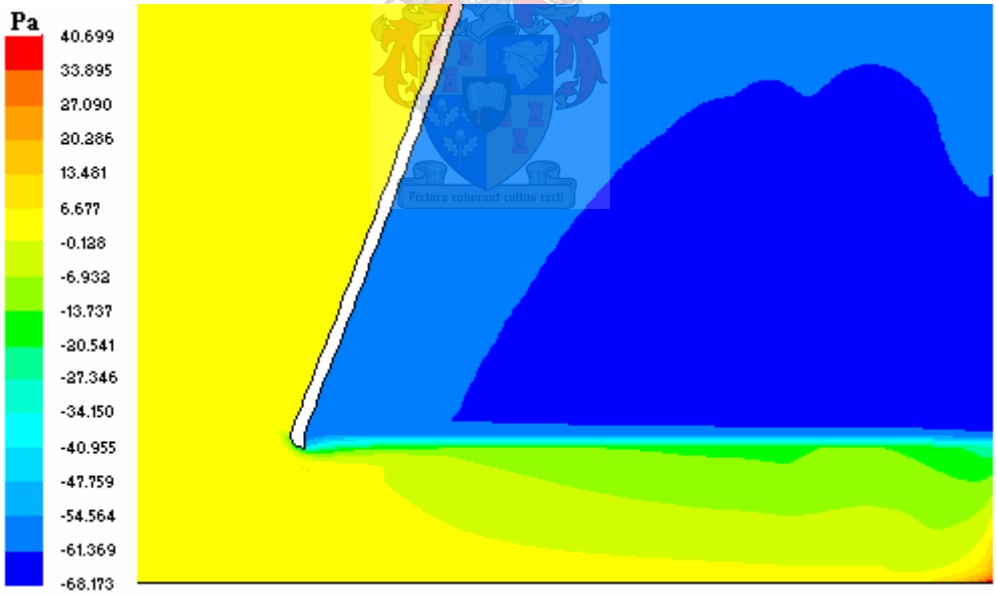

Figure 7.4: Contour plot of the total gauge pressure at the inlet of a circular wet-cooling tower.

Figure 7.3 shows the acceleration along the inlet rounding and that the flow is allowed to freely develop at the tower inlet. Similar to Figure 7.1 the velocity distribution above the fill appears to be relatively uniform. A recirculation zone is present at the tower axis, this is not present in the dry tower simulations nor in a potential flow field, as it is caused by the rain zone.

The total gauge pressure contour plot, Figure 7.4, shows the effect of the rain zone on the pressure distribution.

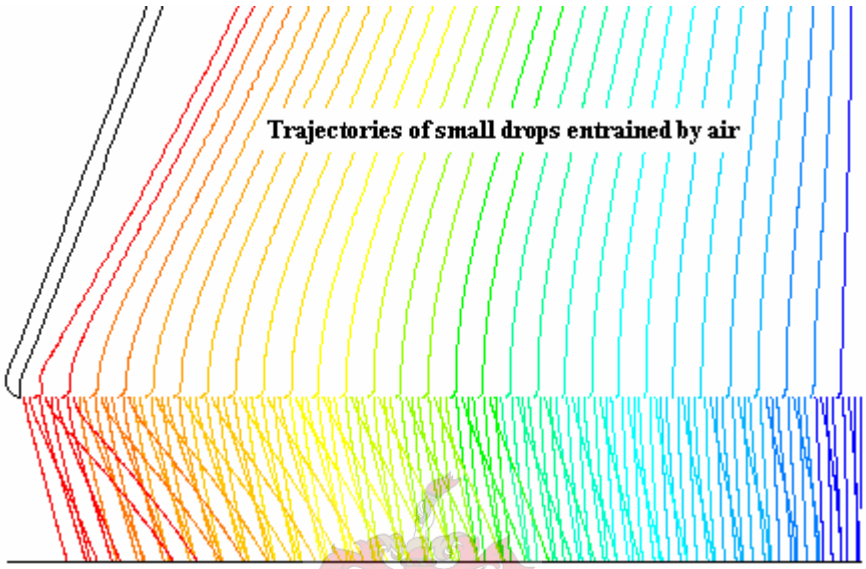

Figure 7.5: Drop trajectories of a polydisperse drop distribution.

The trajectories for the drops of a polydisperse drop distribution can be seen in Figure 7.5. It is seen that the smallest drops are entrained into the air flow and that the trajectories of different drop sizes differ. Smaller drops are carried into the tower more by the air than larger drops.

7.3.1 Circular Cooling Tower Domain

Figure 7.6 is used to compare the results for the total loss coefficient given by CFD and De Villiers and Kröger [1998DE1] for a circular wet-cooling tower. The results of one simulation condition are given. The loss coefficient for the three simulations did not differ significantly. The figure presents the results obtained for different monodisperse drop distributions compared with the results obtained for both polydisperse drop distributions, refer to Section 6.3.2, subject to the conditions of *simulation 1*. The two methods correspond well, even beyond the lower validity limit given by De Villiers and Kröger [1998DE1].

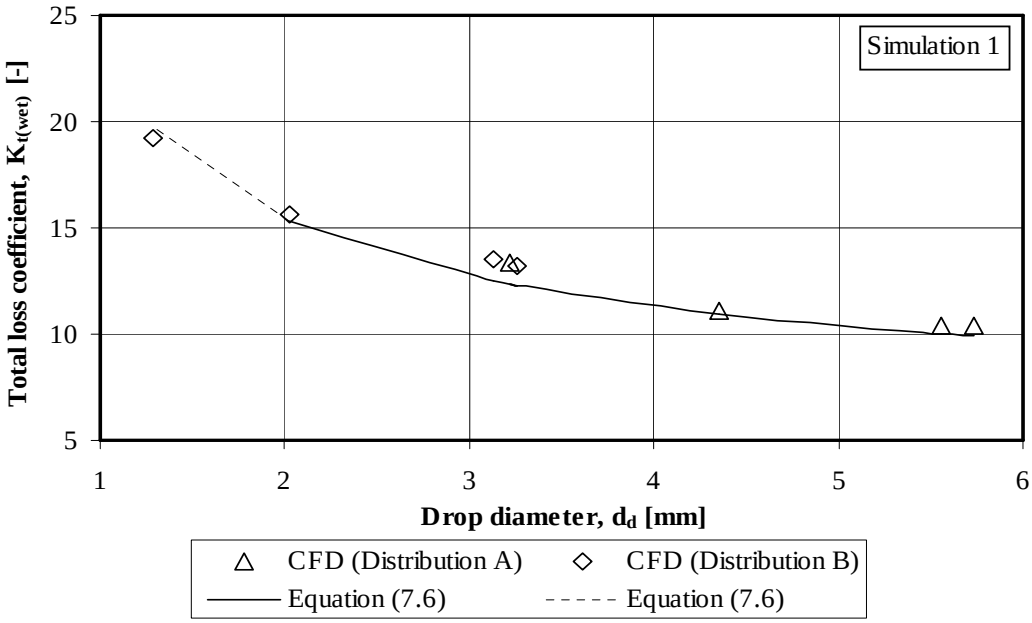

Figure 7.6: Total loss coefficient of a circular wet-cooling tower as a function of drop diameter.

In subsequent figures in this section, the diameters are given from left-to-right as: d_{10} *(average);* d_{30} *(mean volume);* d_{41} *(Pierce)* and d_{32} *(Sauter mean)* defined according to the ASTM standards discussed in Chapter 4. The d_{41} diameter is one that was developed in this thesis, and adheres to the same arithmetical determination technique given in the ASTM standards.

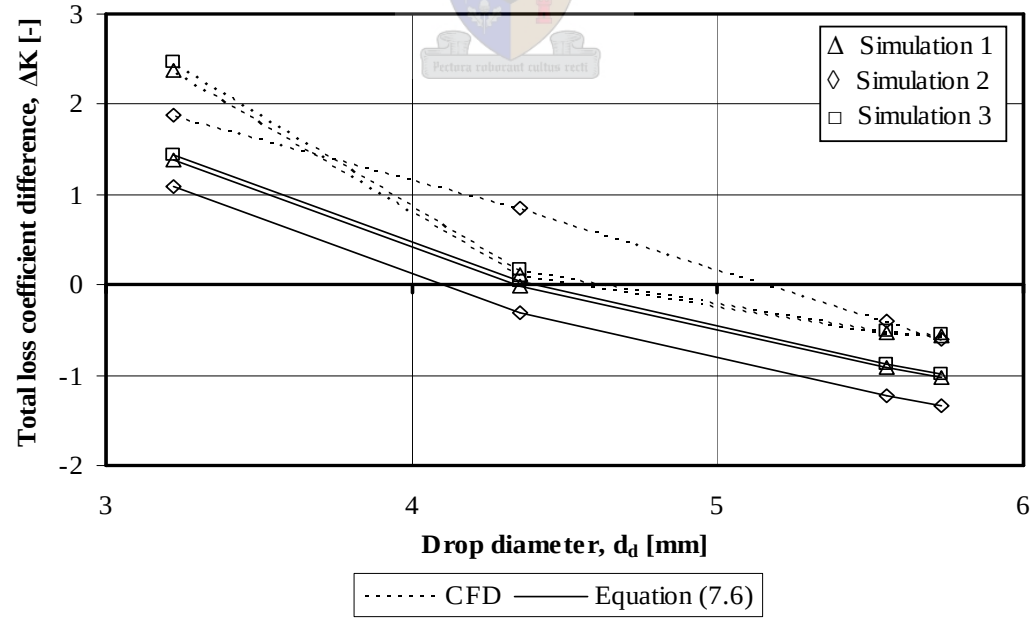

Figure 7.7: Total loss coefficient difference as a function of monodisperse drop diameter for distribution *A*.

Figure 7.7 and 7.8 are for polydisperse drop distributions *A* and *B* respectively. The figures are used to demonstrate the difference in total loss coefficient, ΔK, using Equation (7.10), determined by CFD and De Villiers and Kröger [1998DE1]. Table 7.1 gives an average absolute of the total loss coefficient difference, ΔK.

Table 7.1: Average absolute of ΔK for the analysis of distribution *A*.

	d_{10} = 3.219mm [%]	d_{30} = 4.354mm [%]	d_{41} = 5.553mm [%]	d_{32} = 5.734mm [%]
CFD	20	3	4	5
Equation (7.6)	12	1	9	10

From Table 7.1, which has reference to Figure 7.7, it can be seen that for both methods the *Pierce* and *mean volume* diameters present the smallest ΔK values.

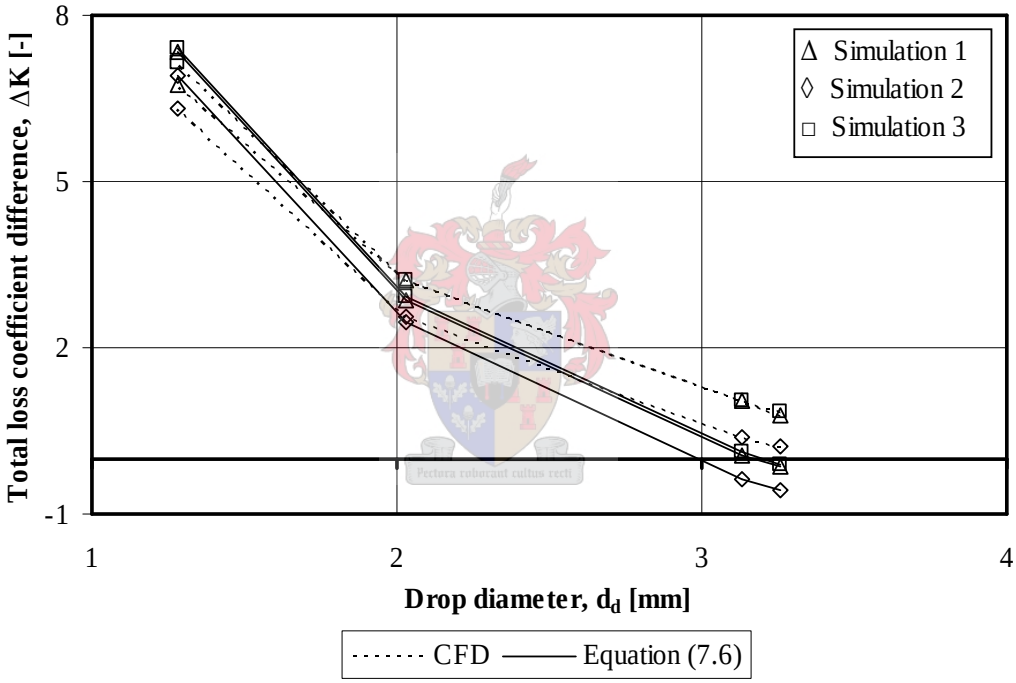

Figure 7.8: Total loss coefficient difference as a function of monodisperse drop diameter for distribution *B*.

Table 7.2 gives an average absolute of the total loss coefficient difference, ΔK.

Table 7.2: Average absolute of ΔK for the analysis of distribution *B*.

	d_{10} = 1.284mm [%]	d_{30} = 2.029mm [%]	d_{41} = 3.131mm [%]	d_{32} = 3.256mm [%]
CFD	54	24	7	5
Equation (7.6)	57	22	1	2

There is a clear shift in accuracy; the *Sauter mean* and *Pierce* diameters now present the smallest ΔK values for both methods. The method of De Villiers and Kröger [1998DE1] seems to present smaller ΔK values than CFD for this particular analysis.

Referring to Figure 7.6, for distribution *B*, the reference value for the total loss coefficient is *12.44*, Chapter 6. The representative diameters for this distribution lie in the range $1.28 \leq d_{pq} \leq 3.25mm$. In this range there is only one instance where the value presented by CFD is closer to the reference value, this is for the *average diameter*. Thus this diameter using CFD will have a smaller deviation in Table 7.2 than the method of De Villiers and Kröger [1998DE1]. Using the same approach and a reference value for the total loss coefficient of *10.95* for distribution *A* with a representative diameter range of $3.21 \leq d_{pq} \leq 5.73mm$ the values in Table 7.1 can be verified.

7.3.2 Counterflow Domain

Due to the fact that the presentation procedure of the results is similar to the previous section, only figures and tables will be given, with explanations where necessary.

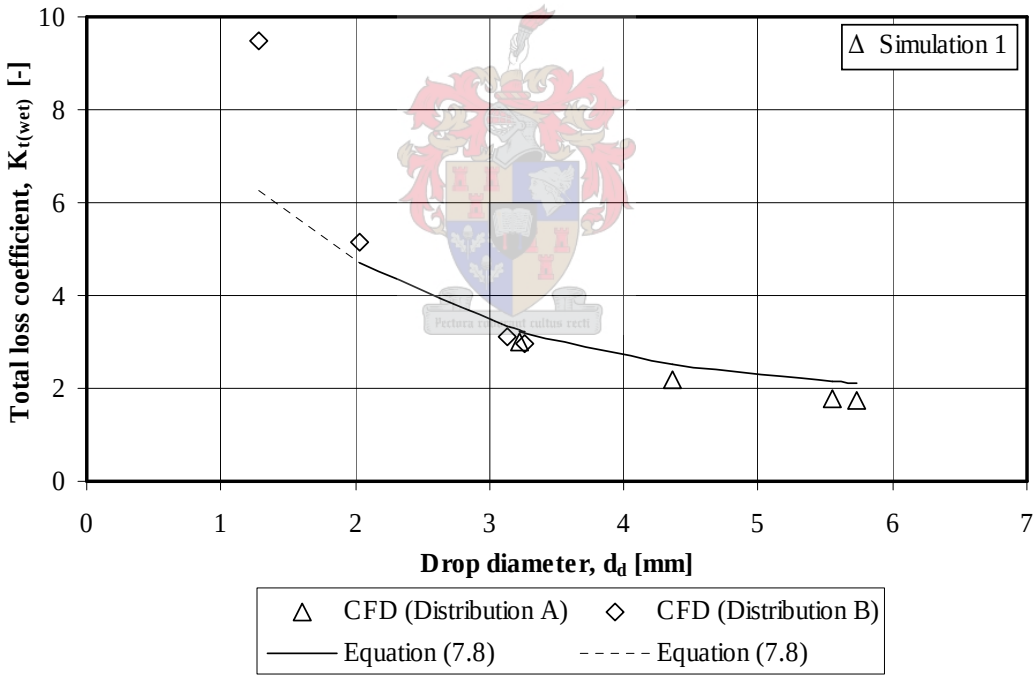

Figure 7.9: Total loss coefficient of a counterflow domain as a function of monodisperse drop diameter.

Figure 7.9 shows that the two methods correspond well except below the lower validity limit given by De Villiers and Kröger [1998DE1].

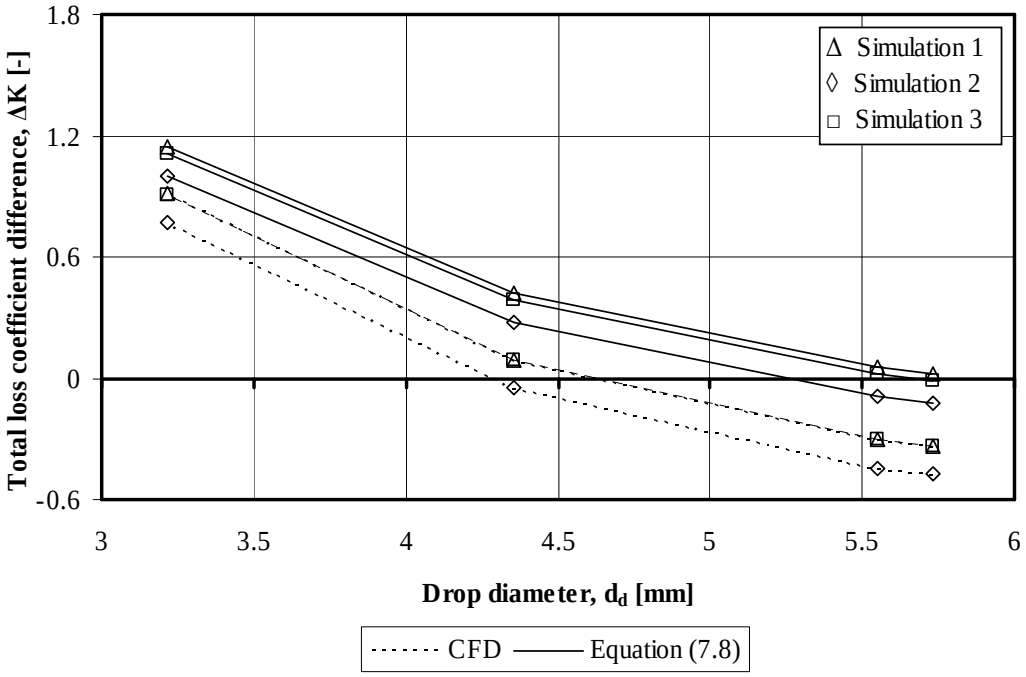

Figure 7.10: Total loss coefficient difference as a function of monodisperse drop diameter for distribution *A*.

Table 7.3: Average absolute of *ΔK* for the analysis of distribution *A*.

	d_{10} = 3.219mm [%]	d_{30} = 4.354mm [%]	d_{41} = 5.553mm [%]	d_{32} = 5.734mm [%]
CFD	40	4	16	18
Equation (7.8)	51	17	3	2

Referring to Table 7.3 and Figure 7.10, it can be seen that the *Pierce* and *Sauter mean* diameters present the smallest *ΔK* values for the method of De Villiers and Kröger [1998DE1]. CFD presents the smallest *ΔK* value using the *mean volume* diameter.

Applying the approach of Section 7.3.1 and using a reference value for the total loss coefficient of *2.092*, Chapter 6, and a representative diameter range of $3.21 \leq d_{pq} \leq 5.73mm$ the values in Table 7.3 can be verified.

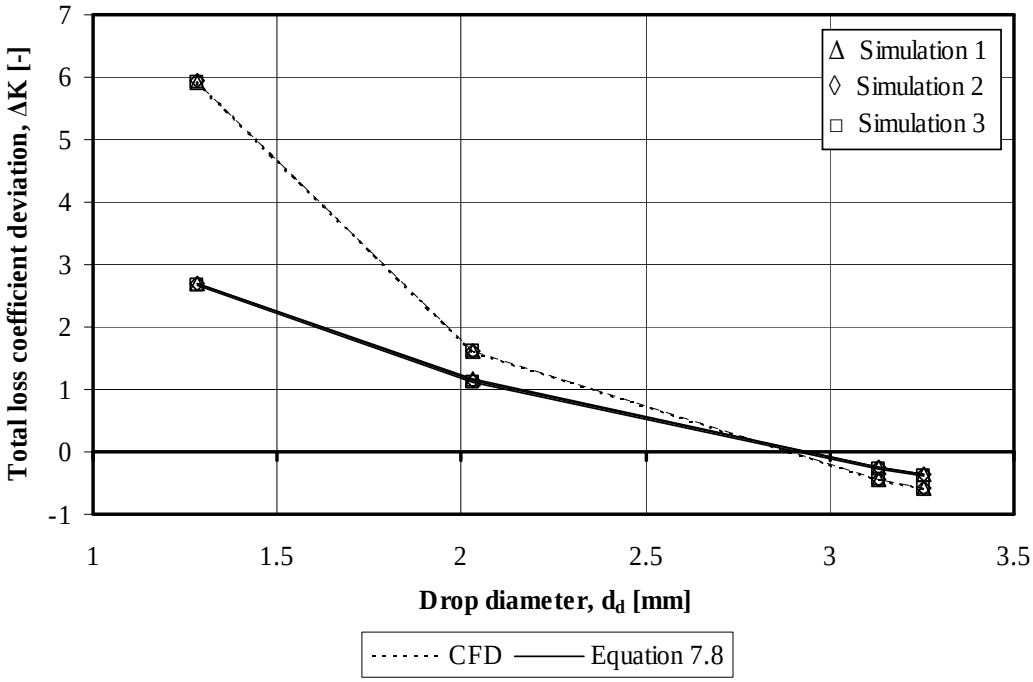

Figure 7.11: Total loss coefficient difference as a function of monodisperse drop diameter for distribution *B*.

Table 7.4: Average absolute of *ΔK* for the analysis of distribution *B*.

	d_{10} = 1.284mm [%]	d_{30} = 2.029mm [%]	d_{41} = 3.131mm [%]	d_{32} = 3.256mm [%]
CFD	166	45	13	16
Equation (7.8)	75	32	7	10

The *Pierce* and *Sauter mean* diameters present the smallest *ΔK* values for this particular analysis. Applying the approach of Section 7.3.1 and using a reference value for the total loss coefficient of *3.55*, Chapter 6, and a representative diameter range of $1.28 \leq d_{pq} \leq 3.25mm$ the values in Table 7.4 can be verified.

Summary

This chapter set out to analyse a circular wet-cooling tower and a counterflow domain with regards to the loss coefficient.

FLUENT 6.2.16 was used to determine the inlet loss coefficient of a circular cooling tower, the results were compared with existing experimental correlations for circular cooling towers with orthotropic type fill. The results compared very satisfactorily, this served as a validation of the CFD code.

Employing the methods given by De Villiers and Kröger [1998DE1] and CFD, together with the different monodisperse drop distributions, the total loss coefficients were determined. The values were compared and found to be in good

agreement, in the order of *5%* and *10%* for the circular cooling tower and counterflow domains respectively. The method of De Villiers and Kröger [1998DE1] for determining the total loss coefficient of a circular wet-cooling tower and a counterflow domain was validated.

The values of the total loss coefficient for both methods, employing the different monodisperse drop distributions, were then compared to the reference value determined by using the polydisperse drop distribution and CFD. It was found that no single representative drop diameter modelled the polydisperse drop distribution precisely, concerning the loss coefficient.

From work done in this thesis a new representative drop diameter, d_{41} *(Pierce)*, was defined. Employing both methods, this diameter and the *Sauter mean* in general model the polydisperse drop distribution the best for the analyses presented here.

CHAPTER

8

Modelling Rain Zone Heat and Mass Transfer

This chapter will investigate the feasibility of modelling a polydisperse drop distribution with a monodisperse drop distribution with regards to the Merkel number. The CFD investigation is done to find the heat and mass transfer over a counterflow domain as well as a circular wet-cooling tower domain. The mathematical correlations for the rain zone Merkel number proposed by De Villiers and Kröger [1998DE1] will be validated.

8.1 Background

In large counterflow wet-cooling towers, as much as *10-20%* of the total heat rejection occurs in the rain zone, which can be increased. This is the motivation for obtaining better insight into the characteristics of the rain zone.

Prior to De Villiers and Kröger [1998DE1] there were some relations that described the Merkel number of the rain zone, however they tended to be incorrect or limited to a narrow range of variables. In light of this De Villiers and Kröger [1998DE1] presented a one-dimensional correlation for the Merkel number. Their method for determining the Merkel number is similar to that of their rain zone loss coefficient, Chapter 7, based on a monodisperse drop distribution.

More recently Fisenko et al. [2004FI1] presented a mathematical model for predicting the performance of a mechanical draft cooling tower. This model determines the change in the drops' diameter, velocity and temperature and the change in the temperature and density of the air-vapour mixture in a cooling tower. The model predicts available experimental data with a deviation of about *3%*. Their mathematical model incorporates a polydisperse drop distribution but ignores drop deformation.

FLUENT 6.2.16 is able to determine the heat and mass transfer between the drop phase and the continuous phase. These values are used to determine the Merkel number for the flow domain.

Williamson et al. [2006WI1] used FLUENT to simulate a two-dimensional axisymmetric two-phase simulation of the heat and mass transfer inside a natural draft wet-cooling tower, with the aim of optimising the design of cooling towers by varying the fill depth and water flow rate in the tower. Their model employs correlations from Kloppers and Kröger [2003KL1] for the fill loss coefficient and Merkel number. The effect of the fill on the continuous phase is represented using

source terms. The temperature of the drops entering the rain zone is determined by the temperature of the water leaving the fill. They make use of a monodisperse drop distribution with a drop diameter of *2.5mm*.

An objective of this chapter is to develop a methodology for modelling the rain zone transfer coefficient using a commercial CFD package. This is then used to validate the one-dimensional rain zone Merkel numbers proposed by De Villiers and Kröger [1998DE1] for counterflow and circular wet-cooling tower domains.

Further objectives are to: investigate which representative diameter gives comparable results to the polydisperse drop distribution and to validate the use of the Chebyshev integration in the determination of the Merkel number for the rain zone of a wet-cooling tower.

8.2 Analysis Procedure

The Merkel equation is given below,

$$\frac{\bar{h}_d A}{m_w} = \int_{T_{wo}}^{T_{wi}} \frac{c_{pw} dT_w}{\left(h_{masw} - h_{ma}\right)} \tag{8.1}$$

where $\bar{h}_d$ is the interfacial area-averaged mass transfer coefficient, A the total interfacial surface area and m_w the total mass flow rate of water in the domain.

Traditionally, the Merkel number is calculated from experimental data using the Chebyshev integration approach,

$$\int_a^b f(x)\,dx \approx \frac{(b-a)}{4}\left[f(x_1) + f(x_2) + f(x_3) + f(x_4) \right] \tag{8.2}$$

The values of *f(x)* are evaluated at values of x which are *0.102673*, *0.406204*, *0.593796* and *0.897327* of the interval *(b-a)*.

Another approach is proposed and the results are compared to the values determined using the Chebyshev integration. Consider the equation of mass transfer from a single drop, given by,

$$m_{evap} = h_d A_d \left(\omega_d - \omega_a\right) \tag{8.3}$$

where the subscripts *d* and *a* are for the conditions of the humidity ratio at the drop surface and the air respectively. Manipulation of Equations (8.1) and (8.3) yields a new determination technique for the Merkel number,

$$\frac{\bar{h}_d A}{m_w} = \frac{m_{evap}}{m_w \int_1^2 (\omega_d - \omega_a) dA} \tag{8.4}$$

Figure 8.1 shows the change in humidity ratio of the air at the water drop surface and of the air as the water and air move through the cooling tower, where, $\Delta\omega_1$ and $\Delta\omega_2$ represent $(\omega_d - \omega_a)$ at the *air outlet* and the *air inlet* of the wet-cooling tower respectively.

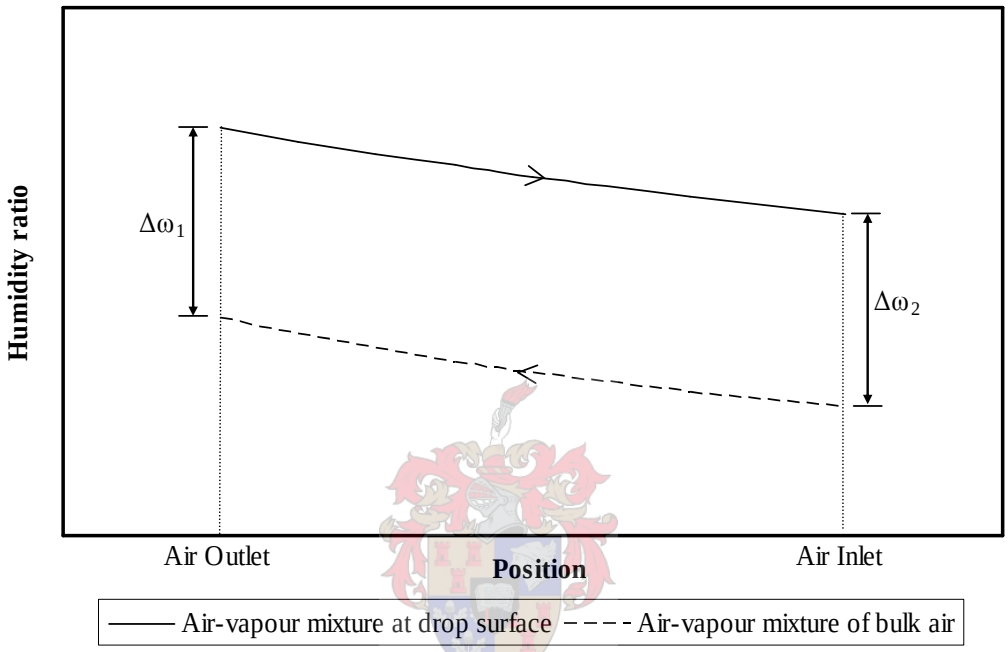

Figure 8.1: Humidity ratio as a function of position in the rain zone of a wet-cooling tower.

The problem now resembles a *counterflow heat exchanger*, thus the *log mean humidity ratio difference* can be used to determine the integral of the humidity ratio difference with respect to differential area.

$$\Delta\omega_{lm} = \frac{\Delta\omega_2 - \Delta\omega_1}{\ln\left(\frac{\Delta\omega_2}{\Delta\omega_1}\right)} \tag{8.5}$$

Thus essentially Equation (8.4) now becomes,

$$\frac{\bar{h}_d A}{m_w} = \frac{m_{evap}}{m_w \Delta\omega_{lm}} \tag{8.6}$$

FLUENT 6.2.16 can report an area-weighted-average mass fraction of a species for a pre-defined plane in the flow domain, thus the mass fraction of water in the air can be determined at the tower inlet and outlet. These can be converted to humidity ratios of the air, ω_a. The humidity ratio of saturated air at the drop surface is determined using the water drop temperature. The inlet temperature of the water, for the simulations presented here, is constant. The temperature of the water at the exit of the domain is calculated using the temperature of the drops on the exit plane and a mass flow averaging technique, Equation 5.7.

The integral of the humidity ratio difference with respect to differential area can also be approximated using the average value of the humidity ratio difference at the inlet and the outlet of the flow domain, given by,

$$\Delta\omega = \frac{\Delta\omega_1 + \Delta\omega_2}{2} \tag{8.7}$$

The results of the three different methods to determine the Merkel number for simulation *1* conditions are presented in Figure 8.2.

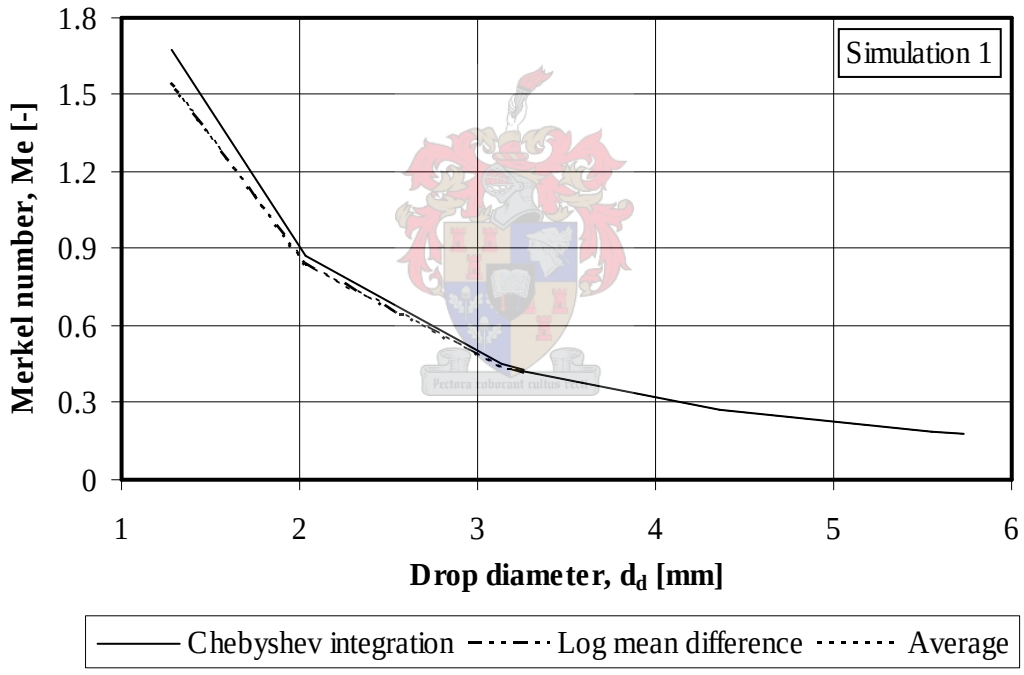

Figure 8.2: Merkel number as a function of monodisperse drop diameter for a circular wet-cooling tower flow domain.

The deviation is in the order of *0%* for $d_d > 3mm$ with a maximum deviation between the three methods of approximately *8%* at $d_d = 1.284mm$. The figure shows that results for the log mean difference and the average methods are virtually identical.

Since Chebyshev is used to determine cooling tower performance and the difference between the different methods is small, this method is used to determine the Merkel number.

For circular wet-cooling towers De Villiers and Kröger [1998DE1] propose the following correlation for the rain zone Merkel number,

$$\begin{aligned}\frac{h_d A}{m_w} &= 12\left(\frac{D}{v_i d_d}\right)\left(\frac{H_i}{d_d}\right)\left(\frac{p_a}{R_v T_a}\Big/\rho_w\right) Sc^{0.33}\, ln\left(\frac{\omega_s + 0.622}{\omega + 0.622}\right)\Big/(\omega_s - \omega) \\ &\times[0.90757 a_\rho \rho_a - 30341.04 a_\mu \mu_a - 0.37564 + 4.04016 \\ &\times[\left(0.55 + 41.7215\left(a_L d_d\right)^{0.80043}\right)\left(0.713 + 3.741\left(a_L H_i\right)^{-1.23456}\right) \\ &\times\left(3.11 exp\left(0.15 a_v v_i\right) - 3.13\right) exp[\left(5.3759 exp\left(-0.2092 a_L H_i\right)\right) \\ &\times ln\left(0.3719 exp\left(0.003811 a_L r_i\right) + 0.55\right)]]]\end{aligned} \tag{8.8}$$

and for a counterflow domain, is given as,

$$\begin{aligned}\frac{h_d A}{m_w} &= 3.6\left(\frac{D}{v_i d_d}\right)\left(\frac{H_i}{d_d}\right)\left(\frac{p_a}{R_v T_a}\Big/\rho_w\right) Sc^{0.33}\, ln\left(\frac{\omega_s + 0.622}{\omega + 0.622}\right)\Big/(\omega_s - \omega) \\ &\times[5.01134 a_\rho \rho_a - 192121.7 a_\mu \mu_a - 2.57724 + 23.61842 \\ &\times\left(0.2539\left(0.15 a_v v_i\right)^{1.67} + 0.18\right)\left(0.83667\left(a_L H_i\right)^{-0.5299} + 0.42\right) \\ &\times\left(43.0696\left(a_L d_d\right)^{0.7947} + 0.52\right)]\end{aligned} \tag{8.9}$$

The coefficients and ranges of application are the same as in the case of the rain zone loss coefficients, Equations (7.7) and (7.8).

The CFD results are used to validate Equations (8.8) and (8.9). Following a similar methodology to the one employed for the rain zone loss coefficient, the Merkel number is obtained for different monodisperse drop distributions using CFD and De Villiers and Kröger [1998DE1] and compared to the reference values, determined for a polydisperse drop distribution. Thus the difference in the Merkel number is evaluated by,

$$\Delta Me = Me_{mono} - Me_{poly} \tag{8.10}$$

8.3 Results

Graphical contour and drop trajectory plots for a circular wet-cooling tower flow field can be seen in Figures 8.3 and 8.4. The figures are results of distribution *B* under the test conditions of simulation *1*.

Figure 8.3 shows the contours of the relative humidity inside a circular wet-cooling tower. The relative humidity increases radially in the direction from the tower inlet to the tower axis. The high relative humidity at the tower axis is due to the flow recirculation zone that is present here.

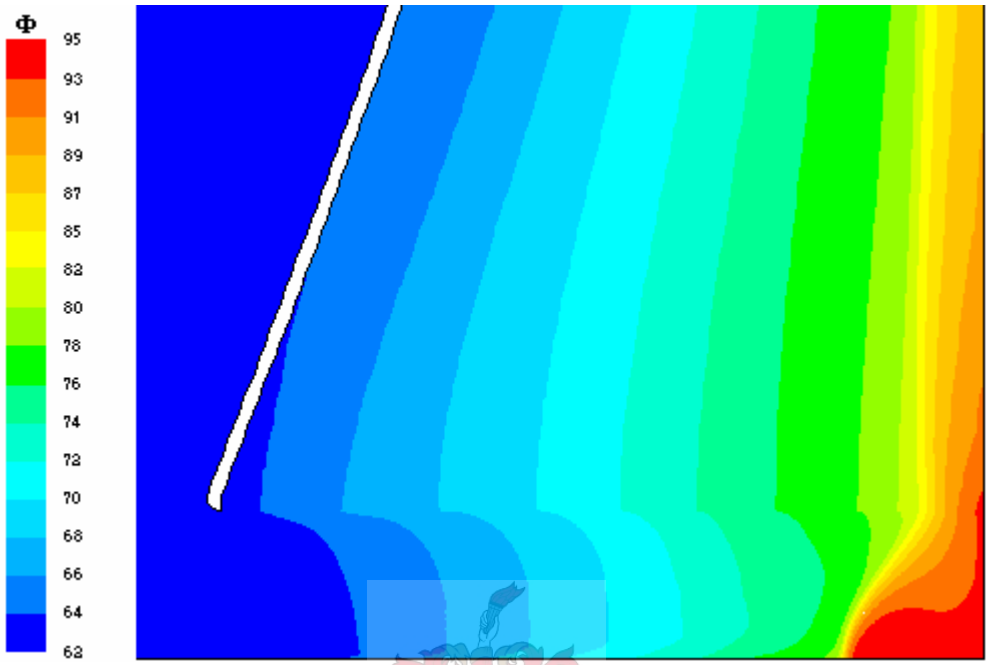

Figure 8.3: Contour plot of the relative humidity (%) inside a circular wet-cooling tower.

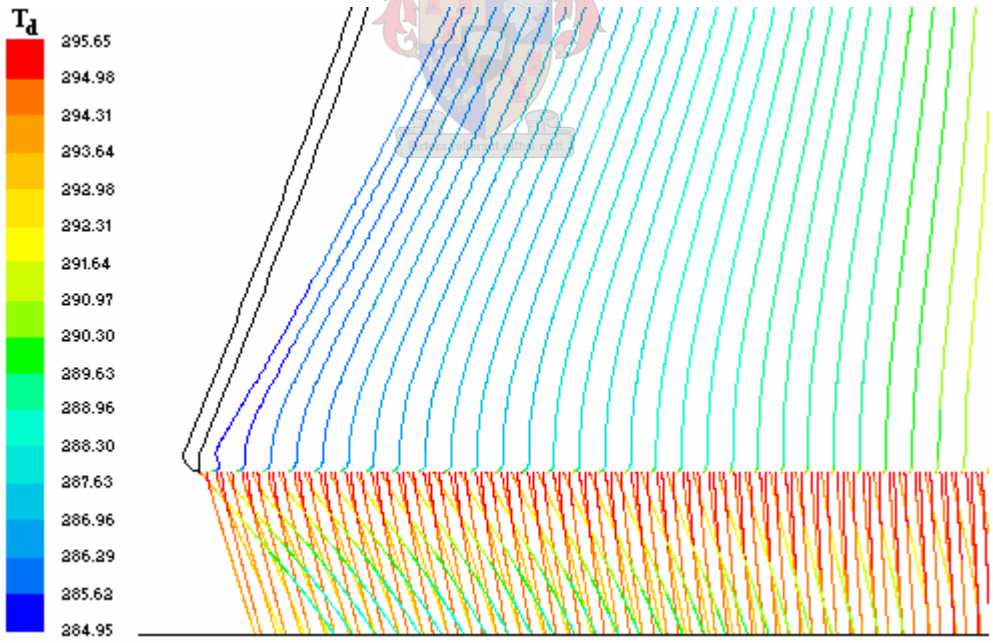

Figure 8.4: Drop trajectory plot for a circular wet-cooling tower showing drop temperature.

Figure 8.4 shows how the drop temperature changes along the drops' trajectories. Figure 8.4 is a presentation plot, the inclined trajectories are those of the smaller drops. The smaller drops' trajectories and temperature change are affected more by the air flow. These trajectories show that the temperature of some of the smaller drops come close to reaching wet bulb temperature. For the larger drops, it can be seen that they do not cool down much and that their trajectories are hardly affected by the air flow. The effect of position along the radius of the circular wet-cooling tower on the drop trajectory and drop temperature can be seen.

8.3.1 Circular Cooling Tower Domain

Figure 8.5 presents the Merkel number results obtained for different monodisperse drop distributions in a circular wet-cooling tower.

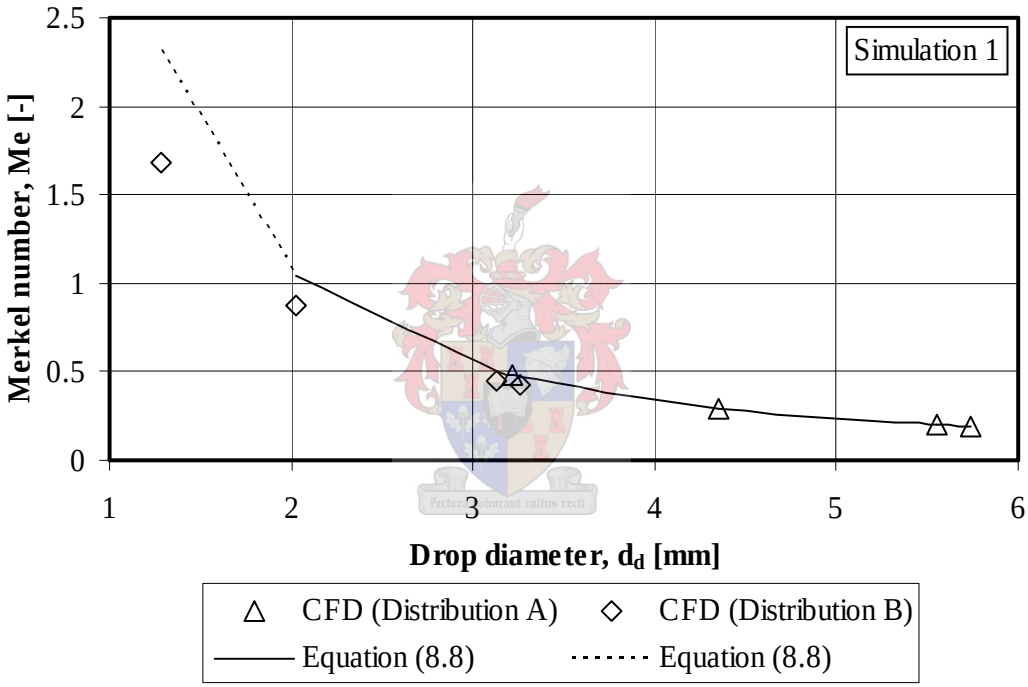

Figure 8.5: Merkel number as a function of drop diameter for a circular wet-cooling tower.

The figure depicts the results of the representative drop diameters for distributions *A* and *B*, refer to Section 6.3.2, subjected to the conditions of *simulation 1*. The two methods correspond well within the valid diameter range of Equation (8.8). Outside of the range the deviation is in the order of *30%*.

In subsequent figures in this section, the diameters are given from left-to-right as: d_{10} *(average);* d_{30} *(mean volume);* d_{41} *(Pierce)* and d_{32} *(Sauter mean).* The d_{41} diameter, defined in the previous chapter, is included in all the analyses concerning the Merkel number.

Figure 8.6 and 8.7 are applicable to distributions *A* and *B* respectively. The figures show which monodisperse drop diameter best predicts the Merkel number of a polydisperse drop distribution. Each figure is accompanied by a table that presents the average absolute of the difference between the Merkel numbers of monodisperse drop diameters and the reference polydisperse Merkel number, *ΔMe*.

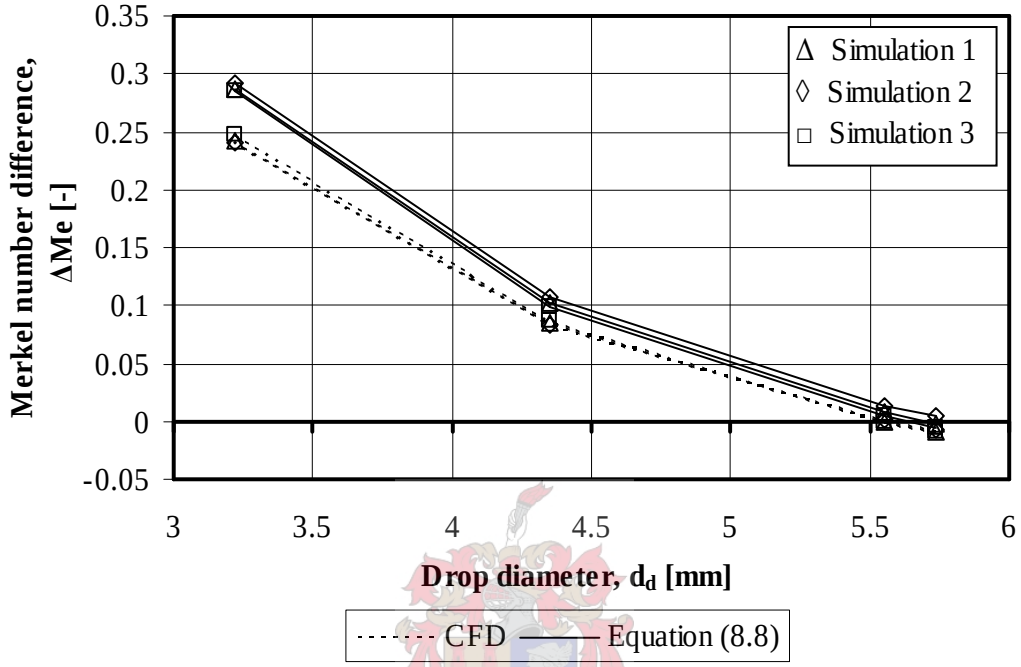

Figure 8.6: Merkel number difference as a function of monodisperse drop diameter for distribution *A*.

Table 8.1 gives an average absolute of the Merkel number difference, *ΔMe*.

Table 8.1: Average absolute of *ΔMe* for the analysis of distribution *A*.

	d_{10} = 3.219mm [%]	d_{30} = 4.354mm [%]	d_{41} = 5.553mm [%]	d_{32} = 5.734mm [%]
CFD	129	45	0	4
Equation (8.8)	152	54	5	2

It can be seen that the smallest *ΔMe* values are obtained for the *Pierce* and *Sauter mean* diameters. CFD, generally presents smaller *ΔMe* values than the De Villiers and Kröger [1998DE1] method. The discrepancy between the respective methods is small due to their close correspondence in Figure 8.5 for the respective diameter range.

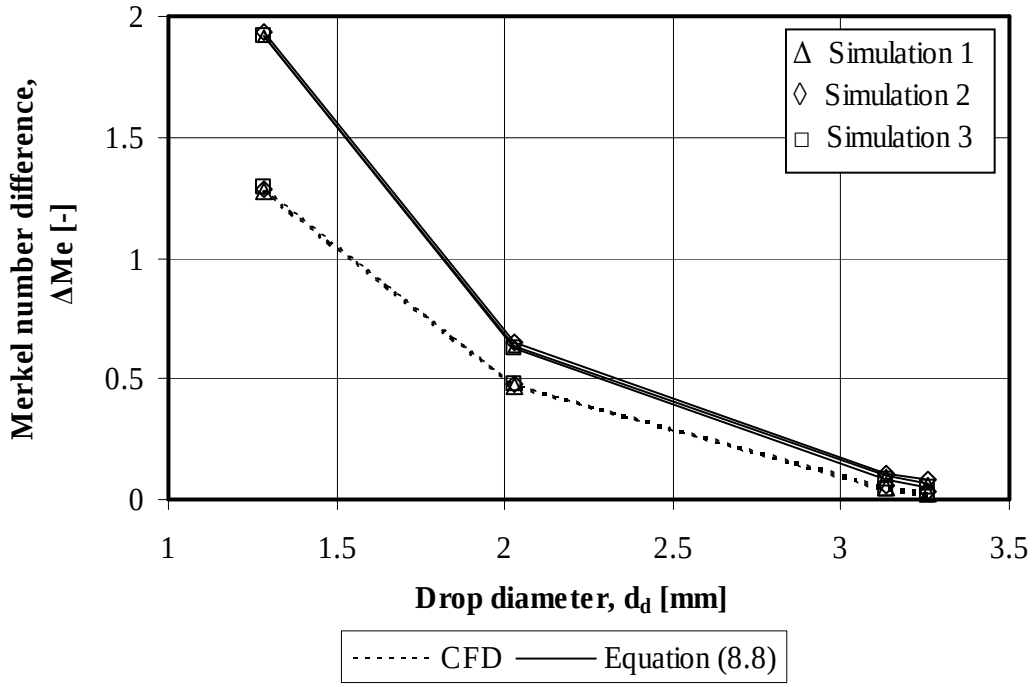

Figure 8.7: Merkel number difference as a function of monodisperse drop diameter for distribution *B*.

Table 8.2 gives an average absolute of the Merkel number difference, *ΔMe*.

Table 8.2: Average absolute of *ΔMe* for the analysis of distribution *B*.

	d_{10} = 1.284mm [%]	d_{30} = 2.029mm [%]	d_{41} = 3.131mm [%]	d_{32} = 3.256mm [%]
CFD	318	117	12	6
Equation (8.8)	477	158	24	16

It can be seen that the *Pierce* and *Sauter mean* diameters present the smallest *ΔMe* values for both methods. CFD, consistently presents smaller *ΔMe* values than the De Villiers and Kröger [1998DE1] method. Both CFD and De Villiers and Kröger [1998DE1] show clear discrepancy outside the valid diameter range for Equation (8.8).

Another point of interest in wet-cooling tower design is the amount of water that is evaporated, as this determines the amount of make-up water needed. Although the amount of water that is evaporated is included in the determination of the transfer coefficient, the author feels that it is an essential test criterion for the polydisperse/monodisperse hypothesis. The same methodology for the determination of the deviation is adopted for the evaporated mass analysis, the results for both polydisperse drop distributions are presented below on one graph for the first test condition, simulation *1*.

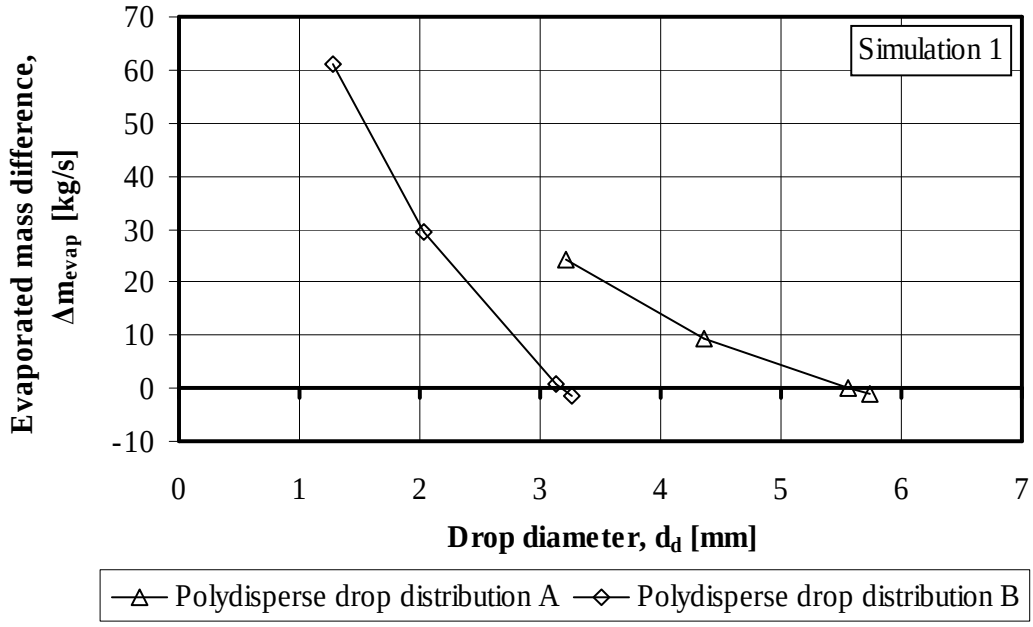

Figure 8.8: Evaporated mass difference as a function of monodisperse drop diameter for distributions *A* and *B*.

For both distributions the *Sauter mean* and *Pierce* diameters present the smallest difference. Both graphs show that for a smaller diameter, more mass is evaporated.

8.3.2 Counterflow Domain

Due to the fact that the presentation procedure of the results is similar to the previous section, only figures and tables will be given with explanations where necessary.

Figure 8.9 presents the results of the representative drop diameters for both polydisperse drop distributions subjected to the conditions of simulation *1*. The two methods correspond well within the valid diameter range given by De Villiers and Kröger [1998DE1]. Outside the diameter range, the two methods deviate by up to *30%*. The curves are very similar to those for the circular wet-cooling tower however, for this instance CFD presents higher values for the Merkel number of the smaller diameters.

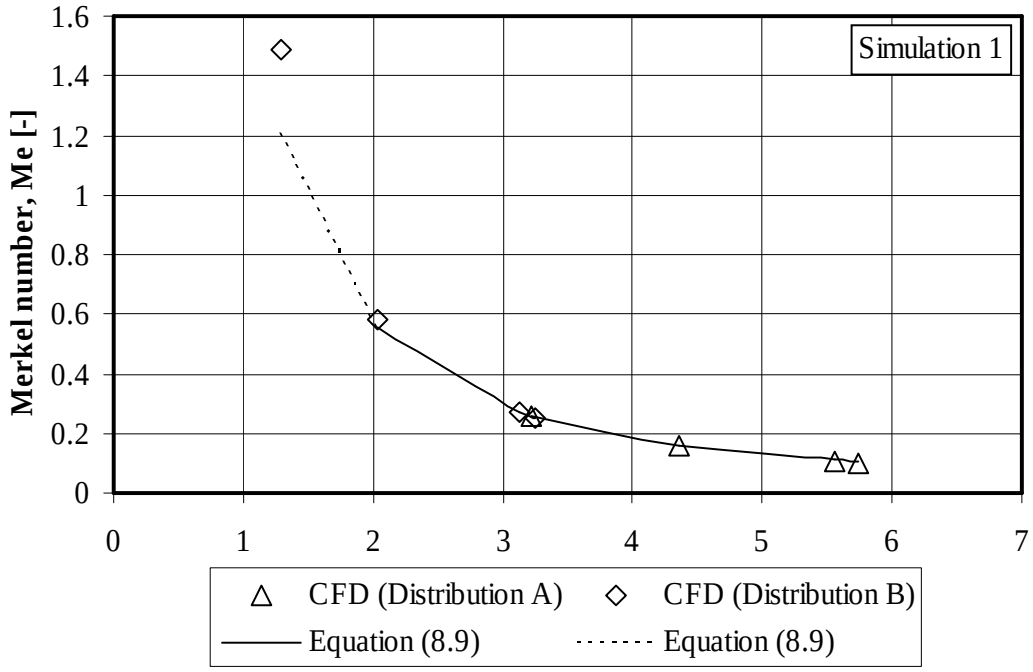

Figure 8.9: Merkel number as a function of monodisperse drop diameter for a counterflow domain.

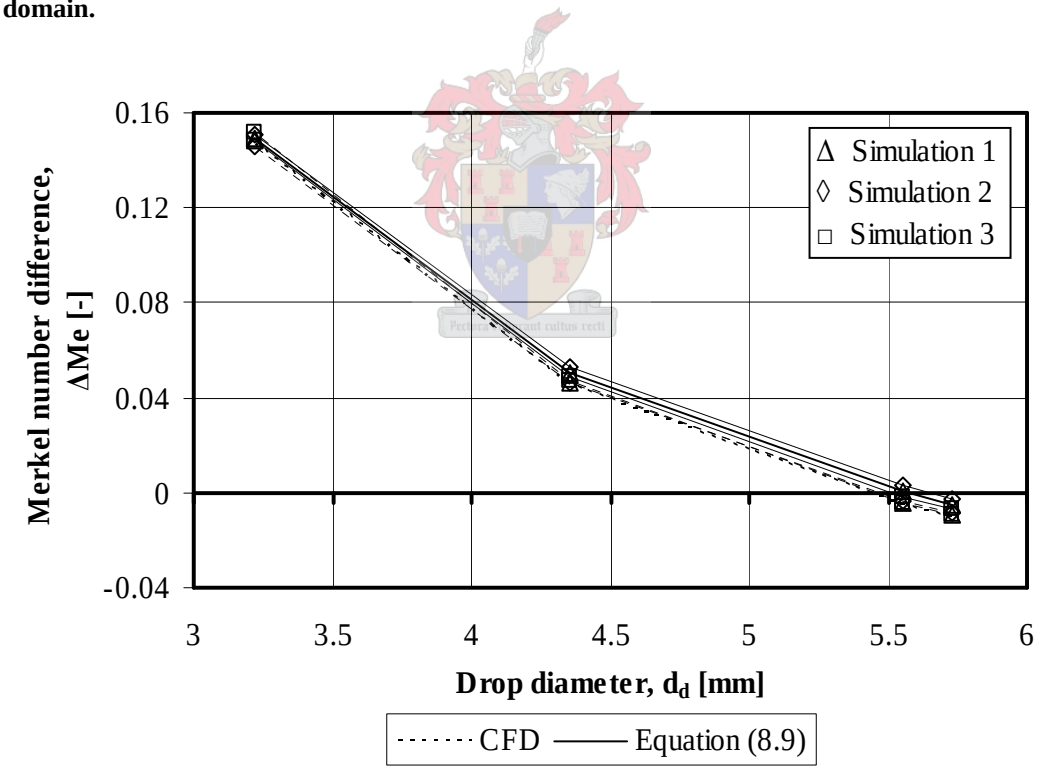

Figure 8.10: Merkel number difference as a function of monodisperse drop diameter for distribution *A*.

Table 8.3: Average absolute of *ΔMe* for the analysis of distribution *A*.

	d_{10} = 3.219mm [%]	d_{30} = 4.354mm [%]	d_{41} = 5.553mm [%]	d_{32} = 5.734mm [%]
CFD	136	42	4	8
Equation (8.9)	137	46	1	4

Table 8.3 and Figure 8.10 show that the smallest *ΔMe* is obtained for the *Pierce* and *Sauter mean* diameters.

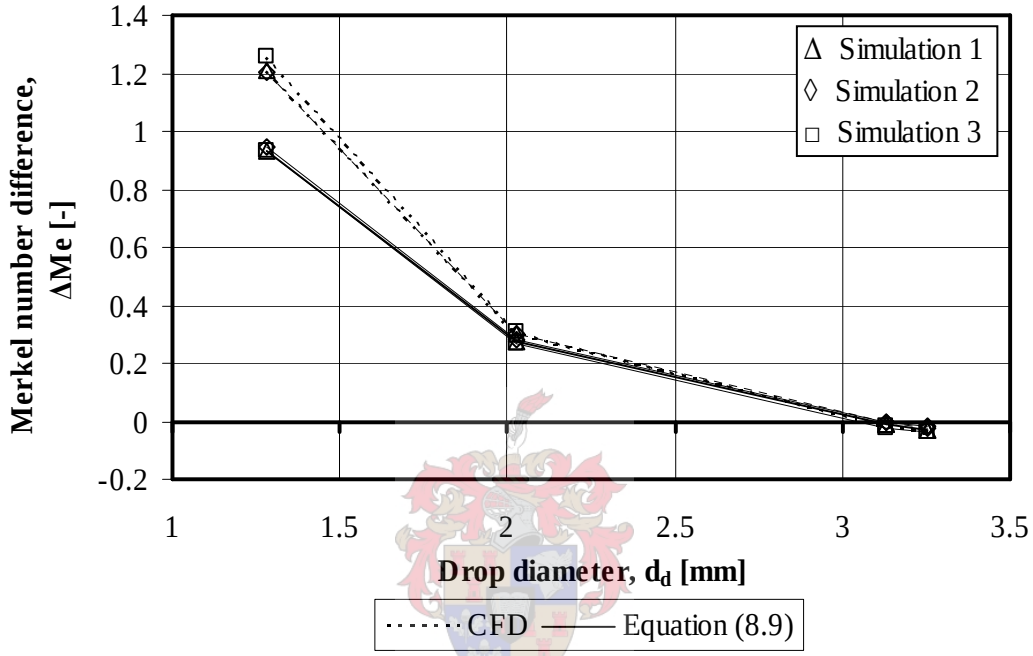

Figure 8.11: Merkel number difference as a function of monodisperse drop diameter for distribution *B*.

Table 8.4: Average absolute of *ΔMe* for the analysis of distribution *B*.

	d_{10} = 1.284mm [%]	d_{30} = 2.029mm [%]	d_{41} = 3.131mm [%]	d_{32} = 3.256mm [%]
CFD	435	109	4	10
Equation (8.9)	334	97	4	10

Table 8.4 and Figure 8.11 show that the smallest *ΔMe* is obtained for the *Pierce* and *Sauter mean* diameters.

Summary

This chapter set out to analyse the rain zone in a circular wet-cooling tower and a counterflow domain with regards to the Merkel number.

A new approximation technique for the Merkel number was developed. The technique relies on the *log mean difference technique*. The Merkel number values presented were compared to the values obtained from the Chebyshev integration technique. The methods compared well, the deviation is in the order of *0%* for $d_d > 3mm$ with a maximum deviation between the three methods of approximately *8%* at $d_d = 1.284mm$.

Employing the correlations given by De Villiers and Kröger [1998DE1] and CFD, the Merkel numbers were determined for different monodisperse drop distributions. The values were compared and found to be in good agreement, in the order of *10%* and *2%* for the circular cooling tower and counterflow domains respectively. Thus the method of De Villiers and Kröger [1998DE1] for determining the transfer coefficient of a circular wet-cooling tower and a counterflow domain was validated.

The values of the Merkel number for both methods, employing the different representative drop diameters were then compared to the reference value determined by using the polydisperse drop distribution. It was found that no single representative drop diameter modelled the polydisperse drop distribution precisely, concerning the Merkel number.

The new representative drop diameter was evaluated. For all the analyses presented here the *Pierce* and the *Sauter mean* diameters were found to model the polydisperse drop distribution the best.

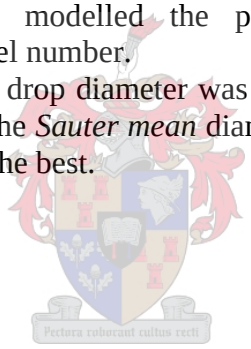

CHAPTER

9

Conclusions and Recommendations

9.1 Conclusions

In this thesis the velocity, path length, cooling and change in diameter of a drop falling through air were modelled using analytical and numerical solution techniques. According to literature, internal circulation and drop oscillation have a negligible effect on the drag experienced by a drop, but the effect of drop deformation is significant. A simplified new correlation is proposed for the drag coefficient of deformable drops, which proves to be less computationally expensive deviating from experimental data by less than *10%*.

Drop deformation results in a lower absolute terminal velocity than a sphere. The pressure drop over a domain was found to be strongly dependent on the drag force of the drops in the domain as well as the total number of drops. It was found that drop deformation increased the pressure drop over a domain significantly, the value of which depends on the applicable domain. The effect of the increased drag coefficient on the cooling of a drop, due to drop deformation, was found to be negligible. Drop deformation therefore needs to be included in the drop drag equation in order to create a model that can predict the loss coefficient accurately. Furthermore, it was found that the cooling of a drop was enhanced significantly by the effects of acceleration.

An increase in counterflow air velocity reduces the absolute terminal velocity of a drop resulting in a longer contact period for a certain fall height, and higher initial heat and mass transfer coefficients. This results in increased cooling, at the expense of a higher pressure drop.

Typically the thermal transient time is longer than the transient time for the velocity of a drop. In conventional cooling towers, the majority of the drops never reach their terminal velocity or cooling limit. Therefore the acceleration period of a drop is most important, thus the model of Lowe and Christie [1961LO1] should be revised. The data of Lowe and Christie [1961LO1] is applicable to small drops only and the drops fall at their terminal velocity.

For specific conditions typically encountered in cooling towers, the diameter of any drop changes by less than *2%* before reaching its cooling limit. Since only the smaller drops tend to approach their cooling limit the change in the drops' diameter can be neglected for the determination of its cooling, however it is needed to determine the mass that is evaporated. The different solution techniques showed that the assumption of constant thermophysical properties of

the drop is acceptable. Figure 3.4 shows that smaller drops require a shorter domain to attain the same cooling as larger drops, resulting in lower pumping costs.

An experimental test facility was designed and built to determine *inter alia* the drop size distribution below different types of fill and the pressure drop over a domain of drops. The facility can be extended to facilitate the investigation of many areas of interest in a cooling tower.

From the experimental drop distribution data it was found that the retained mass distributions, for a specific fill type, remained relatively constant for different water and air mass velocities, which resulted in negligible variation in the representative diameters. The variations in the retained mass distributions remained within the uncertainty limits.

CFD models were generated together with a test procedure for the analysis of a circular cooling tower and counterflow domains. Using these models, the Rosin-Rammler distribution function was found to be inadequate for predicting performance parameters of cooling tower rain zones. Thus it was necessary to input the discrete drop distribution data into CFD.

CFD showed satisfactory comparison with experimental correlations for the inlet loss coefficient of circular cooling towers which instilled confidence.

The correlations of De Villiers and Kröger [1998DE1] for the loss coefficient and Merkel number of a counterflow and circular wet-cooling tower are validated using CFD and a monodisperse drop distribution. The results compared satisfactorily for the prescribed diameter range, with the largest deviation between the methods being in the order of *10%*. Outside this range the results differed considerably.

The *Sauter mean* and d_{41}*(Pierce)* representative diameters were found to be the equivalent monodisperse diameters most suitable for approximating the Merkel number of a polydisperse drop distribution. For the approximation of the loss coefficient; the *mean volume* diameter was the equivalent monodisperse diameter for the polydisperse drop distribution with the larger mean diameter, and the *Sauter mean* and *Pierce* were the equivalent monodisperse diameters for the polydisperse drop distribution with the smaller mean diameter. This presents a shift in equivalent monodisperse diameter, which was not found for the Merkel number. These findings are in agreement with Alkidas [1981AL1], Aggarwal [1988AG1] and Hollands and Goel [1976HO1].

Similar results were obtained with both the *Sauter mean* and the *Pierce* diameters, however the *Pierce* diameter generally appears to be more conservative. Furthermore, the *Pierce* diameter lies between the *Sauter mean* and the *mean volume* diameters. Therefore, with the shift in equivalent monodisperse drop diameter for the loss coefficient, it may generally give better results than the *Sauter mean* diameter, but not necessarily the *mean volume* diameter. It was found that the deviation between the monodisperse and polydisperse Merkel numbers was never larger than *5%* of the tower's overall Merkel number, for both the *Sauter mean* and *Pierce* diameters. A similar result was found for the loss coefficient, using the *Sauter mean* and *Pierce* diameters. Therefore, for the use of the one-dimensional model of De Villiers and Kröger [1998KR1] it is

recommended to use the *Sauter mean* and *Pierce* diameters when determining the performance characteristics of the rain zone.

The formulation of an ideal wet-cooling tower rain zone is given, this rain zone may never be achieved but may serve as a milestone in the journey of improving these systems.

Hollands [1974HO1] states that a monodisperse drop distribution with a diameter of *1 – 2mm* is desirable for a spray cooling tower. Ideally a rain zone should consist of a monodisperse drop distribution of which the drop diameter can automatically be varied, so as to always operate at maximum effectiveness with minimum evaporation losses.

The question of which drop diameter is desirable, presents two possible solutions. For a small drop diameter, a shorter rain zone is needed to reach the cooling limit, however with small drops the interfacial area between the drops and the air is large, resulting in high evaporation losses. For larger drops, the evaporation losses are less, however a longer rain zone is needed to reach the cooling limit. The height of the rain zone can be reduced by creating a counterflow rain zone with a high counterflow air velocity, thereby retarding the large drops, which ultimately means that a shorter rain zone is needed to reach the cooling limit.

Although industry should be heading towards these ideal rain zones, there should still be further investigation and improvement to existing models in the academic environment. This thesis has shown that the cooling, velocity, path length and the change in diameter of a drop can be determined analytically. Therefore a complete two-dimensional mathematical model should be possible that can predict the performance of a cooling tower. By using similar techniques to Fisenko et al. [2004FI1] this model can incorporate a polydisperse drop distribution.

The development of CFD makes it an evermore viable tool for the analysis of cooling tower performance. CFD can model turbulence using different available models and is able to capture certain flow effects that exist in a cooling tower that are ignored in mathematical models. CFD is also able to model polydisperse drop distributions.

9.2 Recommendations

The effect of drop collision, agglomeration and coalescence on the performance of the rain zone should be investigated. Literature shows that circulation and oscillations have no real effect on the terminal velocity of a drop. Is this the case for the heat and mass transfer? This thesis illustrated that the acceleration period of a drop is very important, however very little literature is available on the effects of acceleration on the heat and mass transfer.

With CFD it is possible to model a realistic flow field, this can be used to analyse the assumption of a simplified flow field, found in many mathematical models of the cooling tower. It was found that the rain zone has an effect on the

velocity distribution above the fill, CFD can be used to analyse this. The effect of drop diameter on the distribution can also easily be analysed using CFD. It is also recommended that investigation be done on the most viable turbulence model to be used in CFD models of a cooling tower.

References

[1925ME1] Merkel, F., Verdunstungskühlung, VDI-Zeitschrift, Vol. 70, No. 70, pp. 123 – 128, January 1925.

[1938FR1] Frössling, N., Über die Verdunstung Fallender Tropfen, Gerlands Beitrage Zur Geophysik, Vol. 52, pp. 170 – 216, 1938.

[1940LA1] Lapple, C.E. and Shepherd, C.B., Calculation of Particle Trajectories. Ind. Eng. Chem., Vol. 32, No.5, pp. 605-617 1940.

[1949GU1] Gunn, R. and Kinzer, G.D., The Terminal Velocity of Fall for Water Droplets In Stagnant Air, Journal of Meteorology, Vol. 6, pp. 243 – 248, August 1949.

[1951SN1] Snyder, R.W., The Cooling of a Freely Falling Water-Drop, IMechE, ASME Proceedings of the General Discussion on Heat Transfer, pp. 160 – 166, September 1951.

[1952RA1] Ranz, W.E. and Marshall Jr. W.R., Evaporation from Drops, Part I, Chemical Engineering Progress, Vol. 48, No. 3, pp. 141 – 146, March 1952.

[1954HS1] Hsu, N., Sato, K. and Sage, B., Material Transfer in Turbulent Gas Stream, Industrial and Engineering Chemistry, Vol. 46, pp. 870 – 876, 1954.

[1961LO1] Lowe, H.J. and Christie, D.G., Heat Transfer and Pressure Drop Data on Cooling Tower Packings and Model Studies of the Resistance of Natural Draft Towers to Airflow, Proc. of the Int. Heat Transfer Conf. Boulder, Colorado, 1961.

[1961RI1] Rish, R.F., The Design of a Natural Draught Cooling Tower, Proceedings of the 2nd International Heat Transfer Conference, Boulder, Colorado, USA, 1961.

[1969BE1] Beard, K.V. and Pruppacher, H.R., A Determination of the Terminal Velocity and Drag of Small Water Drops by Means of a Wind Tunnel, Journal of Atmospheric Sciences, Vol. 26, pp. 1066 – 1072, September 1969.

[1972LE1] LeClair, B.P., Hamielec, A.E., Pruppacher, H.R. and Wall, W.D., A Theoretical Study of the Internal Circulation in Water Drops Falling at Terminal Velocity in Air, Journal of the Atmospheric Sciences, Vol. 29, pp. 728 – 740, 1972.

[1972MO1] Morsi, S.A. and Alexander, A.J., An Investigation of Particle Trajectories in Two-Phase Flow Systems, Journal of Fluid Mechanics, Vol. 55, No. 2, pp. 193 – 208, 26 September 1972.

[1972PO1] Poppe, M., Wärme und Stoffübertragung bei der Verdunstungskühlung in Gegen-und Kreuzstrom, Doctoral thesis, Technische Universität, Hannover, 1972.

[1974HO1] Hollands, K.G.T., An Analysis of a Counterflow Spray Cooling Tower, International Journal of Heat and Mass Transfer, Vol. 17, pp. 1227 – 1239, 1974.

[1976HO1] Hollands, K.G.T. and Goel, K.C., Mean Diameters in Parallel-Flow and Counter-Flow Aerosol Systems, ASME Journal of Heat Transfer, pp. 297 – 302, May 1976.

[1976RY1] Ryan, R.T., The Behaviour of Large, Low-Surface Tension Drops Falling at Terminal Velocity in Air, Journal of Applied Meteorology, Vol. 15, pp. 157 – 165, February 1976.

[1976YA1] Yao, S.C. and Schrock, V.E., Heat and Mass Transfer from Freely Falling Drops, ASME Journal of Heat Transfer, pp. 120 – 126, February 1976.

[1977BE1] Beard, K.V., On the Acceleration of Large Water Drops to Terminal Velocity, Journal of Applied Meteorology, Vol. 16, pp. 1068 – 1071, October 1977.

[1977CH1] Chen, K.C. and Trezek, G.J., The Effect of Heat Transfer Coefficient, Local Wet Bulb Temperature and Droplet Size Distribution Function on the Thermal Performance of Sprays, ASME Journal of Heat and Transfer, Vol. 99, pp. 381 – 385, 1977.

[1977MI1] Miura, K., Miura, T. and Ohanti, S., Heat and Mass Transfer to and from Droplets, AIChE Symposium Series, Vol. 73, No. 163, pp. 95 – 102, 1977.

[1978CL1] Clift, R., Grace, J.R. and Weber, M.E., Bubbles Drops and Particles, Academic Press Inc., New York, 1978.

[1978PR1] Pruppacher, H.R. and Klett, J.D., Microphysics of Clouds and Precipitation, D. Reidel Publishing Company, Dordrecht, Holland, 1978.

[1981AL1] Alkidas, A.C., The Influence of Size-Distribution Parameters on the Evaporation of Polydisperse Dilute Sprays, International Journal of Heat and Mass Transfer, Vol. 24, No. 12, pp. 1913 – 1923, 1981.

[1982SR1] Srikrishna, M., Sivaji, K. and Narasimhamutry, G.S.R., Mechanics of Liquid Drops in Air, The Chemical Engineering Journal, Vol. 24, pp. 27 – 34, 1982.

[1986BE1] Benton, D.J. and Rehberg, R.L., Mass Transfer and Pressure drop in Sprays Falling in a Freestream at Various Angles, Proceedings of the 5th IAHR Cooling Tower Workshop, Monterey, October 1986.

[1986TU1] Turton, R. and Levenspiel, O., A Short Note on the Drag Correlation for Spheres, Powder Technology, Vol. 47, pp. 83 – 86, 1986.

[1988AG1] Aggarwal, S.K., Ignition and Flame Propagation in Dilute Polydisperse Sprays; Importance of d_{32} and d_{20}, Journal of Propulsion, Vol. 4, No. 1, pp. 14 – 21, January – February 1988.

[1989HA1] Haider, A. and Levenspiel, A., Drag Coefficient and Terminal Velocity of Spherical and Nonspherical Particles, Powder Technology, Vol. 58, pp. 63 – 70, 1989.

[1989RE1] Renganathan, K., Turton, R. and Clark, N.N., Accelerating Motion of Geometric and Spherical Particles in a Fluid, Powder Technology, Vol. 58, pp. 279 – 284, 1989.

[1991WH1] White, F.M., Viscous Fluid Flow, McGraw-Hill, Singapore, 1991.

[1994DR1] Dreyer, A.A., Modelling of Cooling Tower Splash pack, Ph.D. Thesis, University of Stellenbosch, Stellenbosch, South Africa, 1994.

[1994ER1] Erens, P.J., Mercker, A.A. and Dreyer, A.A., Evaporation from Accelerating Droplets, Proceedings of the 10th Heat Transfer Conference, Brighton, pp. 305 – 310, 1994.

[1994TE1] Terblanche, J.E. and Kröger, D.G., Experimental Evaluation of the Aerodynamic Inlet Losses in Cooling Towers, South African Institute of Mechanical Engineers R&D Journal, Vol. 10, No. 2, pp. 41 – 44, 1994.

[1997DE1] De Villiers, E. and Kröger, D.G., Analysis of Heat, Mass and Momentum Transfer in the Rain Zone of Counterflow Cooling Towers, Proceedings of the 1997 IJPGC, Vol. 2, PWR-Vol. 32, pp. 141 – 149, Denver, November 1997.

[1997FE1] Ferreira, J.M. and Chhabra, R.P., Accelerating Motion of a Vertically Falling Sphere in Incompressible Newtonian Media: an Analytical Solution, Powder technology, Vol. 97, pp. 6 – 15, 1998.

[1998KR1] Kröger, D.G., Air-Cooled Heat Exchangers and Cooling Towers, Begell House, New York, 1998.

[1999MI1] Mills, A.F., Heat Transfer, Prentice Hall, Upper Saddle River, NJ, USA, 1999.

[1999ST1] Stewart, J., Calculus, Brooks/Cole Publishing Company, Pacific Grove, USA, 1999.

[1999WH1] White, F.M., Fluid Mechanics, McGraw-Hill, Singapore, 1999.

[2000EV1] Evans, G., Blackledge, J. and Yardley, P., Numerical Methods for Partial Differential Equations, Springer-Verlag, London, Great Britain, 2000.

[2002CE1] Cengel, S.A. and Boles, M.A., Thermodynamics: an Engineering Approach, McGraw-Hill, New York, 2002.

[2002IN1] Incropera, F.P. and De Witt, D.P., Fundamentals of Heat and Mass Transfer, John Wiley and Sons, New York, 2002.

[2003FL1] FLUENT 6.2.16, Documentation, Fluent Inc., Lebanon, USA, 2003

[2004FI1] Fisenko, S.P., Brin, A.A. and Petruchik, A.I., Evaporative Cooling of Water in a Mechanical Draft Cooling Tower, International Journal of Heat and Mass Transfer, Vol. 47, pp.165 – 177, 2004.

[2005SN1] Snyman, H., Automation of a Data Acquisition System for a Cooling Tower Test Facility, B.Eng final year project, University of Stellenbosch, Stellenbosch, South Africa, 2005.

[2005TE1] Terblanche, R., Optimization of a Measurement Technique for Evaluation of Drop Size Distribution in a Wet Cooling Tower Test Rig, B.Eng final year project, University of Stellenbosch, Stellenbosch, South Africa, 2005.

[2006VI1] Viljoen, D.J., Evaluation and Performance Prediction of Cooling Tower Spray Zones, MSc.Eng. Thesis, University of Stellenbosch, Stellenbosch, South Africa, 2006.

[2006WI1] Williamson, N., Behnia, M. and Armfield, S., Numerical Simulation of Heat and Mass Transfer in a Natural Draft Wet Cooling Tower, Proceedings of the 15th Australasian Fluid Mechanics Conference, 13 – 17 December 2004.

APPENDIX

A

Thermophysical Properties of Fluids

All thermophysical properties are taken from Kröger [1998KR1].

A.1 Thermophysical properties of dry air from 220K to 380K at atmospheric pressure 101325Pa

Density:

$$\rho_a = \frac{p_a}{R_a T} \text{ kg/m}^3 \tag{A.1}$$

Specific heat:

$$c_{pa} = 1.045356\times10^{3} - 3.161783\times10^{-1}T + 7.083814\times10^{-4}T^{2} - 2.705209\times10^{-7}T^{3} \text{ J/kgK} \tag{A.2}$$

Dynamic viscosity:

$$\mu_a = 2.287973\times10^{-6} + 6.259793\times10^{-8}T - 3.131956\times10^{-11}T^{2} + 8.15038\times10^{-15}T^{3} \text{ kg/sm} \tag{A.3}$$

Thermal conductivity:

$$k_a = -4.937787\times10^{-4} + 1.018087\times10^{-4}T - 4.627937\times10^{-8}T^{2} + 1.250603\times10^{-11}T^{3} \text{ W/mK} \tag{A.4}$$

A.2 Thermophysical properties of saturated water vapour from 273.15K to 380K

Vapour pressure:

$$p_v = 10^z \text{ N/m}^2$$
$$z = 10.79586\left(1-273.16/T\right)+5.02808\,log_{10}\left(273.16/T\right)$$
$$+1.50474\times10^{-4}\left(1-10^{-8.29692\left((T/273.16)-1\right)}\right)$$
$$+4.2873\times10^{-4}\left(10^{4.76955(1-273.16/T)}-1\right)+2.786118312 \quad \text{(A.5)}$$

Specific heat:

$$c_{pv} = 1.3605\times10^3 + 2.31334T - 2.46784\times10^{-10}T^5 + 5.91332\times10^{-13}T^6 \text{ J/kgK} \quad \text{(A.6)}$$

Humidity ratio:

$$\omega = \frac{0.622\phi p_v}{\left(p_a - \phi p_v\right)} \quad \text{(A.7)}$$

A.3 Thermophysical properties of mixtures of air and water vapour

Density:

$$\rho_{av} = \left(1+\omega\right)\left(1-\omega/\left(\omega+0.62198\right)\right)p_a/287.08T \text{ kg air-vapour/m}^3 \quad \text{(A.8)}$$

Specific heat:

$$c_{pav} = \left(c_{pa}+\omega c_{pv}\right)/\left(1+\omega\right) \text{ J/K kg air-vapour} \quad \text{(A.9)}$$

Dynamic viscosity:

$$\mu_{av} = \left(X_a\mu_a M_a^{0.5} + X_v\mu_v M_v^{0.5}\right)/\left(X_a M_a^{0.5} + X_v M_v^{0.5}\right) \text{ kg/ms} \quad \text{(A.10)}$$

where $M_a = 28.97$kg/mole, $M_v = 18.016$kg/mole, $X_a = 1/(1 + 1.608\omega)$ and $X_v = \omega/(\omega + 0.622)$

Thermal conductivity:

$$k_{av} = \left(X_a k_a M_a^{0.33} + X_v k_v M_v^{0.33} \right) \Big/ \left(X_a M_a^{0.33} + X_v M_v^{0.33} \right) \text{ W/mK} \qquad \text{(A.11)}$$

Enthalpy:

$$h_{av} = \frac{\left(c_{pa} \left(T - 273.15 \right) + \omega \left(h_{fgwo} + c_{pv} \left(T - 273.15 \right) \right) \right)}{\left(1 + \omega \right)} \text{ J/kg air-vapour} \qquad \text{(A.12)}$$

Humidity ratio:

$$\omega = \left(\frac{2501.6 - 2.3263 \left(T_{wb} - 273.15 \right)}{2501.6 + 1.8577 \left(T - 273.15 \right) - 4.184 \left(T_{wb} - 273.15 \right)} \right) \times \left(\frac{0.62509\, p_{vwb}}{p_a - 1.005\, p_{vwb}} \right) - \left(\frac{1.00416 \left(T - T_{wb} \right)}{2501.6 + 1.8577 \left(T - 273.15 \right) - 4.184 \left(T_{wb} - 273.15 \right)} \right) \qquad \text{(A.13)}$$

A.4 Thermophysical properties of saturated water liquid from 273.15K to 380K

Density:

$$\rho_w = \left(\begin{matrix} 1.49343 \times 10^{-3} - 3.7164 \times 10^{-6} T + 7.09782 \times 10^{-9} T^2 \\ -1.90321 \times 10^{-20} T^6 \end{matrix} \right)^{-1} \text{ kg/m}^3 \qquad \text{(A.14)}$$

Specific heat:

$$c_{pw} = 8.15599 \times 10^3 - 2.80627 \times 10^1 T + 5.11283 \times 10^{-2} T^2 - 2.17582 \times 10^{-13} T^6 \text{ J/kgK} \qquad \text{(A.15)}$$

Latent heat of vaporization:

$$h_{fgw} = 3.4831814 \times 10^6 - 5.8627703 \times 10^3 T + 12.139568 T^2 - 1.40290431 \times 10^{-2} T^3 \text{ J/K} \qquad \text{(A.16)}$$

APPENDIX

B

Derivation of a Drag Coefficient Correlation for Deformable Drops

FLUENT 6.2.16 provides the option to select one of five different drag laws for drops, of which only three are applicable to the work in this thesis i.e. spherical, non-spherical and the dynamic drag law. Referring to Figure 2.3 it can be seen that for large drop diameters, $d > 2mm$, a drag law that makes provision for drop deformation needs to be used. The spherical drag law is therefore not applicable. When selecting the non-spherical drag law a single value for the shape factor is required as input, which presents a problem when modelling a polydisperse drop distribution as this shape factor is then the same for all the different drop diameters. FLUENT 6.2.16 also assumes that the shape factor is constant and thus the drop does not undergo transient deformation. The dynamic drag law does however consider transient deformation and can accommodate a polydisperse drop distribution. This drag law can only be activated in conjunction with a drop break-up model and unsteady tracking.

The calculation procedure and reasoning for the derivation of a drag coefficient correlation for deformable drops is given below.

Dreyer [1994DR1] proposes a correlation that expresses the ratio of the drop and sphere drag coefficients as a function of the drop deformation, Equation (2.15). The correlation shows good comparison with the experimental results of Gunn & Kinzer [1949GU1] as shown in Figure 2.9.

$$\frac{C_D}{C_{D,sphere}} = 1 - 0.17185(1-E) + 6.692(1-E)^2 - 6.605(1-E)^3 \qquad (2.15)$$

When employing Equation (2.15) there are six calculation steps to be performed of which one is an iteration loop to determine the terminal velocity of the drop. FLUENT 6.2.16 will perform this set of calculations for each drop in the domain thereby increasing the computing time. A need therefore exists for a correlation that requires few calculation steps but that still models the transient deformation of a drop and that can be used when modelling poly-dispersed drop distributions.

The deformed drop drag coefficient, calculated using Equation (2.15), is plotted in Figure B.1 as a function of Reynolds number for different drop diameters and compared with the drag coefficient calculated using Equation (2.6) for spheres.

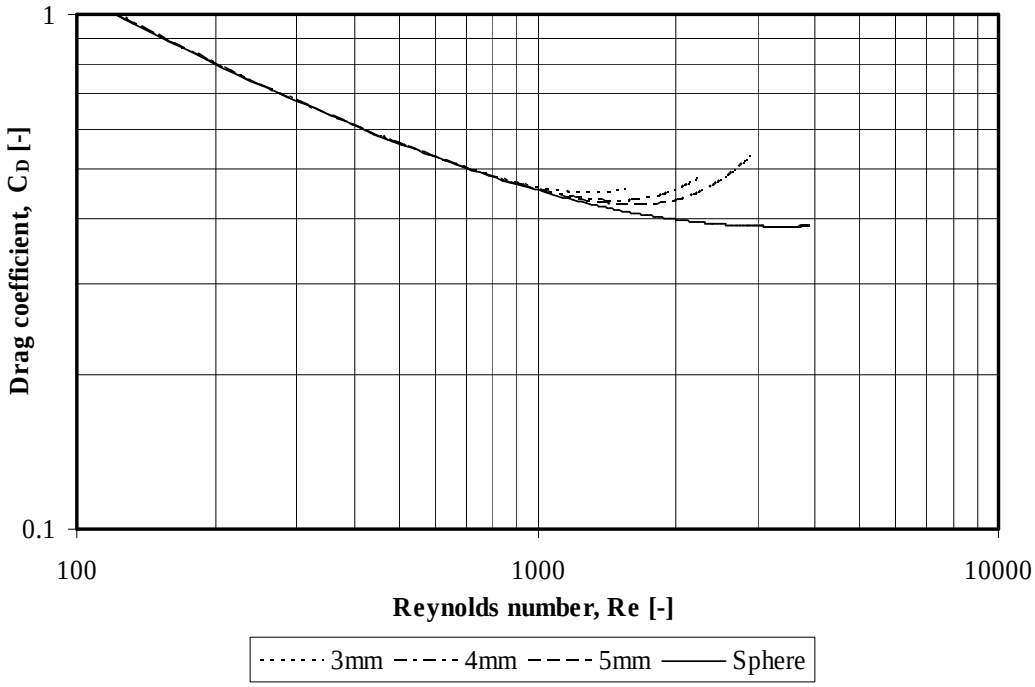

Figure B.1: Deformed drag coefficient as a function of Reynolds number.

Figure B.1 shows how the deformed drag coefficients for a number of drop diameters deviate from the standard drag curve of a sphere, they are no longer only dependent on the Reynolds number. Each drop has a unique terminal deformation value, thus resulting in its own unique drag coefficient curve. Using the terminal deformation value for a drop from Equation (2.12), a new correlation can be determined for the deformed drag coefficient, given by,

$$C_D = \frac{23.986}{Re} + \frac{4.186}{Re^{0.343}} + \left(1.28\times10^{-6} E_T^{2.017} - 1.75\times10^{-6} E_T + 7.07\times10^{-7}\right) Re^{1.831} \quad (2.16)$$

Figure B.1 shows that the deformed drag coefficients closely resemble the drag coefficient of a sphere for Reynolds numbers *Re < 1000*, and therefore the first two terms of Equation (2.16) are similar to the first two terms in Equation (2.6), the third term however differs to account for drop deformation.

Figure B.2 illustrates the difference between the drag coefficient values predicted by Equation (2.15) and Equation (2.16). Referring to Figure 2.9 the prediction error on the terminal velocity using Equation (2.16) can be seen. From the figure it is clear that the new correlation slightly over predicts the terminal velocity but within an acceptable limit of *10%*. Furthermore Equation (2.16) requires three non-iterative calculation steps.

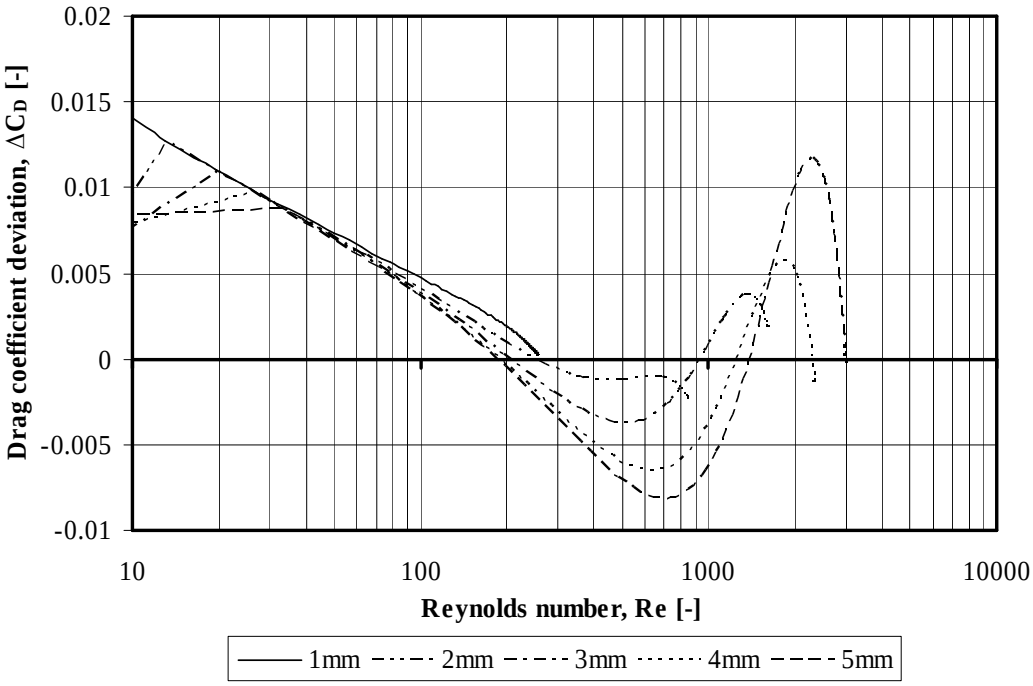

Figure B.2: Deviation between Equation (2.15) and Equation (2.16) for different diameters.

Since the drag laws available in FLUENT 6.2.16 are inadequate for the modelling of polydisperse drop distributions and large drops, Equation (2.16) is implemented by means of a user-defined-function (UDF), written in *C* code.

APPENDIX

C

An Analytical Solution for the Accelerating Motion of a Vertically Free-Falling Sphere in an Incompressible Newtonian Fluid

A spherical body free-falling vertically in an incompressible Newtonian fluid will be decelerated by frictional and form drag and will be accelerated by gravity. The net force on the spherical object will be the vectorial sum of the form drag and the body forces. The drag force will always depend on the relative velocity of the spherical body to the fluid.

To describe the accelerating motion of a spherical body, it is assumed that a sphere of diameter d_s, mass M_s and density ρ_s falls freely in an incompressible Newtonian fluid of density ρ_a. The velocity of the sphere can be represented by v_s at any instant t. Let g represent gravitational acceleration.

Renganathan and Turton [1989RE1] noted that when the sphere density was much larger than the fluid density, the Basset force becomes negligible. Where the Basset force, also known as the history term, is the force associated with past movements of the body. The added mass force is a result of the fluid surrounding the body being accelerated. It has a tendency to keep the body from being accelerated in any direction. Neither of these terms is included in the derivation that follows.

The equation of motion can be given by,

$$\frac{dv_s}{dt} = \left(1 - \frac{\rho_a}{\rho_s}\right) g - \frac{3\rho_a}{4\rho_s d_s} C_D v_s^2 \qquad \text{(C.1)}$$

where C_D represents the drag coefficient.

The main difficulty in finding an analytical solution to Equation (C.1) is the drag coefficient term which is non-linear. Rayleigh proposed that the fundamentals of particle motion can be expressed in the form of a drag coefficient in terms of Reynolds number plot. For spheres such a curve has been determined up to Reynolds numbers of the order 10^6, by numerous experimenters. At low Reynolds numbers viscous flow exists around the sphere, in this Reynolds number range the drag coefficient can be approximated by the law of Stokes. At high Reynolds numbers the drag coefficient is approximately constant and has a value of *0.44*. This range is often termed Newton's law of particle motion. A transition region exists between these two ranges.

There are numerous drag correlations for spheres that represent the available standard drag coefficient data over the complete range of Reynolds numbers, discussed in Chapter 2.

In Figure 2.2 the correlations and the experimental values given by Lapple and Shepherd [1940LA1] are plotted. Figure C.1 shows the deviation between the correlations and the data and it is found that Turton and Levenspiel [1986TU1] and Clift et al. [1978CL1] fit the data well, differing marginally from each other in the applicable Reynolds number range.

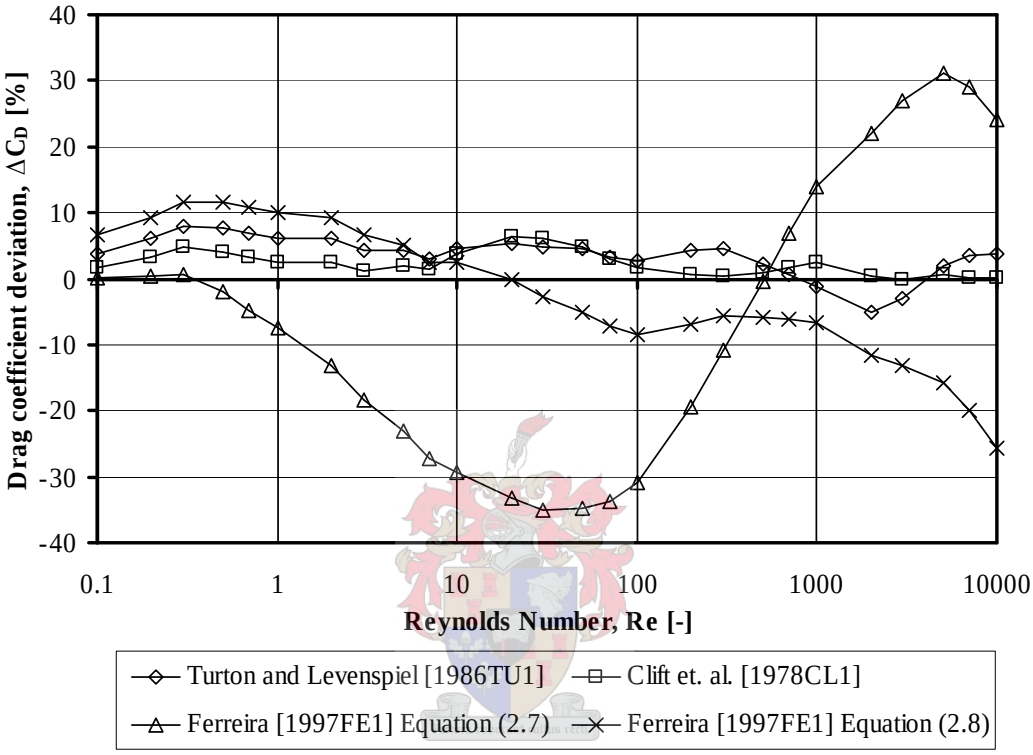

Figure C.1: Deviation between drag coefficient correlations and the data from Lapple and Shepherd [1940LA1].

From the definition of the Reynolds number, the spherical drop's velocity can be written as,

$$v_s = \frac{\mathrm{Re}\,\mu_a}{\rho_a d_s} \tag{C.2}$$

Substituting Equation (C.2) into Equation (C.1) and rearranging yields,

$$\frac{d\,\mathrm{Re}}{dt} = \alpha + \beta C_D\,\mathrm{Re}^2 \tag{C.3}$$

where

$$\alpha = \frac{\rho_a d_s}{\mu_a}\left(1-\frac{\rho_a}{\rho_s}\right)g \tag{C.4}$$

$$\beta = -\frac{3\mu_a}{4{d_s}^2\rho_s} \tag{C.5}$$

When terminal velocity is reached, the rate of change of Reynolds number with respect to time is zero, thus resulting in,

$$\left(C_D\,\mathrm{Re}^2\right)_T = \frac{4\rho_a g {d_s}^3\left(\rho_s-\rho_a\right)}{3{\mu_a}^2} \tag{C.6}$$

where the subscript *T* is for the terminal velocity condition. Equation (C.6) reveals the maximum value of C_DRe^2 that a sphere of size d_s can attain when falling freely in a gravitational field.

By separation of variables, Equation (C.3) can be integrated as follows,

$$\int_{t_0}^{t} dt = \int_{\mathrm{Re}_0}^{\mathrm{Re}} \frac{d\,\mathrm{Re}}{\alpha+\beta C_D\,\mathrm{Re}^2} \tag{C.7}$$

If the sphere starts from rest then $Re_0 = 0$. The denominator in Equation (C.7) contains a term C_DRe^2 which can be plotted against *Re* using the drag coefficient correlation of Turton and Levenspiel [1986TU1], Equation (2.6), for the Reynolds number range $0 \le Re \le 10^4$.

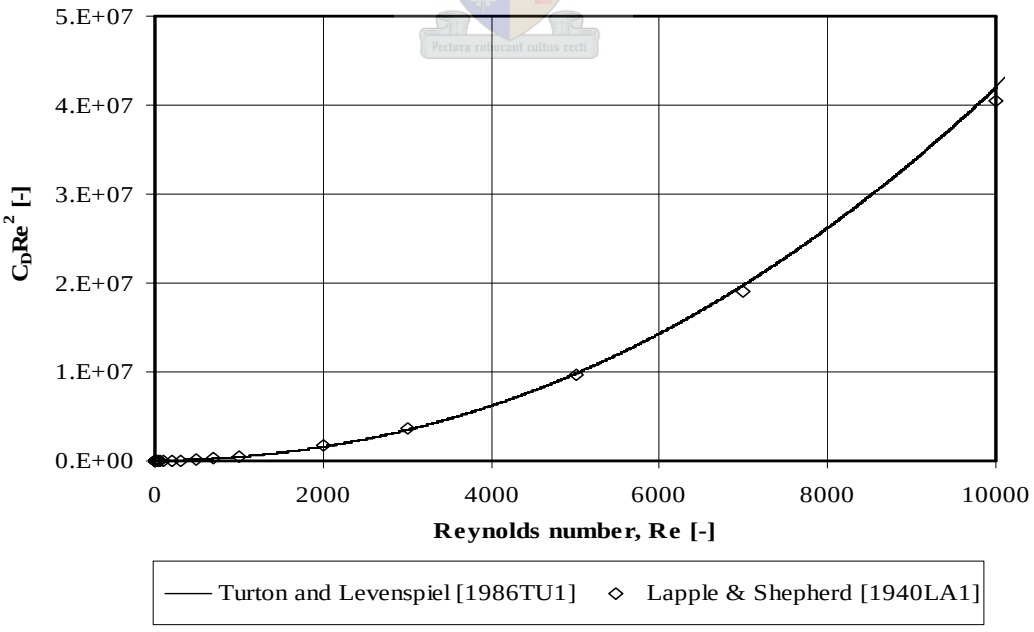

Figure C.2: C_DRe^2 as a function of Reynolds number.

Figure C.2 illustrates that the curve can accurately be represented by a parabolic equation, which lends itself to analytical solution. The parabolic equation for the curve presented in Figure C.2 is written as:

$$C_D \,\mathrm{Re}^2 = f\left(\mathrm{Re}\right) = b_1 \,\mathrm{Re}^2 + b_2 \,\mathrm{Re} + b_3 \tag{C.8}$$

The Reynolds number range, $0 \le Re \le 10^4$, has been subdivided to facilitate better accuracy. Each subinterval has a distinct parabolic equation, the coefficients of which are given in Table 2.3.

Substituting Equation (C.8) into Equation (C.7) and rearranging yields,

$$\int_{t_0}^{t} dt = \int_{\mathrm{Re}_0}^{\mathrm{Re}} \frac{d\,\mathrm{Re}}{E_1 \,\mathrm{Re}^2 + E_2 \,\mathrm{Re} + E_3} \tag{C.9}$$

where the constants in Equation (C.9) are represented by,

$$E_1 = b_1 \beta$$
$$E_2 = b_2 \beta$$
$$E_3 = \alpha + b_3 \beta$$

Equation (C.9) can be integrated directly to yield,

$$t\Big|_{t_0}^{t} = \frac{2}{\psi} \mathrm{atan}\left(\frac{2E_1 \,\mathrm{Re} + E_2}{\psi} \right)\Bigg|_{\mathrm{Re}_0}^{\mathrm{Re}} \tag{C.10}$$

where

$$\psi = \left(4E_3 E_1 - E_2^2\right)^{1/2}$$

Rearranging Equation (C.10) so that $Re = f(t)$ yields,

$$\mathrm{Re}(t) = \frac{1}{2E_1}\left(\psi \tan\left(\frac{\psi\left(t - t_0\right)}{2} + \mathrm{atan}\left(\frac{2E_1 \,\mathrm{Re}_0 + E_2}{\psi} \right) \right) - E_2 \right) \tag{C.11}$$

Using Equation (C.2) the velocity can be found.

$$v_s(t) = \frac{\mu_a}{2\rho_a d_s E_1}\left(\psi \tan\left(\frac{\psi\left(t - t_0\right)}{2} + \mathrm{atan}\left(\frac{2\rho_a d_s E_1 v_{s,0} + \mu_a E_2}{\mu_a \psi} \right) \right) - E_2 \right) \tag{2.17}$$

The acceleration and path length of the spherical drop are given below respectively.

$$a_s(t) = \frac{1}{4}\mu_a \frac{\psi^2}{\rho_a d_s E_1}\left(1+\tan\left(\frac{1}{2}\psi\left(t-t_0\right)+\operatorname{atan}\left(\frac{2E_1\rho_a d_s v_{s,0}+E_2\mu_a}{\mu_a\psi}\right)\right)^2\right) \tag{C.12}$$

$$\begin{aligned} s_s(t) = &-\frac{\mu_a}{2}\frac{-ln\left(sec^2\left(\frac{\psi\left(t-t_0\right)}{2}+tan^{-1}\left(\frac{2\rho_a d_s E_1 v_{s,0}+E_2\mu_a}{\mu_a\psi}\right)\right)\right)+E_2 t}{\rho_a d_s E_1} \\ &+\frac{\mu_a}{2}\frac{-ln\left(sec^2\left(tan^{-1}\left(\frac{2\rho_a d_s E_1 v_{s,0}+E_2\mu_a}{\mu_a\psi}\right)\right)\right)+E_2 t_0}{\rho_a d_s E_1} \end{aligned} \tag{2.18}$$

D

Re-correlation of the Data by Yao and Schrock [1976YA1] for Heat and Mass Transfer from Vertically Free-Falling Accelerating Water Drops

Yao and Schrock [1976YA1] determined the heat and mass transfer coefficients for large water drops accelerating from rest in still air by conducting a series of experiments. They measured the drop temperature at a measurement station located at different heights for drops with different diameters.

The data covered the following ranges: $3 \le d \le 6mm$, $29 \le \Phi \le 100\%$ and $0.18 \le z \le 2.9m$. The ambient air drybulb temperature was held between 294.45 and $296.75K$, while the initial temperature of the water drops was at approximately $313.85K$.

Yao and Schrock [1976YA1] correlated their data using their proposed modified form of the Ranz and Marshall correlation,

$$Nu_{YS} = 2 + g_{YS}\left(0.6\, Re^{1/2}\, Pr^{1/3}\right) \quad \text{for } Re < 2500 \tag{3.8}$$

where the term g_{YS} is introduced to account for acceleration, drop deformation, internal circulation and drop oscillation effects. The correlation for g_{YS} proposed by Yao and Schrock [1976YA1] is given below,

$$g_{YS} = 25\left(\frac{z}{d}\right)^{-0.7} \quad \text{for } 10 < \left(\frac{z}{d}\right) < 600 \tag{3.9}$$

Referring to Figure 3.1, it can be seen that this correlation over-predicts the cooling of a water drop. Furthermore employing this correlation for any of the Yao and Schrock [1976YA1] experimental cases did not correlate their experimental data. Chen and Trezek [1977CH1] and Erens et al. [1994ER1] also noticed this. Erens et al. [1994ER1] re-correlated the data and proposed the following equation including an acceleration term:

$$g_{YS} = 0.22 + 3.15\left(\frac{(dv/dt)\, d_d}{v^2 d_m}\right)^{0.2} \quad \text{for } \frac{(dv/dt)\, d_d}{v^2} > 5\times 10^{-4} \tag{3.10}$$

Figure 3.1 shows that the correlation by Erens et al. [1994ER1] under predicts the cooling of a drop.

The re-correlation procedure, used in this thesis, of the data by Yao and Schrock [1976YA1] is now given.

By reordering Equation (3.5) an equation for the Nusselt number for a vertically free-falling water drop is given.

$$Nu_{YS} = \frac{hd_d}{k_a} = \frac{d_d}{k_a}\left(\frac{\frac{1}{6} c_v d_d \frac{dT_d}{dt}}{(T_a - T_d) - \frac{h_{fg} Sc}{\rho_a c_{v,a} Pr}(C_d - C_a)} \right) \tag{D.1}$$

Yao and Schrock [1976YA1] present their experimental data in the form of drop temperature and fall distance. The fall distance of the relevant drops can be determined as a function of time numerically using Equation (2.15) for drop deformation. The temperature can now be presented as a function of time for each drop. The resulting curves exhibit a linear characteristic, thus the gradient, dT_d/dt, of the curves can be found and substituted into Equation (D.1) to calculate Nu_{YS} for each experimental data point. The required drop thermophysical properties are calculated for each data point and the air conditions are assumed constant. The correction factor, g_{YS}, can be calculated for each data point from Equation (3.8).

Figure D.1 shows the correction factor plotted as a function of the dimensionless fall distance.

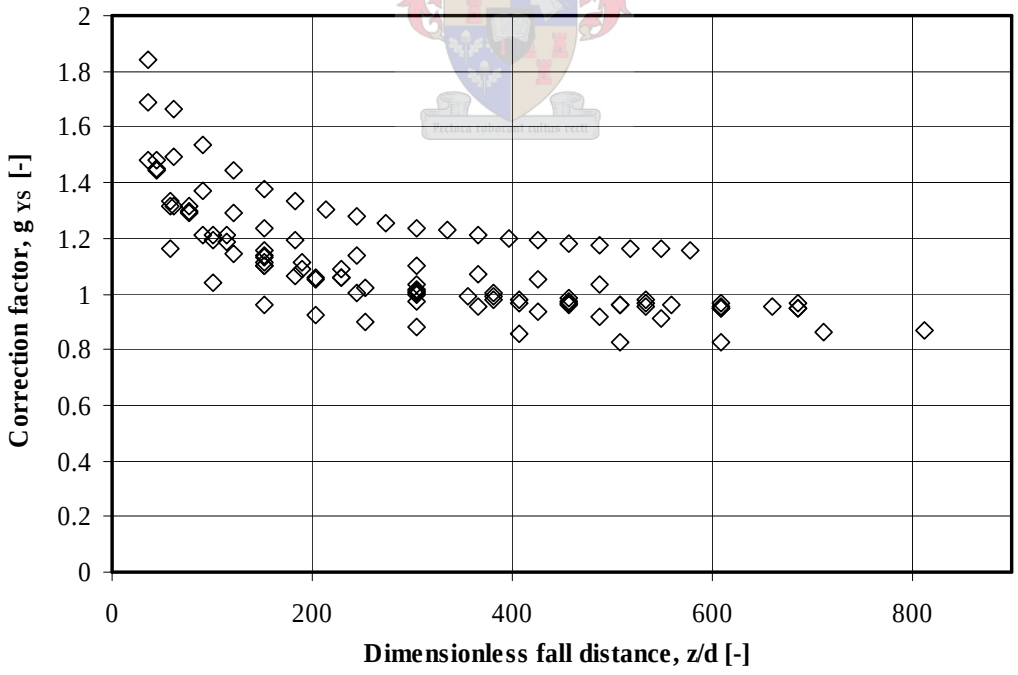

Figure D.1: Correction factor for Ranz and Marshall correlation as a function of dimensionless fall distance.

Once the acceleration is zero the experimental correction values should be in the order of unity, as Ranz and Marshall [1952RA1] conducted their experiments on stationary drops in a steady air stream. The data in the Figure D.1 shows an asymptotic characteristic, the value of the asymptote being in the order of *0.8 – 1.2*.

Yao and Schrock [1976YA1] used the dimensionless fall distance, *z/d*, to correlate the correction factor, which does not take the effect of air flow on the drop acceleration into consideration. The author uses an acceleration based variable to correlate the experimental data.

The calculation procedure for the selection of the dimensionless variable to be used to correlate the experimental data is now given.

Consider the equation of motion for a deformable drop, given by,

$$\frac{dv_d}{dt} = \frac{(\rho_d - \rho_a)}{\rho_d} g - \frac{3}{4} \frac{\rho_a}{\rho_d d_e} E^{-2/3} C_D v_{ad}^2 \tag{D.2}$$

where d_e is the equivalent spherical diameter. The v_{ad}^2 term in Equation (D.2) can be rewritten in terms of Reynolds number. For the terminal velocity condition this simplifies to:

$$\left(C_D\, Re^2\right)_T = \left(\frac{4\rho_a (\rho_d - \rho_a) d_e^3 g}{3\mu_a^2} \right) E_T^{2/3} \tag{D.3}$$

The value of Equation (D.3) is a fixed and maximum value attainable for a specific drop diameter as the right-hand-side of the equation is only a function of the drop diameter and thermophysical properties of the drop and the continuous phase and the terminal drop deformation of the drop. For each drop diameter the instantaneous $C_D Re^2$ value can be normalized by Equation (D.3).

The recalculated correction factor data is correlated using the *abscissa* of Figure D.2. The correlation is given by,

$$g_{YS} = 0.68 \left(\frac{C_D\, Re^2}{\left(C_D\, Re^2\right)_T} \right)^{-0.28} + \frac{0.95}{\left(1 + 1.4 \left(\frac{C_D\, Re^2}{\left(C_D\, Re^2\right)_T} \right)^{-2} \right)} \tag{3.12}$$

Interestingly Equation (3.12) resembles the last two terms of the Turton and Levenspiel [1986TU1] drag correlation, Equation (2.6).

Figure D.2 shows that two of the data sets (data sets 3 and 7) do not follow the same trend as the other data and are therefore excluded from the data used to determine Equation (3.12).

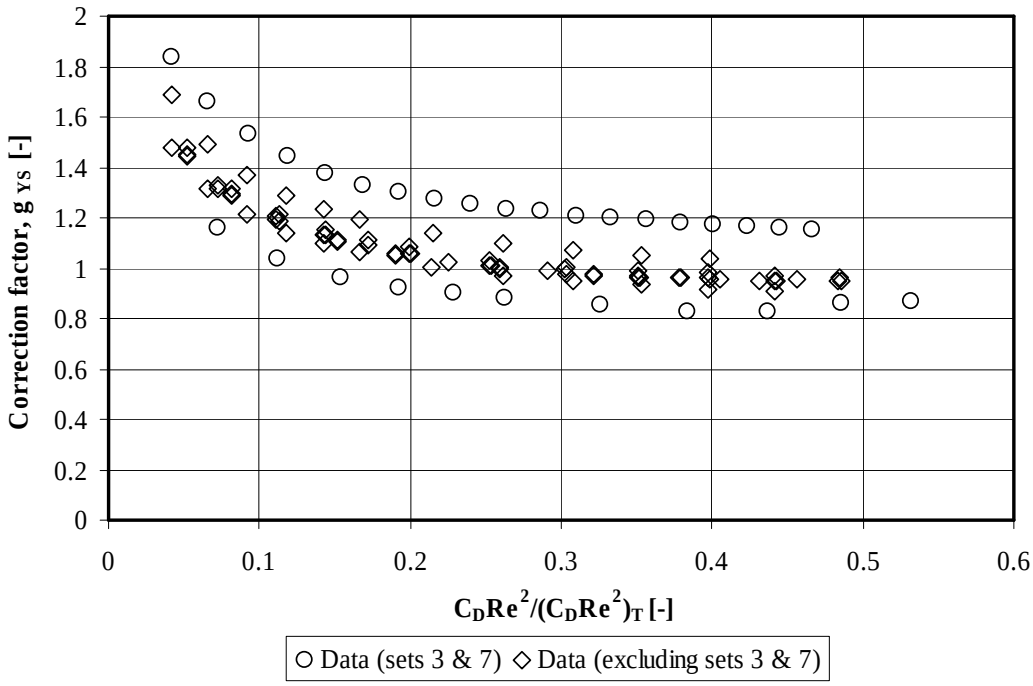

Figure D.2 Correction factor, g_{YS}, as a function of $C_DRe^2/(C_DRe^2)_T$.

Figure 3.1 is used to draw comparison between the different correlations, from the figure it is obvious that Equation (3.12) fits the data better than any of the other correlations.

It was found that the sensitivity of the results is mostly affected by the first part of the curve. From Figure D.2 it can be seen that the correction factor changes from approximately *1.6* at an *abscissa* value of approximately *0.05*, where the drop acceleration is the highest, to approximately *1* at an *abscissa* value of approximately *0.25*, after which it remains virtually constant. This indicates that the most significant effect of acceleration on the Nusselt number is during the initial acceleration stage.

Figure D.3 shows that by using Equation (3.12), the experimental data of Yao and Schrock [1976YA1] can be predicted satisfactorily for different drop diameters. Figure 3.1 shows that the Ranz and Marshall [1952RA1] equation is conservative. FLUENT 6.2.16 exclusively uses the correlations of Ranz and Marshall [1952RA1]. Thus for the purposes of this thesis these correlations will suffice.

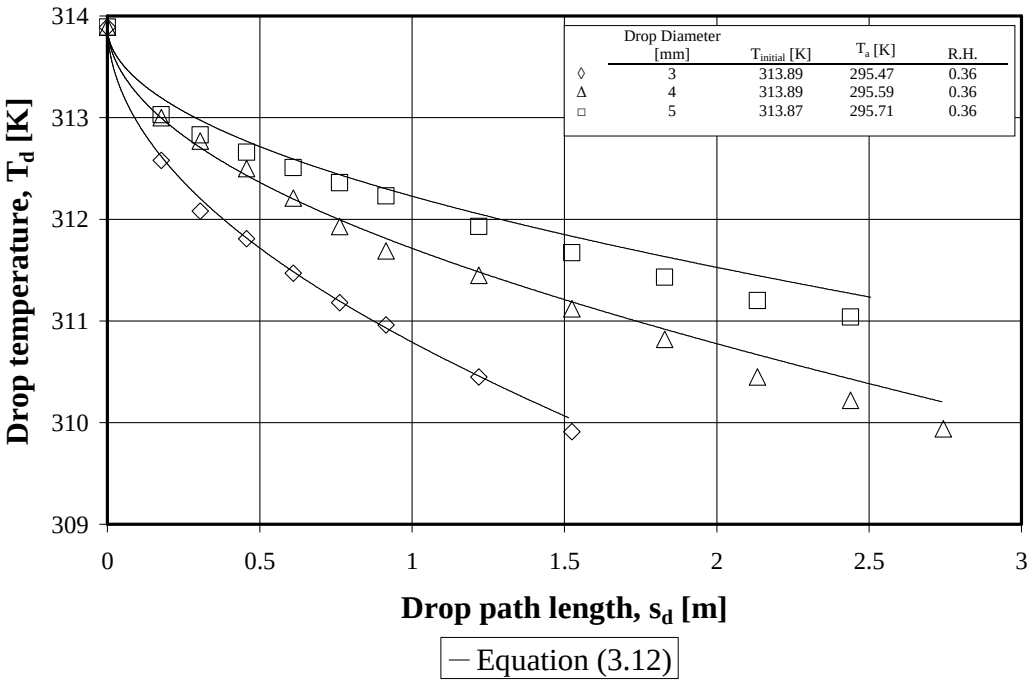

Figure D.3: Experimental data of Yao and Schrock [1976YA1] and predicted results using Equation (3.12).

APPENDIX

E

Analytical Solution for the Cooling of a Spherical Water Drop in an Air Stream

The governing equation for the mass transfer of the spherical water drop is given by,

$$\frac{dM_s}{dt} = -h_D A_S \left(C_s - C_a\right) \tag{3.1}$$

where A_S and M_s are the surface area and the mass of the spherical water drop respectively, C_s is the vapour concentration at the spherical water drop's surface, where saturated conditions exist, and C_a is the vapour concentration in the continuous phase, air. The thermophysical properties of the air are assumed to remain constant. For the conditions simulated in a cooling tower the change in the density of the water is less than one percent, thus it is assumed to be constant.

Equation (3.1) can be rewritten as,

$$\frac{dd_s}{dt} = -\frac{2}{\rho_s} h_D \left(C_s - C_a\right) \tag{E.1}$$

The governing equation for the conservation of energy of the spherical water drop is given by,

$$\frac{dT_s}{dt} = \frac{hA_S}{M_s c_v}\left(T_a - T_s\right) - \frac{h_D A_S}{M_s c_v}\left(C_s - C_a\right) h_{fg} \tag{3.5}$$

The first term on the right-hand-side of Equation (3.5) represents the convection heat transfer and the second term represents the enthalpy transfer due to mass transfer. T_s is the temperature at the surface of the spherical water drop which is equal to the average drop temperature due to the assumption of the *complete mixing model*. T_a is the temperature of the air, which is assumed to remain constant. The definitions of the vapour concentrations are given below,

$$C_s = \frac{p_{vs}\left(T_s\right)}{RT_s} \tag{E.2}$$

$$C_a = X_v \frac{p_a}{RT_a} \tag{E.3}$$

where R is the universal gas constant, $p_{vs}(T_s)$ is the saturated vapour pressure taken at the spherical water drop's temperature, p_a is the atmospheric pressure and X_v is the mass fraction of the water vapour in the air.

Equations (E.1) and (3.5) are coupled and thus need to be solved simultaneously. The equations can be combined to form a single equation by dividing Equation (3.5) by Equation (E.1) which yields,

$$\frac{dT_s}{dd_s} = -\frac{3}{c_v}\frac{h}{h_D}\frac{T_a - T_s}{C_s - C_a}\frac{1}{d_s} + \frac{3h_{fg}}{c_v}\frac{1}{d_s} \tag{3.13}$$

The resulting equation is separable and thus it can be solved analytically. The equation contains a number of variables some of which are assumed to remain constant so as to simplify the equation by reducing the number of dependent variables. From a numerical study of the equation it can be seen that the latent heat, h_{fg}, and specific heat at constant volume, c_v, do not vary considerably, thus they will be taken as constant. The remaining variables are found to be functions of temperature, velocity or diameter.

The convection heat transfer coefficient is a function of the temperature and the velocity, given by,

$$h = \frac{k_a Nu}{d_s} \tag{3.4}$$

where k_a is the thermal conductivity of the air. The Nusselt number can be calculated using the correlation proposed by Ranz and Marshall [1952RA1],

$$Nu = 2 + 0.6\, Re^{1/2}\, Pr^{1/3} \text{ for } 2 \le Re \le 800 \tag{3.6}$$

The mass transfer coefficient is a function of the temperature, velocity and diameter of the spherical drop, given by,

$$h_D = \frac{D\, Sh}{d_s} \tag{3.2}$$

where D is the diffusion coefficient. The Sherwood number can be calculated using the correlation proposed by Ranz and Marshall [1952RA1],

$$Sh = 2 + 0.6\, Re^{1/2}\, Sc^{1/3} \text{ for } 2 \le Re \le 800 \tag{3.7}$$

Miura et al. [1977MI1] show that the correlations of Ranz and Marshall [1952RA1] accurately predict the heat and mass transfer for Reynolds numbers of up to *2000*.

Substitution of Equations (3.4), (3.2), (E.2) and (E.3) into Equation (3.13) yields,

$$\frac{dT_s}{dd_s} = -\frac{3kR}{c_v D}\frac{Nu}{Sh}\frac{\left(T_a - T_s\right)}{\left(\frac{p_{vs}\left(T_s\right)}{T_s} - X_v\frac{p_a}{T_a}\right)}\frac{1}{d_s} + \frac{3h_{fg}}{c_v}\frac{1}{d_s} \tag{E.4}$$

The Nusselt and Sherwood ratio is inherent in the Lewis number definition,

$$\frac{Nu}{Sh} = Le^{-1/3} \tag{E.5}$$

In a cooling tower the Lewis number can be taken to be equal to unity. Equation (E.4) is now an equation where all the variables are functions of temperature and diameter.

The bracketed term in the denominator of the first term on the right-hand-side of Equation (E.4) is dependent on the spherical water drop's temperature and can thus be substituted for by,

$$\frac{p_{vs}\left(T_s\right)}{T_s} - X_v\frac{p_a}{T_a} = f\left(T_s\right) + A \tag{E.6}$$

where the new constant *A* is a function of the thermophysical properties of the continuous phase, air.

Substitution of Equations (E.5) and (E.6) into Equation (E.4) yields,

$$\frac{dT_s}{dd_s} = -\frac{3k_a R}{c_v D}\frac{\left(T_a - T_s\right)}{\left(f\left(T_s\right) + A\right)}\frac{1}{d_s} + \frac{3h_{fg}}{c_v}\frac{1}{d_s} \tag{E.7}$$

The ratio of saturated vapour pressure to spherical water drop temperature can be represented by means of a parabolic equation in terms of spherical water drop temperature,

$$f\left(T_s\right) = a_1 T_s^{\,2} + a_2 T_s + a_3 \tag{E.8}$$

where,

$$a_1 = 0.017$$

$a_2 = -9.5279$

$a_3 = 1340.5$

These constants were determined by using the definition of the saturated vapour pressure as given by Kröger [1998KR1] to determine discrete numerical values for the ratio of saturated vapour pressure to spherical water drop temperature. The coefficients of Equation (E.8) are obtained by means of a least squares curve fit. The temperature range is from *290K* to *314K*, as this is the range of cooling generally encountered in wet-cooling towers.

Equation (E.7) is separable and can be solved analytically. To simplify the equation, the following dimensionless parameters are defined:

$$\eta = \frac{d_s}{d_{s,0}}$$

$$\theta = \frac{T_s - T_a}{T_{s,0} - T_a}$$

where $d_{s,0}$ and $T_{s,0}$ are the initial values for the diameter and temperature of the spherical water drop respectively.

Rewriting Equation (E.7) in terms of η and θ yields,

$$\frac{d\theta}{d\eta} = \beta \frac{\theta}{\alpha_1 \theta^2 + \alpha_2 \theta + \alpha_3} \frac{1}{\eta} + \xi \frac{1}{\eta} \tag{E.9}$$

where,

$$\alpha_1 = a_1 \left(T_{s,0} - T_a\right)^2$$

$$\alpha_2 = \left(T_{s,0} - T_a\right)\left(2a_1 T_a + a_2\right)$$

$$\alpha_3 = a_1 T_a^2 + a_2 T_a + a_3 + A$$

$$\beta = \frac{3k_a R}{c_v D}$$

$$\xi = \frac{3h_{fg}}{c_v \left(T_{s,0} - T_a\right)}$$

By separation of variables, Equation (E.9) can be integrated.

$$\int_\eta^1 \frac{1}{\eta} d\eta = \int_\theta^1 \frac{1}{\beta \dfrac{\theta}{\alpha_1 \theta^2 + \alpha_2 \theta + \alpha_3} + \xi} d\theta \tag{E.10}$$

The analytical solution to the integration is given below.

$$ln(\eta) = \frac{1}{\xi}(\theta - 1) - \frac{\beta}{2\xi^2\alpha_1} ln\left(\frac{\xi\alpha_1\theta^2 + I_1\theta + \xi\alpha_3}{\xi\alpha_1 + I_1 + \xi\alpha_3}\right) \\ ... + \frac{\beta I_1}{\xi^2\alpha_1 I_2}\left(tan^{-1}\left(\frac{2\xi\alpha_1\theta + I_1}{I_2}\right) - tan^{-1}\left(\frac{2\xi\alpha_1 + I_1}{I_2}\right)\right) \tag{3.14}$$

where the constants of integration are defined as,

$$I_1 = \beta + \alpha_2\xi$$
$$I_2 = \left(4\xi^2\alpha_3\alpha_1 - I_1^2\right)^{1/2}$$

Now it is possible to express η as a function of θ.

$$\eta = e^{RHS} \tag{3.15}$$

where *RHS* is the right-hand-side of Equation (3.14).

It is possible to simplify the solution by using a linear curve fit to represent the ratio of saturated vapour pressure to spherical water drop temperature,

$$f\left(T_s\right) = a_4 T_s + a_5 \tag{E.11}$$

where,

$$a_4 = 0.748$$
$$a_5 = -210.451$$

The integral equation now becomes,

$$\int_\eta^1 \frac{1}{\eta} d\eta = \int_\theta^1 \frac{1}{\beta\dfrac{\theta}{\alpha_4\theta + \alpha_5} + \xi} d\theta \tag{E.12}$$

where,

$$\alpha_4 = a_4\left(T_{s,0} - T_a\right)$$
$$\alpha_5 = a_5 + a_4 T_a + A$$

The definite integral solution then becomes,

$$ln(\eta) = \frac{\alpha_4}{J}(\theta - 1) - \frac{\alpha_5 \beta}{J^2} ln\left(\frac{J\theta + \xi\alpha_5}{J + \xi\alpha_5}\right) \tag{E.13}$$

where,

$$J = \beta + \xi\alpha_4$$

Once again η can be written as a function of θ using Equation (3.15) with RHS referring to the right-hand-side of Equation (E.13).

Figure E.1 is used to illustrate the results obtained by Equations (3.14) and (E.13).

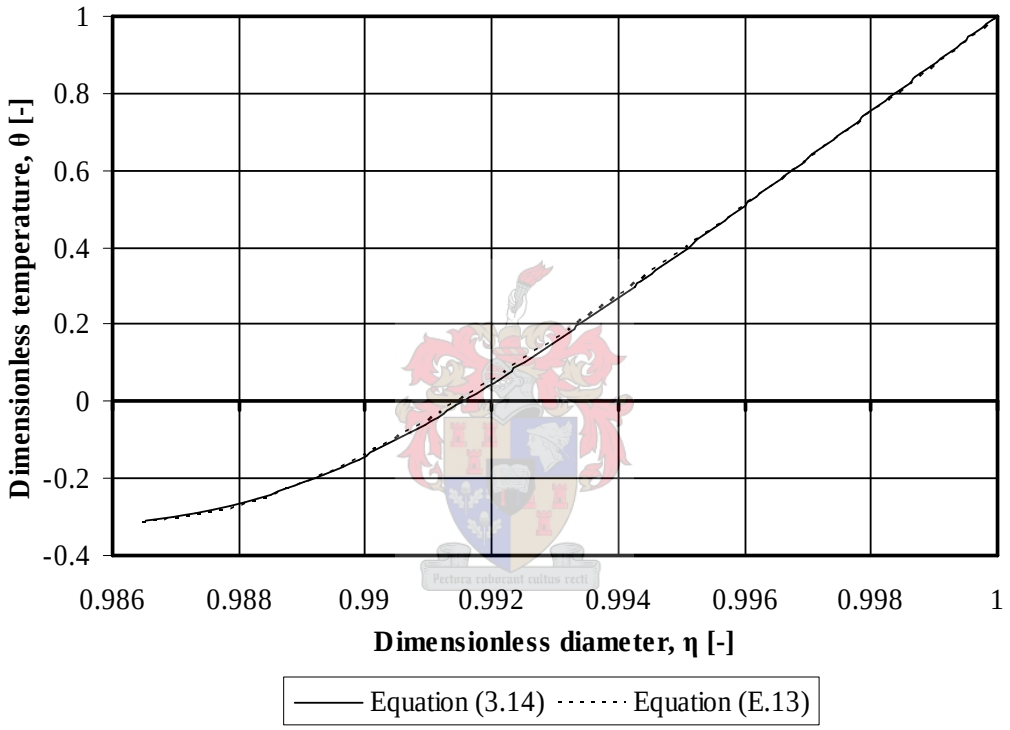

Figure E.1: Dimensionless temperature as a function of dimensionless diameter for Equations (3.14) and (E.13).

APPENDIX

F

Experimental Data

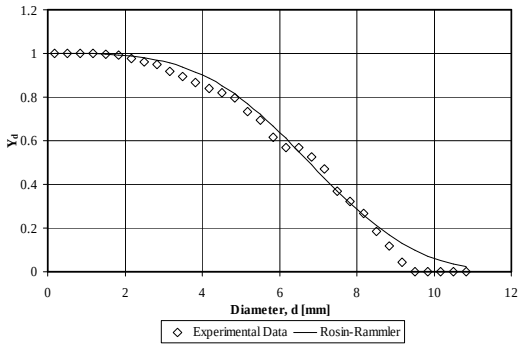

(a) $G_w = 1.34 kg/m^2s$ $G_a = 1.60 kg/m^2s$

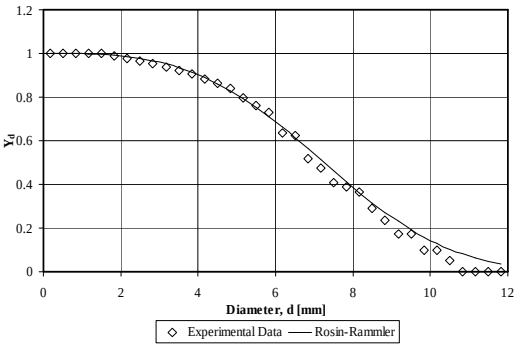

(b) $G_w = 1.34 kg/m^2s$ $G_a = 2.44 kg/m^2s$

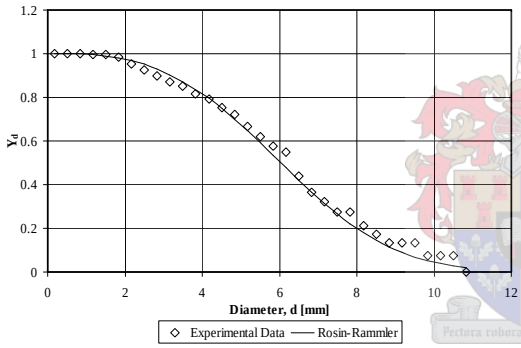

(c) $G_w = 1.33 kg/m^2s$ $G_a = 3.20 kg/m^2s$

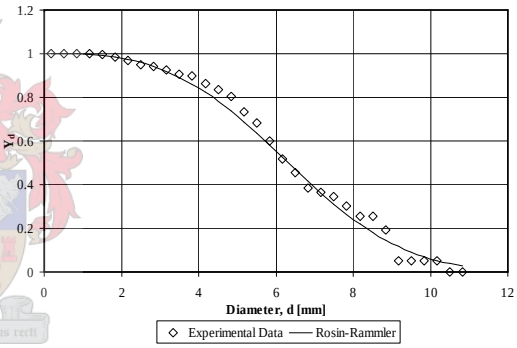

(d) $G_w = 1.75 kg/m^2s$ $G_a = 1.60 kg/m^2s$

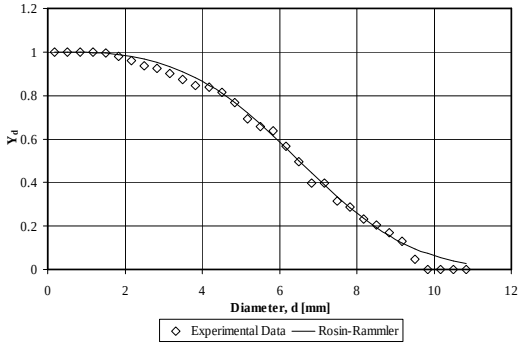

(e) $G_w = 1.73 kg/m^2s$ $G_a = 2.43 kg/m^2s$

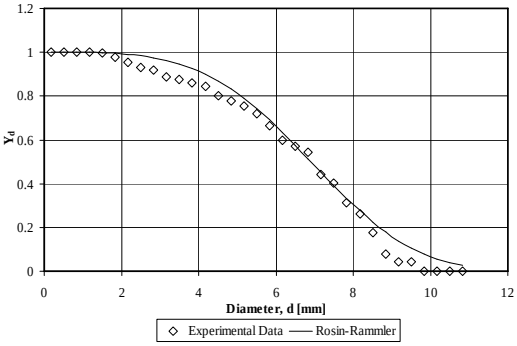

(f) $G_w = 1.76 kg/m^2s$ $G_a = 3.19 kg/m^2s$

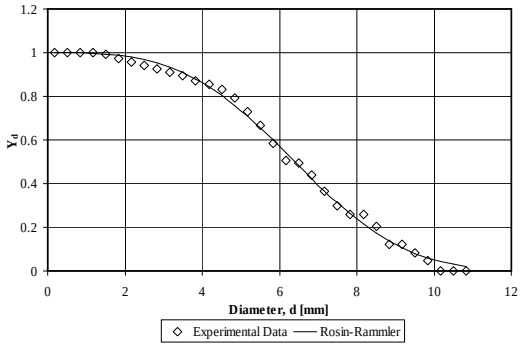

(g) $G_w = 2.21 kg/m^2s$ $G_a = 1.59 kg/m^2s$

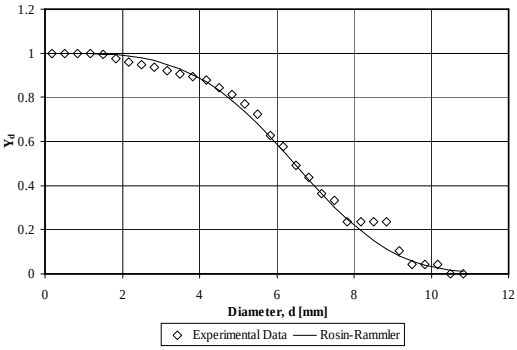

(h) $G_w = 2.21 kg/m^2s$ $G_a = 2.42 kg/m^2s$

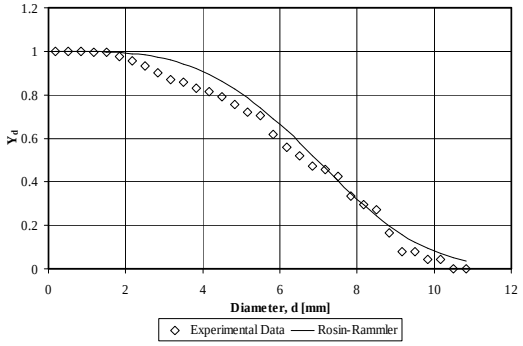

(i) $G_w = 2.28 kg/m^2s$ $G_a = 3.19 kg/m^2s$

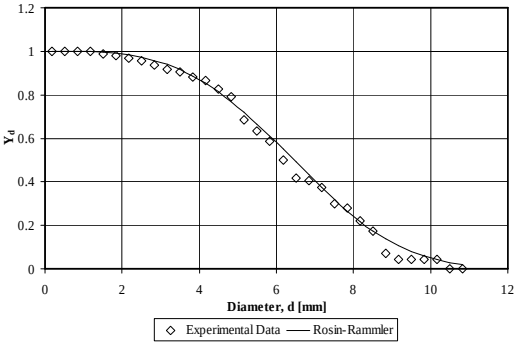

(j) $G_w = 2.57 kg/m^2s$ $G_a = 1.59 kg/m^2s$

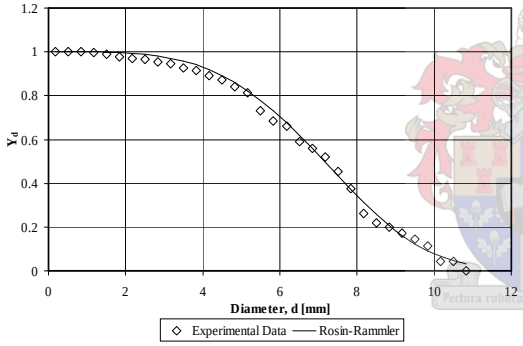

(k) $G_w = 2.57 kg/m^2s$ $G_a = 2.43 kg/m^2s$

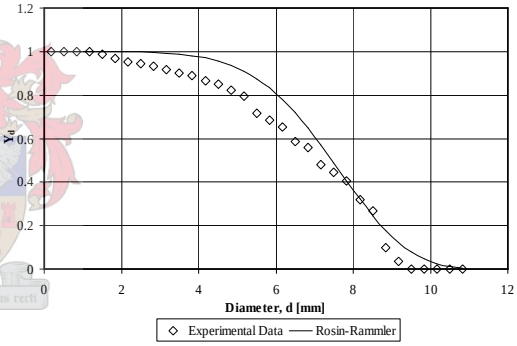

(l) $G_w = 2.54 kg/m^2s$ $G_a = 3.20 kg/m^2s$

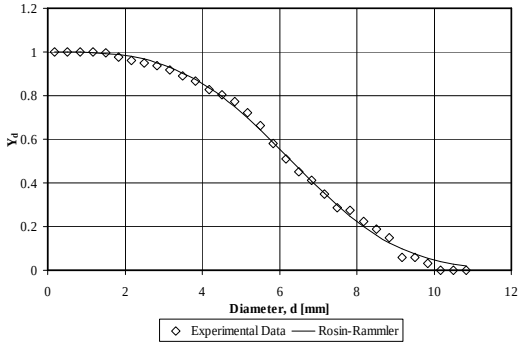

(m) $G_w = 2.85 kg/m^2s$ $G_a = 1.58 kg/m^2s$

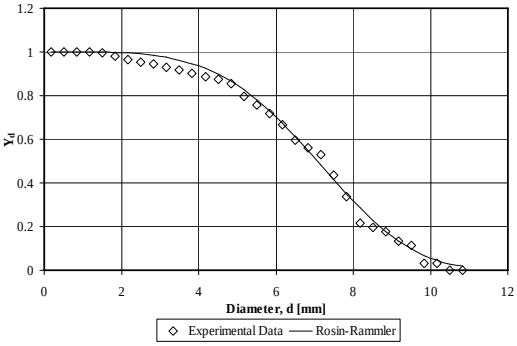

(n) $G_w = 2.85 kg/m^2s$ $G_a = 2.44 kg/m^2s$

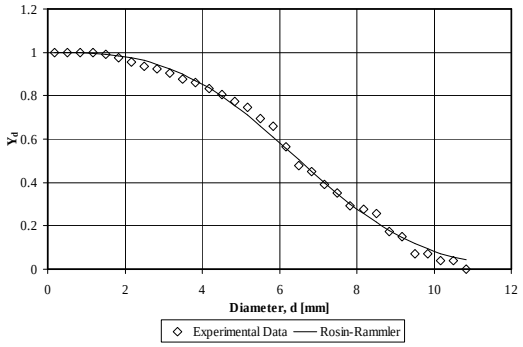

(o) $G_w = 2.87 kg/m^2s$ $G_a = 3.19 kg/m^2s$

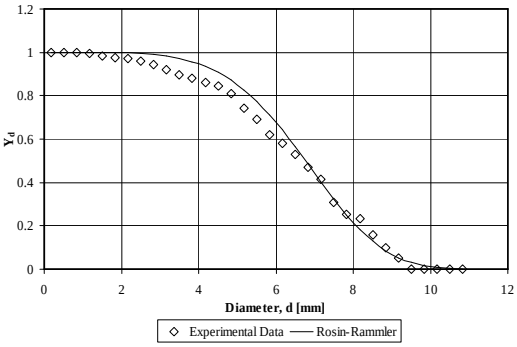

(p) $G_w = 3.99 kg/m^2s$ $G_a = 1.58 kg/m^2s$

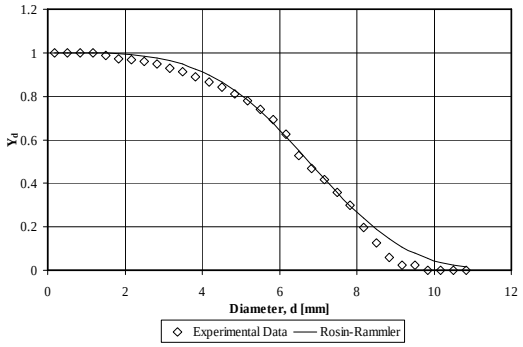

(q) $G_w = 3.95 kg/m^2s$ $G_a = 2.44 kg/m^2s$

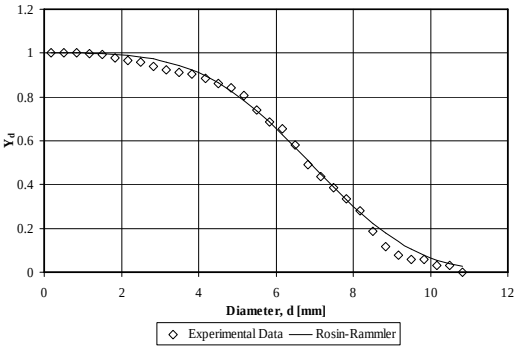

(r) $G_w = 3.84 kg/m^2s$ $G_a = 3.18 kg/m^2s$

Figure F.1: Experimental drop size data and Rosin-Rammler distribution function.

Table F.1: Experimental data for rain zone loss coefficient.

p_a [N/m^2]	T_a [K]	T_w [K]	time [s]	V_w [V]	Δp_n [mmH_2O]	Δp_{rz} [mmH_2O]	ρ_a [kg/m^3]	ρ_w [kg/m^3]	Q_w [ℓ/s]	Q_{bt} [ℓ/s]	Q_{ts} [ℓ/s]	G_w [kg/m^2s]	G_a [kg/m^2s]	Δp_{rz} [N/m^2]	K_{rz} [-]
100460	296.612	294.375	0	0	9.9	0.03	1.18	997.9	0	0	0	0	1.6	0.29	0.27
100200	293.029	292.423	57	1.25828	9.85	0.40	1.19	998.29	3.62	1.61	2.01	1.34	1.6	3.92	3.63
100200	292.423	292.731	49	1.36142	9.8	0.45	1.19	998.23	4.51	1.87	2.64	1.75	1.6	4.41	4.1
100200	293.464	292.886	40	1.52364	9.7	0.55	1.19	998.2	5.62	2.3	3.32	2.21	1.59	5.39	5.07
100200	293.293	292.782	35	1.68896	9.65	0.65	1.19	998.22	6.49	2.62	3.87	2.57	1.59	6.37	6.02
100200	293.311	292.775	29	1.92953	9.6	0.75	1.19	998.22	7.45	3.17	4.28	2.85	1.58	7.34	6.98
100460	294.149	293.76	22	2.78414	9.6	0.95	1.19	998.03	10.17	4.17	6	3.99	1.58	9.3	8.84
100460	297.495	294.36	0	0	22.65	0.05	1.18	997.9	0	0	0	0	2.42	0.49	0.2
100200	293.242	292.467	57	1.25846	22.8	0.55	1.19	998.28	3.62	1.61	2.01	1.34	2.44	5.39	2.16
100200	293.435	292.745	48	1.3617	22.65	0.60	1.19	998.23	4.51	1.91	2.6	1.73	2.43	5.88	2.37
100200	293.369	292.773	40	1.52378	22.4	0.75	1.19	998.22	5.62	2.3	3.32	2.21	2.42	7.34	2.99
100200	293.328	292.743	35	1.68878	22.7	0.85	1.19	998.23	6.49	2.62	3.87	2.57	2.43	8.32	3.35
100200	293.295	292.678	29	1.92843	22.8	0.95	1.19	998.24	7.45	3.17	4.28	2.85	2.44	9.3	3.72
100460	294.38	293.848	22	2.76548	22.9	1.25	1.19	998.01	10.11	4.17	5.94	3.95	2.44	12.24	4.88
100460	298.004	294.317	0	0	40	0.10	1.17	997.91	0	0	0	0	3.21	0.98	0.22
100460	294.452	293.582	58	1.25479	39.2	0.65	1.19	998.06	3.58	1.58	2	1.33	3.2	6.36	1.48
100460	294.36	293.477	49	1.36118	39	0.70	1.19	998.09	4.51	1.87	2.64	1.76	3.19	6.85	1.6
100460	294.479	293.56	41	1.53075	39.1	0.95	1.19	998.07	5.66	2.24	3.42	2.28	3.19	9.3	2.17
100460	294.508	293.754	34	1.69702	39.2	1.05	1.19	998.03	6.52	2.7	3.82	2.54	3.2	10.28	2.39
100460	294.593	293.879	29	1.93703	39.1	1.20	1.19	998	7.48	3.17	4.31	2.87	3.19	11.75	2.74
100460	294.722	294.113	21	2.77867	38.9	1.60	1.19	997.96	10.15	4.37	5.77	3.84	3.18	15.66	3.67

G

Sample Calculation for the Rain Zone Loss Coefficient Test in the Cooling Tower Test Facility

A sample calculation is performed for one of the test conditions used to determine the rain zone loss coefficient of a counterflow rain zone. The sample calculation procedure is discussed in Chapter 4. During the particular test the following data was measured:

Ambient temperature	T_a = 293.328K
Atmospheric pressure	p_a = 100200N/m^2
Air flow nozzle water micromanometer reading	ΔH_n = 22.7mm
Water pressure transducer voltage output	V_w = 1.68878V
Sample time	t_{bt} = 35s
Volume of water in bypass tank	V_{bt} = 0.09183m^3
Rain zone pressure drop micromanometer reading	ΔH_{rz} = 0.85mm
Temperature of the water	T_w = 292.743K

The density of the water is calculated from Equation (A.14),

$$\rho_w = \left(\begin{array}{l} 1.49343\times10^{-3} - 3.7164\times10^{-6}\left(292.743\right) + 7.09782\times10^{-9}\left(292.743\right)^2 \\ -1.90321\times10^{-20}\left(292.743\right)^6 \end{array} \right)^{-1}$$
$$= 998.23\,kg/m^3$$

The density of the air is calculated from Equation (A.1),

$$\rho_a = \frac{100200}{287.08\times293.328} = 1.19\,kg/m^3$$

The air and water mass velocities are calculated as follows:
Pressure difference over air flow nozzle ($\times 10$ Betz water micromanometer)

$$\Delta p_a = 10\Delta H_n = 10\times22.7 = 227\,N/m^2$$

Air flow nozzle throat cross sectional area:
$d_n = 0.455m$

$$A_n = \pi\left(\frac{d_n}{2}\right)^2 = \pi\left(\frac{0.455}{2}\right)^2 = 0.1626\,m^2$$

Test section cross sectional area:
$A_{ts} = 1m \times 1.5m = 1.5m^2$

Velocity of the air in the test section:

$$v_{ts} = C_n \left(\frac{2\Delta p_n}{\rho_a \kappa} \right)^{0.5} \frac{A_n}{A_{ts}} = 0.96 \left(\frac{2 \times 227}{1.19 \times 0.988} \right)^{0.5} \frac{0.1626}{1.5} = 2.04\, m/s$$

Air mass velocity in the test section:

$$G_a = \rho_a v_{ts} = 1.19 \times 2.04 = 2.43\, kg/m^2 s$$

Pressure difference over water venturi flow meter:

$$\Delta p_w = 15.996 V_w - 16.006 = 15.996 \times 1.68878 - 16.006 = 11.007\, kN/m^2$$

Water flow rate to the distribution manifold:

$$\begin{aligned} Q_w &= 1.73 \times 10^{-7} \Delta p_w^5 - 2.915 \times 10^{-5} \Delta p_w^4 + 1.819 \times 10^{-3} \Delta p_w^3 \\ &\quad -5.363 \times 10^{-2} \Delta p_w^2 + 0.9511 \Delta p_w + 0.4887 \\ &= 1.73 \times 10^{-7} (11.007)^5 - 2.915 \times 10^{-5} (11.007)^4 + 1.819 \times 10^{-3} (11.007)^3 \\ &\quad -5.363 \times 10^{-2} (11.007)^2 + 0.9511 (11.007) + 0.4887 \\ &= 6.49\, \ell/s \end{aligned}$$

Water flow rate in the bypass troughs:

$$Q_{bt} = \frac{V_{bt}}{t} = \frac{0.09183}{35} = 2.62\, \ell/s$$

Water flow rate in the test section:

$$Q_{ts} = Q_w - Q_{bt} = 6.49 - 2.62 = 3.87\, \ell/s$$

Water mass velocity in the test section:

$$G_w = \frac{\rho_w Q_{ts}}{A_{ts}} = \frac{998.23 \times 0.00387}{1.5} = 2.57\, kg/m^2 s$$

The rain zone loss coefficient is calculated as follows:
Pressure drop over the test section:

$$\Delta p_{rz} = \rho_w g \Delta H_{rz} = 998.23 \times 9.81 \times 0.00085 = 8.32\, N/m^2$$

Rain zone loss coefficient:

$$K_{rz} = \frac{\Delta p_{ts}}{\frac{1}{2} \rho_a v_{ts}^2} = \frac{8.32}{0.5 \times 1.19 \times (2.04)^2} = 3.35$$

APPENDIX

H

Rosin-Rammler Distribution Function Analysis

In reality a rain zone consists of a number of different drop sizes referred to as a polydisperse drop distribution. The drop size data that was experimentally determined in Chapter 4 are polydisperse drop distributions. A polydisperse drop distribution can be described by a log-normal or Rosin-Rammler distribution function to name but a few. This thesis confines itself to an analysis of the Rosin-Rammler distribution function due to its inclusion in FLUENT 6.2.16. A polydisperse drop distribution can also be represented by a monodisperse drop distribution. A monodisperse drop distribution consists of only one diameter, which is usually taken to be one of the representative diameters that derive from the polydisperse drop distribution through relevant arithmetical operations.

The accuracy of the Rosin-Rammler distribution function is analysed with respect to the rain zone performance parameters. The analysis is performed by implementing a goodness of fit technique.

H.1 Performance Parameters' Sensitivity

The objective of this section is to show how well the Rosin-Rammler distribution function correlates the experimental polydisperse drop distribution data. To this end, the water outlet temperature and pressure drop are predicted for a counterflow rain zone using CFD and the experimental polydisperse drop distribution data. These results are compared with corresponding results obtained using the Rosin-Rammler distribution function based on the methodology provided in the FLUENT documentation [2003FL1]. A further investigation is conducted to determine the effect of improving the curve-fit in certain intervals of drop diameters, by changing the spread parameter and mean diameter.

The analysis is conducted for two different drop size distributions, distribution *A* (experimentally determined in Chapter 4 for the test condition, $G_w = 2.21 kg/m^2s$ $G_a = 2.42 kg/m^2s$, with a large median diameter, and distribution *B*, Kröger [1998KR1], with a smaller median diameter. The experimental polydisperse drop distribution data is divided into *6* intervals for distribution *A* shown in Figure H.1, and *5* intervals for distribution *B*, for both distributions a section comprises a *2mm* span.

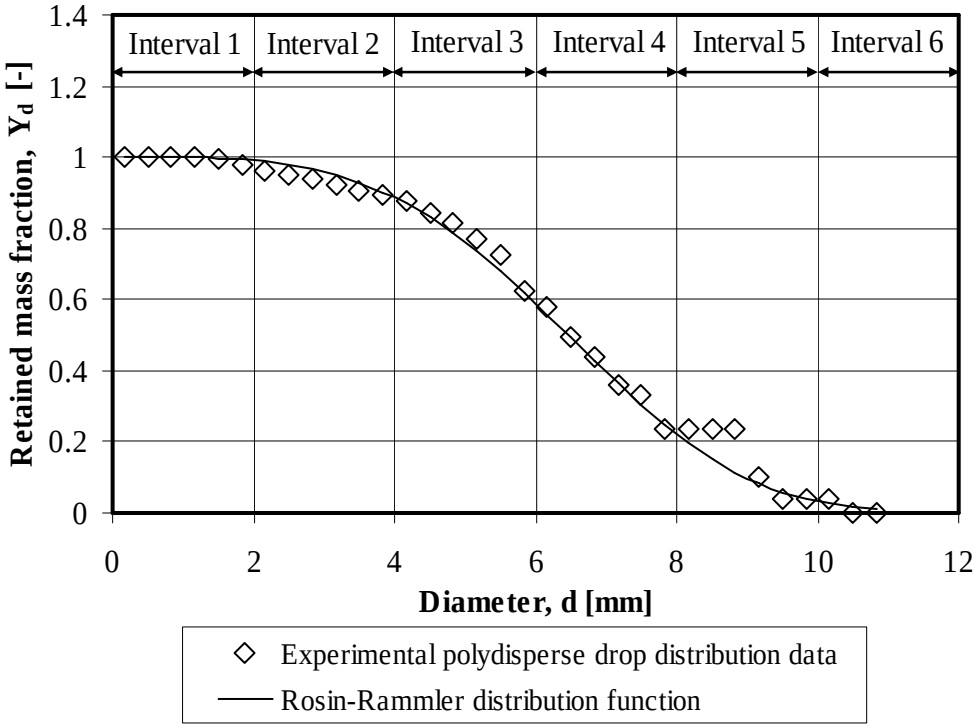

Figure H.1: Division of experimental polydisperse drop distribution data.

For each interval, using the experimental polydisperse drop distribution data, a least squares analysis is performed using the Rosin-Rammler distribution function by varying the values of the mean diameter, d_{RR}, and the spread parameter, n, with the aim of minimizing the sum of the squared deviation, irrespective of the sum of the squared deviations of the other sections. Each resultant Rosin-Rammler distribution function is recorded together with the sum of the squared deviations that it produces for all the intervals. The "best fit" Rosin-Rammler distribution function is determined by minimizing the sum of the squared deviations for all the sections. The results are given in Table H.1.

Table H.1 shows that for both distributions the "best fit" Rosin-Rammler distribution function gives better results than the standard Rosin-Rammler distribution function. The table also shows that the Rosin-Rammler distribution functions, fitted to the larger diameter based sections, on average correlate the water outlet temperature better. On average the smaller diameter based sections' Rosin-Rammler distribution functions seem to correlate the pressure drop over the domain better.

Table H.1: Analysis results for Distribution *A* and Distribution *B*.

Distribution *A*									
	Experimental polydisperse drop distribution data	Rosin-Rammler	Best fit	Interval 1	Interval 2	Interval 3	Interval 4	Interval 5	Interval 6
n	n/a	3.651	3.491	6.901	1.833	3.887	3.778	4.443	5.781
d_{RR}	n/a	7.142	7.310	3.141	12.616	7.203	7.184	7.721	8.111
T_{wo}	294.702	294.692	294.694	293.156	294.373	294.736	294.718	294.871	294.99
Δp	4.404	2.784	2.832	4.515	9.192	2.705	2.738	2.585	2.503
Distribution *B*									
	Experimental polydisperse drop distribution data	Rosin-Rammler	Best fit	Interval 1	Interval 2	Interval 3	Interval 4	Interval 5	Interval 6
n	n/a	2.308	2.021	1.884	1.009	2.556	1.562	2.758	n/a
d_{RR}	n/a	5.587	5.222	4.388	8.219	5.413	4.758	5.488	n/a
T_{wo}	293.445	293.8	293.456	292.937	292.614	293.877	292.815	293.997	n/a
Δp	4.55	3.961	4.571	5.465	6.14	3.779	5.788	3.568	n/a

Summary

It is shown that the standard Rosin-Rammler distribution function does not correlate the performance parameters the best.

The Rosin-Rammler distribution function does not correlate the performance parameters of the rain zone with sufficient accuracy for the purposes of this thesis and is therefore excluded as a means of inputting polydisperse drop distributions into FLUENT 6.2.16 for the modelling of wet-cooling tower rain zones.

APPENDIX

I

CFD Grid Independence Analysis

This appendix is used to present the results of the grid independence analysis. The purpose of the analysis is to determine the feasible cell size in the rain zone. The results that are monitored are the pressure drop across the domain, the outlet water temperature and the mass fraction of the water vapour at the air outlet boundary. The solver and model settings are discussed in Chapter 6.

The analysis is performed on a counterflow domain of $1 \times 1.5 \times 3m$ using hexahedral cells. The domain consists of *2400* face cells on the inlet and outlet boundaries, which are held constant throughout the analysis. The height of the cells is varied, as given below in Table I.1.

Table I.1: Cell height dimension and number of cells for a domain.

Cell height [mm]	Number of cells [-]
1500	4800
1000	7200
750	9600
600	12000
500	14400
375	19200
300	24000
250	28800
200	36000
150	48000
100	72000
75	96000
50	144000
42.9	168000
37.5	192000
33.3	216000
30	240000

The analysis is conducted using one set of simulation conditions, which are given below in Table I.2.

Table I.2: Simulation conditions for grid independence analysis of a counterflow domain.

Property	Value
Water mass flow, m [kg/s]	6
Monodisperse drop distribution diameter, d_d [mm]	2
Inlet air velocity, v_i [m/s]	2
Inlet water drops temperature, T_d [K]	313.9
Dynamic viscosity of air, μ_a [kg/ms]	1.72×10^{-5}
Diffusion coefficient, D [m^2/s]	1.963×10^{-5}
Thermal conductivity of air, k_a [W/mK]	0.026
Density of water drops, ρ_w [kg/m^3]	998.2
Specific heat of water drops, c_v [J/kgK]	4182
Latent heat of water drops, h_{fg} [J/kg]	2.4051×10^{6}
Ambient air pressure, p_a [N/m^2]	101325
Air drybulb temperature, T_a [K]	296.6
Relative humidity, Φ [-]	0.6

The saturated vapour pressure is a function of the water drop temperature, T_d, and is represented by a fourth order polynomial, given by,

$$p_{vs}(T_d) = 676.88\times10^{-6}T_d^4 - 735.7508\times10^{-3}T_d^3 + 301.9731T_d^2 - 55426.82T_d + 3836516 \quad \text{(I.1)}$$

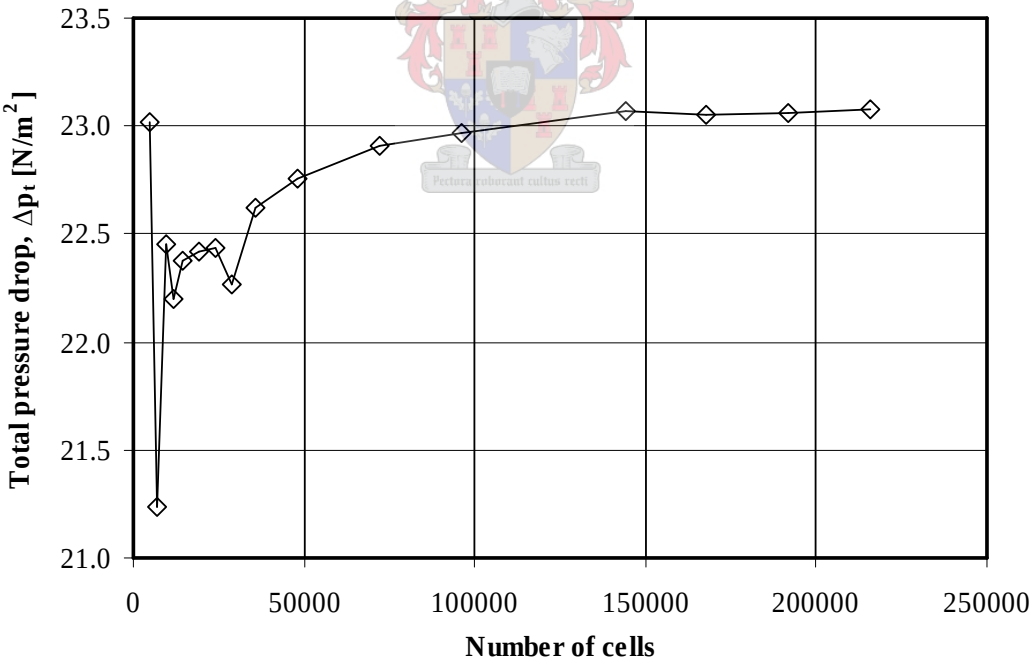

Figure I.1: Grid independence analysis of the total pressure drop across a counterflow domain.

Figure I.1 presents the results for the grid independence analysis of the total pressure drop across the domain. Figure I.2 presents the results for the grid independence analysis of the water outlet temperature and the mass fraction of water vapour at the air outlet boundary.

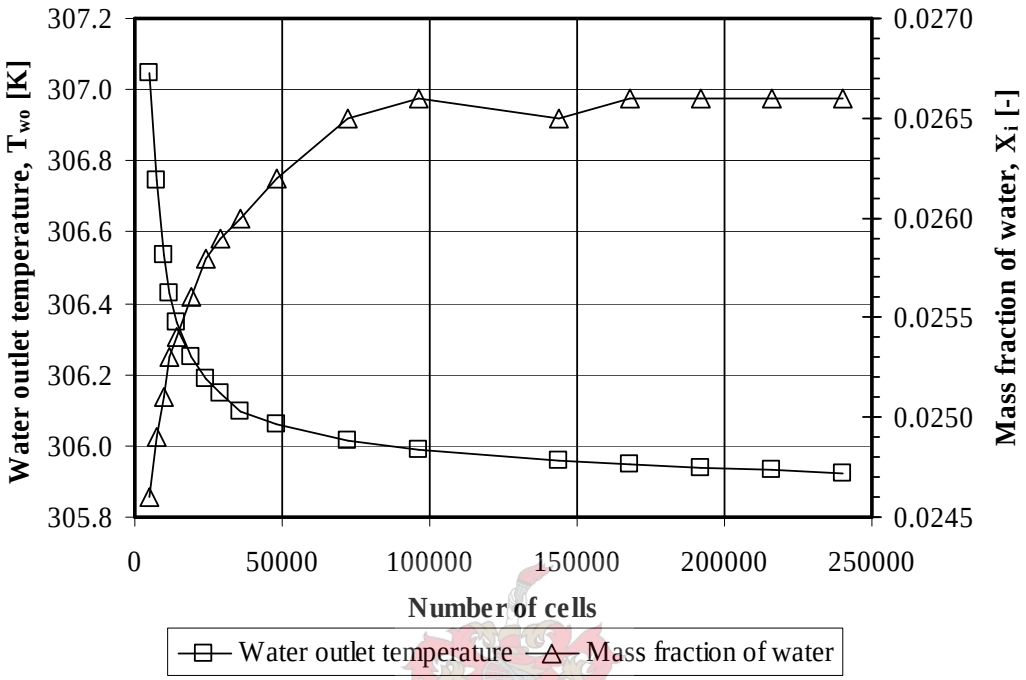

Figure I.2: Grid independence analysis of the water outlet temperature and the mass fraction of water vapour at the air outlet.

The convergence criteria for the monitored results are *0.02* for the total pressure drop and outlet water temperature and *0.0001* for the mass fraction of water. These three criteria are satisfied by a domain of *144 000* cells, referring to Table I.1 this translates to a cell height of *50mm*.

Two points were checked for the circular cooling tower domain and found to be in accordance with the results for grid independence of the counterflow domain.